UNIVERSIDADE D
COIMBRA

José António Assunção Marzia

INFLUENCE OF THE YIELD CRITERION IN THE FORMABILITY PREDICTION ON PARTS WITH COMPLEX GEOMETRY

Dissertação no âmbito do Mestrado Integrado em Engenharia Mecânica, área de Produção e Projeto orientada pela Professora Doutora Marta Cristina Cardoso de Oliveira e pelo Engenheiro Mário António Oliveira Santos e apresentada ao Departamento de Engenharia Mecânica, da Faculdade de Ciências e Tecnologia.

Outubro de 2020

1 2 9 0

FACULDADE DE CIÊNCIAS E TECNOLOGIA
UNIVERSIDADE D COIMBRA

Influence of the yield criterion in the formability prediction on parts with complex geometry

Submitted in Partial Fulfilment of the Requirements for the Degree of Master in Mechanical Engineering in the speciality of Production and Project

Influência do critério de plasticidade na previsão da conformabilidade em peças de geometria complexa

Author

José António Assunção Marzia

Advisors

Marta Cristina Cardoso de Oliveira

Mário António Oliveira Santos

Jury

President	**Professor Doutor Luís Filipe Martins Menezes** **Professor Catedrático da Universidade de Coimbra**
Vowel	**Professor Doutor Diogo Mariano Simões Neto** **Professor Auxiliar da Universidade de Coimbra**
Advisor	**Engenheiro Mário António Oliveira Santos** **Coordenador de Projeto e Construção de Ferramentas**

Institutional Collaboration

Volkswagen
Autoeuropa Lda.

Coimbra, October, 2020

Father, this is for you.

ACKNOWLEDGEMENTS

The present work would not be possible without the help and support of all the dear people in my life. I would like to dedicate this section to everyone who contributed for this work and helped me along the way.

Mom, thank you for being the bravest woman I know. For all the love, confidence and care in the world. Thank you, little sister, you are the joy of my life. Those moments of procrastination with you are always the most precious. I want you both to know how important you are to me and how indispensable your support was and always will be.

To my girlfriend, who has walked along side me through thick and thin, who has seen me at my worst and best and who is always pushing me to be a better version of myself every day. You never cease to amaze me with your incomparable kindness and passion. A very special thanks to you, with love.

To those I consider my family at heart. I'm forever thankful for all the inspiring words, for all the advice and affection. To my friends, from childhood through university. Thank you for all the laughter, for all the adventures and unforgettable moments. You are the fuel that drives me every day.

To professor Marta Oliveira. Thank you for sharing your unmeasurable knowledge and wisdom, for always answering my curiosity and being the best teacher and advisor, I could have had. This work is as much yours as it is mine.

My thanks go to Volkswagen Autoeuropa®, the institution that welcomed me for the internship. I appreciate the opportunity and all the resources provided without hesitation. A company is made by its people, and everyone that crossed my path has done so with a smile and eagerness to help. A special thanks goes to the CAD team of the UNCC, who taught and guided me through the whole process. Without belittling the companionship and aid of everyone, I would like to mention the colleagues that had a direct contribution to this work. To my advisor, Mário Santos, to Luís Monteiro, João Teixeira, João Sousa, Tânia Rodrigues, Luís Oliveira, Bernardo Oliveira and Rui Pires, my sincere gratitude.

I am truly a lucky man to have shared my time and learned from all of you.

Thank you.

Abstract

Sheet metal forming is an indispensable manufacturing technology in the automotive industry. The production of metallic components using this technology involves the planning of the process that requires complex and expensive tooling. The development of these tools has to consider the formability limits of the metal sheets. Finite element analysis codes, such as AutoForm®, are used throughout the industry to support the development of the tools, since they enable the prediction of defects, such as wrinkling and thinning. Unfortunately, in some cases defects arise in the metallic components, either in the tools try-out or in the production, which were not predicted by the finite element model. The main objective of this work is to understand the factors that can contribute to improving the prediction of forming defects for deep drawn automotive components.

Three case studies were considered in this work, a fender and two inner liftgates. Two galvanized steels of the same class, DX54D and DX56D, are used to produce the fender and the inner liftgates, respectively. For the fender and one of the inner liftgates, the study focused on the analysis of the influence of the equibiaxial stress value in the prediction of the formability, considering the Hill'48 and the BBC 2005 yield criteria. For the other inner liftgate, a thorough analysis of the kinematics of the forming process was performed to understand the factors that contribute for the occurrence of sporadic problems in production. In this context, the control options for the tools were explored as well as the material generator of AutoForm® R8, which required performing some experimental tests to characterize the mechanical behavior of the material. This enabled the use of the Vegter 2017 yield criterion, for this case study.

For all case studies, the formability analysis was performed with the linear and the non-linear forming limit curve. For this material class, it is known that the Hill'48 yield criteria overestimates the equibiaxial stress value. The results show that the equibiaxial stress value has impact on the formability predictions and it can even change the critical locations of defects. In this context, the use of the non-linear forming limit curve is very important, since strain paths close to plane strain followed by equibiaxial state or *vice versa* show higher exhaustion in formability. Based on the formability predictions, the equibiaxial stress value is estimated to be around 0.9 times the value predicted by the Hill'48 criterion, corroborating

previous studies. In this context, the Vegter 2017 yield criterion can be considered an interesting approach to describe the plastic behavior of the material, since its parameters identification only requires performing three uniaxial tensile tests. Finally, besides an accurate description of the plastic behavior of the material, the prediction of defects requires the proper definition of the kinematics of the process.

Keywords Sheet metal forming, Finite element method, Yield criterion, Formability, Non-linear strain paths, AutoForm® R8.

Resumo

A conformação de chapas metálicas é uma tecnologia de produção indispensável na indústria automóvel. A produção de componentes metálicos com esta tecnologia envolve o planeamento do processo, que requer ferramentas complexas e dispendiosas. A conceção dessas ferramentas deve considerar os limites de conformabilidade das chapas metálicas. Os códigos de análise por elementos finitos, como o AutoForm®, são utilizados na indústria para apoiar a conceção das ferramentas, já que permitem prever defeitos, como rugas e a localização da deformação. Infelizmente, em alguns casos surgem defeitos nos componentes metálicos, seja no *try-out* das ferramentas ou na produção, que não são previstos pelos modelos de elementos finitos. O objetivo principal deste trabalho é compreender os fatores que podem contribuir para melhorar a previsão de defeitos de conformação em componentes automóveis estampados.

Neste trabalho foram considerados três casos de estudo, um guarda-lamas e dois portões traseiros interiores. São utilizados dois aços galvanizados da mesma classe, DX54D e DX56D, para produzir o guarda-lamas e os portões interiores, respetivamente. Para o guarda-lamas e um dos portões interiores, o estudo focou-se na análise da influência do valor da tensão equibiaxial na previsão da conformabilidade, com base nos critérios de plasticidade de Hill'48 e BBC 2005. Para o outro portão interior, foi realizada uma análise minuciosa da cinemática do processo de conformação, para analisar os fatores que contribuem para a ocorrência de problemas esporádicos na produção. Neste contexto, foram exploradas as opções de controle das ferramentas, assim como o gerador de materiais do AutoForm® R8, o que exigiu a realização de alguns ensaios experimentais para caracterizar o comportamento mecânico do material. Assim, foi possível utilizar o critério de plasticidade de Vegter 2017, para este caso de estudo.

Para todos os casos de estudo, a análise de conformabilidade foi realizada com a curva limite de estampagem linear e não-linear. Com base em resultados anteriores, sabe-se que o critério de plasticidade de Hill'48 sobrestima o valor da tensão equibiaxial, para esta classe de material. Os resultados mostram que o valor da tensão equibiaxial tem impacto nas previsões de conformabilidade e pode até mesmo alterar as regiões críticas para a ocorrência de defeitos. Nesse contexto, o uso da curva limite de estampagem não-linear é muito

importante, uma vez que trajetórias de deformação próximas da deformação plana seguidas de estado equibiaxial, ou *vice-versa*, apresentam maior exaustão de conformabilidade. Com base nas previsões de conformabilidade, é possível estimar um valor para a tensão equibiaxial de 0.9 vezes o valor previsto pelo critério de Hill'48, o que corrobora estudos anteriores. Nesse contexto, o critério de plasticidade de Vegter 2017 pode ser considerado uma abordagem interessante para descrever o comportamento plástico do material, uma vez que a identificação dos seus parâmetros requer apenas a realização de três ensaios de tração uniaxial. Finalmente, além de uma descrição precisa do comportamento plástico do material, a previsão de defeitos requer a definição adequada da cinemática do processo.

Palavras-chave: Conformação de chapas metálicas, Método dos elementos finitos, Critério de plasticidade, Formabilidade, Trajetórias de deformação não-lineares, AutoForm® R8.

Contents

LIST OF FIGURES

LIST OF TABLES

LIST OF SIMBOLS AND ACRONYMS

List of Symbols

$\mathbf{0}$ – Null tensor

α – Limit angle for mesh control options

β – Strain path strain ratio

γ – Angle formed between the rolling direction and the first principal stress

$\boldsymbol{\Upsilon}$ – Transverse shear strain vector

$\overline{\boldsymbol{\Upsilon}}$ – Assumed transverse shear strain vector

Δ – Increment

$\boldsymbol{\varepsilon}$ – Infinitesimal deformation tensor

$\varepsilon_{\mathrm{eq}}$ – Equivalent strain

ε^{p} – Equivalent plastic strain

$\dot{\varepsilon}$ – Thinning rate

θ – Angle formed in the sheet plane with respect to the rolling direction

ϑ – Rotation degree of freedom

ϑ_n – Linear variation of the rotation

ϑ_s – Quadratic variation of the rotation

κ – Shear correction factor

λ – Strain path length ratio

μ – Bézier interpolation factor

ρ – Strain ratio

Π – Variational functional of the modified Hu-Washizu principal

Π_{b} – Bending component of the variational functional of the modified Hu-Washizu principal

Π_{s} – Shear component of the variational functional of the modified Hu-Washizu principal

Π_{ext} – External forces component of the variational functional of the modified Hu-Washizu principal

$\boldsymbol{\sigma}$ – Stress tensor

$\bar{\sigma}$ – Equivalent stress

$\vec{\sigma}$ – Stress vector

σ_0 – Yield stress in the rolling direction

σ_{45} – Yield stress for an angle of 45º with respect to the rolling direction

σ_{90} – Yield stress for an angle of 90º with respect to the rolling direction

σ_{b} – Equibiaxial yield stress

σ_{ps} – Plane strain yield stress

σ_{shear} – Shear yield stress

τ – Shear stress

τ_{R} – Friction shear stress

υ – Poisson ratio

Φ – Yield function

ϕ_k – Shear influence factor

$\boldsymbol{\chi}$ – Curvature vector

A – Area

A_{g} – Percentage of total elongation at maximum force

A_{t} – Percentage of total elongation at fracture

$\boldsymbol{B}$ – Matrix of the partial derivatives of the shape functions

$\boldsymbol{B_{\mathbf{b}}}$ – Bending matrix of the partial derivatives of the shape functions

$\boldsymbol{B_{\mathbf{s}}}$ – Shear matrix of the partial derivatives of the shape functions

Biax – Biaxial factor

cof – Coefficient of friction

cof_{eff} – Effective coefficient of friction

d – Displacement

D – Deformation rate tensor

E – Young modulus

f_z – Static distributed load in the z direction

f_{Dirac} – Dirac function

F – Deformation gradient

F – Normalized stress

$\vec{F}$ – Normalized stress vector

F_{N} – Normal force

F_{R} – Shear force due to friction

F_{c} – Cylinder force

h – Element thickness

$\boldsymbol{H_{\mathbf{b}}}$ – Bending constitutive matrix

$\boldsymbol{H_{\mathbf{s}}}$ – Shear constitutive matrix

I – Identity matrix

K – Stiffness matrix

$\boldsymbol{K_{\mathbf{b}}}$ – Bending component of the stiffness matrix

$\boldsymbol{K_{s}}$ – Shear component of the stiffness matrix

$\boldsymbol{K_{\mathbf{P}}}$ – Plate stiffness matrix

l – Strain path length

L – Velocity gradient tensor

L_k – Length of the segment of index k

$\boldsymbol{M}$ – Bending moment per unit length tensor

M – Yield criterion exponent

$\boldsymbol{N}$ – Shape functions

p – Pressure

p – Permissible penetration

p_{ref} – Reference pressure

p_{charge} – Cylinder charge pressure

p_{cyl} – Cylinder pressure

P – External forces

P_k – Higher order shape functions

r – Radius

r_θ – Anisotropy coefficient with respect to the angle θ

r_b – Equibiaxial anisotropy coefficient

r_m – Average anisotropy coefficient

R – Internal forces

R_m – Tensile strength

$R_{\mathrm{p0.2}}$ – Proof strength at 0.2% of the extensometer gauge length

t – Time

$\boldsymbol{T}$ – Shear force per unit length tensor

$\boldsymbol{u}$ – Vector of nodal degrees of freedom

$\widehat{\boldsymbol{u}}$ – Vector of nodal displacements

$\boldsymbol{U_n}$ – Plate element´s vector of nodal degrees of freedom

w – Weight factor

W – Plastic work

$\mathbf{X}$ – Reference position vector

Y – Yield stress

Y_θ – Yield stress with respect to the angle θ

Y_{b} – Equibiaxial yield stress

Acronyms

2D – Two dimensional

3D – Three dimensional

CAD – Computer Aided Design

CAE – Computer Aided Engineering

EPS – Elastic-Plastic Shell

FE – Finite Element

FEA – Finite Element Analysis

FEM – Finite Element Method

FLC – Forming limit curve

FLD – Forming limit diagram

GFLC – Generalized forming limit concept

ND – Normal direction

RD – Rolling direction

TD – Transverse direction

TDEM – Time Dependent Evaluation Method

UNCC – Unidade de Negócios de Cunhos e Cortantes

1. INTRODUCTION

The present work was performed in an industrial context in collaboration with Volkswagen Autoeuropa®, more specifically, in the Computer Aided Design (CAD) department of the Tools and Die Business Unit (UNCC). The purpose of this unit is the development and production of sheet metal forming tools for the automotive industry. In this context, one of the commercial codes used to perform the tools' virtual try-out is AutoForm®. In the following section a brief description of sheet metal forming process is given, including the tools and machinery needed. Afterwards, the motivation and objectives of the work are laid out.

1.1. Sheet Metal forming

Sheet metal forming is a process in which a blank (flat, thin metallic sheet) is peripherally restrained while being forced to deform by a punch into a die, resulting in a geometry that cannot be defined using flat patterns. The ratio between the area and the depth of the part is normally used to distinguish stamping from deep drawing processes, with the latest being used for deeper components. However, it can also be used to distinguish between the processes driven by radial tension-tangential compression (deep drawing) and by stretch-and-bending (stamping). In either case, the tools used in sheet metal forming processes have different purposes. The geometry of the die is commonly imposed by the one of the aimed component and by the addendum required to support the initial blank. This means that the geometry of the punch can be generated by applying an offset to the die cavity geometry, which establishes the gap between the punch and the die. The blankholder or binder is typically obtained by applying an offset to the addendum region of the die, meaning that it is an outer tool that applies the restraining force to the blank. Deep drawing processes aimed at producing automotive parts, generally require the reduction of the material flow to the die cavity, to increase the stretching of the metallic material and, consequently, promote increased rigidity and reduce the springback effect. Sometimes, in order to reduce the material flow it is necessary to introduce drawbeads in the blankholder, which are, in

essence, grooves or steps. They can be positioned all around the part and/or in specific sections, depending on the required control.

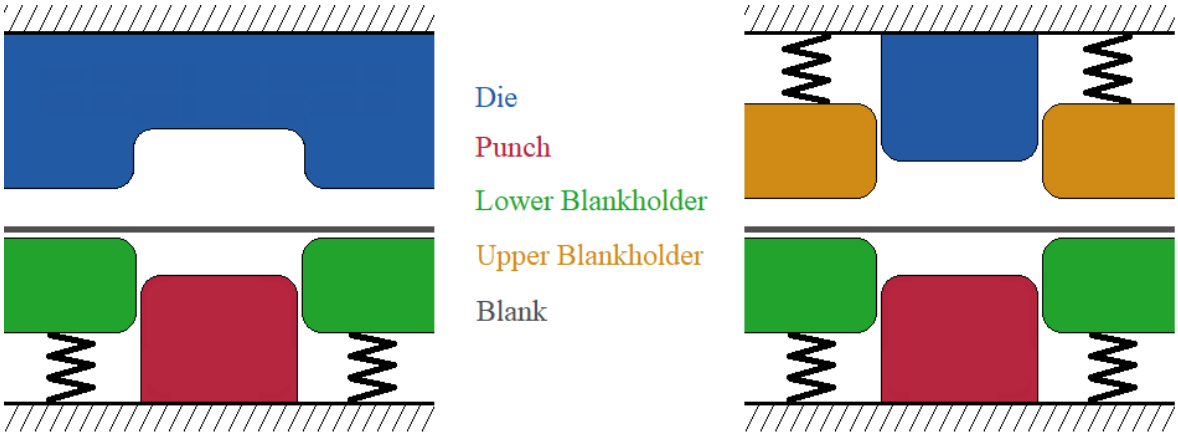

Figure 1.1 Schematic representations of a single-action press (left) and triple-action press (right).

The tools are mounted on presses, the main equipment needed to perform deep drawing processes. They provide the necessary linear force to the tools that interact with the metal sheets. There are different kinds of presses, including mechanical and hydraulic. Generally, mechanical presses are preferred in a mass production environment, since they enable faster operations. Presses can also be classified according to their operation type. The ones of interest for the current work are the single-action and triple-action presses. Action refers to the number of slides or rams that operate on the same axis and that are mounted within the same frame. A single-action press has one slide, corresponding to the die that displaces against a fixed bed, comprised by the punch and blankholder. However, in recent presses the blankholder is usually supported by a cushion system, which provides a constant force and a stroke relative to the punch, referred as cushion stroke. This enables the blankholder to apply pressure to the metal sheet before the drawing occurs. Although this requires the existence of another slide in the bed of the press, the nomenclature is not altered, i.e. they are referred as single-action presses, as schematically shown in Figure 1.1 (left). Double-action presses possess two slides and, in essence, work like an inverted single-action press, with a fixed die on the press bed and the punch and an upper blankholder on the displacing ram. On the other hand, triple-action presses, have three slides: two that work in a similar fashion to the single-action press; and a third that resides in the ram and applies

force in the opposite direction, typically using an outer blankholder, like double-action presses. This means that there are two different cushion strokes, one relative to the punch and another to the die, as schematically shown in Figure 1.1 (right). The main advantage of the triple-action press is that it can draw parts with a more complex geometry, since it enables drawing in both directions. Nevertheless, they operate slower than single-action presses, since the third action takes additional time (Wick, Benedict and Veilleux, 1984; Smith, 1990).

1.2. Motivation

Sheet metal forming is a reference manufacturing process in the automotive industry, for the production of various components, such as inner or outer body panels and structural elements. Several different processes are commonly required to obtain the final desired part from the initial sheet (coil). These include blanking, stamping or deep drawing, trimming, hemming and flanging. Each of them requires specific tools, tailored for the process. Nowadays, the design of such tools resorts to the virtual try-out, using the Finite Element Method (FEM). Computer Aided Engineering (CAE) relies heavily on Finite Element Analysis (FEA) since it significantly reduces product development costs and time. This has become rather important with the ever more complex geometries of automotive parts, the implementation of lightweight materials and the desire to continuously improve the quality, safety and reliability of the vehicles. Stamping and deep drawing are the first engineering challenge of sheet metal forming processes. The sheet must be plastically deformed to the desired geometry without showing any defect, the most notorious of which are wrinkles and splits. Engineers seek to improve FEM numerical solutions, in order to reproduce as much as possible, the experimental try-out condition and, consequentially, the production.

1.3. Objectives

The main objective of this work is to understand why certain defects appear in deep drawn parts, even though they are not detected in the Finite Element (FE) simulations performed with AutoForm®. In this context, representative cases studies were selected, which dictated the adoption of two different approaches. The first focused on the influence

of the model used to describe the material mechanical properties on formability predictions, where special emphasis was given to the yield criterion. The possibility of creating a material file, with the aid of AutoForm®'s material generator was also studied. The second approach involved a thorough understanding of the control options provided for the tools, by the commercial FE code used in this work, AutoForm®, in order to best reproduce the process conditions.

1.4. Layout of the thesis

This section presents a summary of the contents covered in this work. The thesis comprises of two main parts, organized into six chapters. The first part is dedicated to the state-of-the-art of sheet metal forming, highlighting the aspects related to the AutoForm® FE commercial solver, and is constituted by chapter 2 through 4. The second part corresponds to the analysis of three case studies (chapter 5) and the main conclusions of the work (chapter 6).

Chapter 2 presents the main characteristics of AutoForm® 's forming solver, including some details regarding the shell element's bending formulation and the strategies used for the automatic mesh refinement. The different options available for the control of the tools are also explored. The knowledge pertaining to the material generator is exposed, namely the main assumptions concerning the yield criterion, the different hardening laws available and the principles behind the linear forming limit curve.

Chapter 3 is dedicated to the anisotropic yield criteria implemented in AutoForm® and used within the context of this work. The general assumptions are laid out, leading to the chronologically description of the yield criteria, starting with Hill'48 and ending with Vegter 2017. Emphasis is given to the mathematical formulation of each yield criterion.

Chapter 4 introduces the generalized forming limit concept, a phenomenological approach that is heavily based on knowledge acquired from experimental tests, which extends the use of the linear forming limit curve to the analysis of non-linear strain paths. The strategy adopted in AutoForm® to explore the concept is also explained.

Chapter 5 presents the three case studies, which were selected with two different goals. The first two components, a fender and an inner liftgate, are used to study the

formability sensitivity to the mechanical properties of the material, specifically to the equibiaxial stress value. The third case study, also an inner liftgate, is a component in production that occasionally shows defects, such as wrinkles, that do not appear in the FE simulation. The reason behind this is discussed and a solution to minimize the problem is proposed.

Chapter 6 is devoted to the conclusion taken from this work, summarizing the main difficulties and presenting some recommendations for future work.

2. AUTOFORM® FORMING SOLVER

The Volkswagen® group utilizes the commercial software AutoForm® for the tools method planning. This software uses the Finite Element Method to simulate processes such as stamping, deep drawing, hemming, trimming and flanging. These processes involve non-linear analysis, where material, geometrical and boundary conditions non-linearities occur. This processes also involve finite or large deformations of the thin sheets. Therefore, the software uses triangular, bidimensional elements with a Lagrangian formulation, meaning that only the middle plane of the sheet is subjected to loadings, assuming a plane stress condition. Plane stress is a simplification that considers that the components of stress and shear perpendicular to the mid plane are null. The information pertaining to this chapter was taken from the AutoForm® R8 user's manual (*AutoForm® R8 software manual*, 2018), provided by Volkswagen Autoeuropa® during the time period of the curricular internship.

2.1. Implicit Solution

The software´s integration scheme is based on an implicit time integration method. In other words, it considers the analyzed problems as quasi-static, disregarding any dynamic forces. In each iteration, the following equilibrium equation is solved for the time $t + \Delta t$:

$$^{t+\Delta t}\mathbf{R} - {}^{t+\Delta t}\mathbf{P} = \mathbf{0}, \tag{2.1}$$

where **R** and **P** represent the internal and external forces, respectively. For implicit methods the time steps are in essence increments of displacement, since time does not play a direct role in the formulation. The equilibrium equation is solved with a Taylor series, with:

$$\mathbf{K}(\hat{\boldsymbol{u}})\Delta\hat{\boldsymbol{u}} - \mathbf{P}(\hat{\boldsymbol{u}}) = \mathbf{0}, \tag{2.2}$$

where **K** is the stiffness matrix, $\hat{\boldsymbol{u}}$ the vector of nodal displacements and $\Delta\hat{\boldsymbol{u}}$ the unknown displacement increment.

The main advantage of this formulation when compared to the other most commonly adopted, the dynamic explicit method, is that it is unconditionally stable. Thus, the chosen time steps can be significantly larger without the occurrence of instabilities. The

explicit method is conditionally stable, meaning that for time steps larger than the critical one it is not possible to assure the accuracy of the solution. This translates into the need to use very small time steps. However, the higher stability of the implicit method comes with a disadvantage. A set of non-linear algebraic equations must be linearized and solved for each increment, using an iterative process, which requires additional CPU time and memory. In addition, very large increments can cause convergence problems due to, for example, strong changes in contact constraints. Nevertheless, this solution imposes no restriction on the spatial discretization, which is an important aspect for its preferred choice in many applications. This will be further addressed in the following subchapters (Zienkiewicz, Taylor and Zhu, 2013; Belytschko *et al.*, 2014).

2.2. Finite Elements

Triangular elements are widely used due to their simple formulation. They are ideal for generating non-structured meshes and are very flexible, enabling local refinement. In other words, a clear distinction can be made between coarse and finer regions on the mesh. Zones with high gradients of deformation and/or stress, like regions with small curvature for example, should necessarily be discretized with elements with a smaller size. The coupled use of finer with coarser mesh regions, optimizes computational time and memory spent without significant loss in accuracy (Teixeira-Dias *et al.*, 2018).

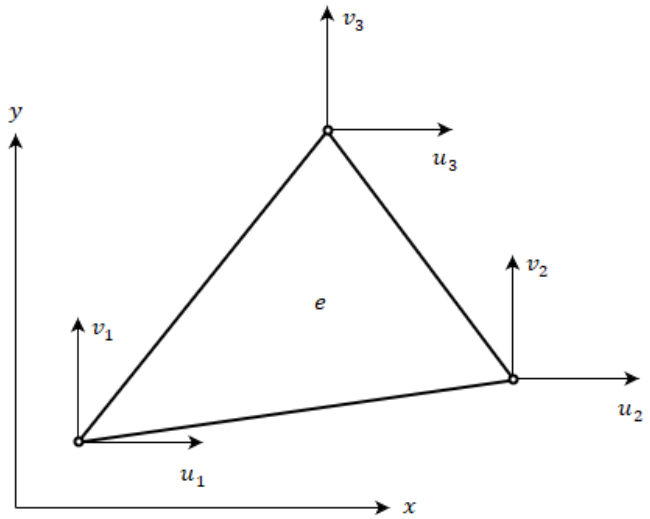

Figure 2.1. Generic triangular element.

Consider the generic triangle element shown in Figure 2.1, with nodal degrees of freedom, u_i^{e}, v_i^{e}, with $i = 1, 2, 3$. The displacement field can be defined by the shape functions, N_i^{e}, and the nodal degrees of freedom as follows:

$$\boldsymbol{u} = \begin{Bmatrix} u(x,y) \\ v(x,y) \end{Bmatrix} = \begin{bmatrix} N_1^{\mathrm{e}} & 0 & N_2^{\mathrm{e}} & 0 & N_3^{\mathrm{e}} & 0 \\ 0 & N_1^{\mathrm{e}} & 0 & N_2^{\mathrm{e}} & 0 & N_3^{\mathrm{e}} \end{bmatrix} \begin{Bmatrix} u_1^{\mathrm{e}} \\ v_1^{\mathrm{e}} \\ u_2^{\mathrm{e}} \\ v_2^{\mathrm{e}} \\ u_3^{\mathrm{e}} \\ v_3^{\mathrm{e}} \end{Bmatrix}, \tag{2.3}$$

where, considering linear interpolation, the shape functions are:

$$N_i^{\mathrm{e}} = \frac{1}{2A^{\mathrm{e}}}(\alpha_i + \beta_i x + \gamma_i y), \tag{2.4}$$

with $\alpha_i = \left(x_j y_k - x_k y_j\right)$, $\beta_i = \left(y_j - y_k\right)$ and $\gamma_i = \left(x_k - x_j\right)$, where x_i and y_i are the spatial coordinates of the nodes ($i = 1, 2, 3$). The area of the finite element can be obtained based on the following determinant:

$$A^{\mathrm{e}} = \frac{1}{2}\det\begin{bmatrix} 1 & x_1 & y_1 \\ 1 & x_2 & y_2 \\ 1 & x_3 & y_3 \end{bmatrix} = \frac{(x_2 - x_1)(y_3 - y_1) + (x_1 - x_3)(y_2 - y_1)}{2}. \tag{2.5}$$

From continuum mechanics, the infinitesimal deformation tensor is given by:

$$\boldsymbol{\varepsilon} = \begin{Bmatrix} \varepsilon_{xx} \\ \varepsilon_{yy} \\ \varepsilon_{xy} \end{Bmatrix} = \begin{Bmatrix} \dfrac{\partial u}{\partial x} \\ \dfrac{\partial v}{\partial y} \\ \dfrac{\partial u}{\partial y} + \dfrac{\partial v}{\partial x} \end{Bmatrix}, \tag{2.6}$$

so, the strain field can be obtained by:

$$\boldsymbol{\varepsilon} = \begin{bmatrix} \dfrac{\partial N_1^{\mathrm{e}}}{\partial x} & 0 & \dfrac{\partial N_2^{\mathrm{e}}}{\partial x} & 0 & \dfrac{\partial N_3^{\mathrm{e}}}{\partial x} & 0 \\ 0 & \dfrac{\partial N_1^{\mathrm{e}}}{\partial y} & 0 & \dfrac{\partial N_2^{\mathrm{e}}}{\partial y} & 0 & \dfrac{\partial N_3^{\mathrm{e}}}{\partial y} \\ \dfrac{\partial N_1^{\mathrm{e}}}{\partial y} & \dfrac{\partial N_1^{\mathrm{e}}}{\partial x} & \dfrac{\partial N_2^{\mathrm{e}}}{\partial y} & \dfrac{\partial N_2^{\mathrm{e}}}{\partial x} & \dfrac{\partial N_3^{\mathrm{e}}}{\partial y} & \dfrac{\partial N_3^{\mathrm{e}}}{\partial x} \end{bmatrix} \begin{Bmatrix} u_1^{\mathrm{e}} \\ v_1^{\mathrm{e}} \\ u_2^{\mathrm{e}} \\ v_2^{\mathrm{e}} \\ u_3^{\mathrm{e}} \\ v_3^{\mathrm{e}} \end{Bmatrix}. \tag{2.7}$$

Defining the matrixes of the partial derivatives of the shape functions as:

$$\boldsymbol{B}_i = \begin{bmatrix} \frac{\partial N_i^{\mathrm{e}}}{\partial x} & 0 \\ 0 & \frac{\partial N_i^{\mathrm{e}}}{\partial y} \\ \frac{\partial N_i^{\mathrm{e}}}{\partial y} & \frac{\partial N_i^{\mathrm{e}}}{\partial x} \end{bmatrix} = \frac{1}{2A^{\mathrm{e}}} \begin{bmatrix} \beta_i & 0 \\ 0 & \gamma_i \\ \gamma_i & \beta_i \end{bmatrix}. \tag{2.8}$$

The compact form of the deformation matrix is $\boldsymbol{\varepsilon} = \boldsymbol{B}\boldsymbol{u}^{\mathrm{e}}$, with:

$$\boldsymbol{B} = \frac{1}{2A^{\mathrm{e}}} \begin{bmatrix} \beta_1 & 0 & \beta_2 & 0 & \beta_3 & 0 \\ 0 & \gamma_1 & 0 & \gamma_2 & 0 & \gamma_3 \\ \gamma_1 & \beta_1 & \gamma_2 & \beta_2 & \gamma_3 & \beta_3 \end{bmatrix}. \tag{2.9}$$

AutoForm® R8 version comes with different FE formulations for membrane and shell elements. For the first type, only one is available: Bending Enhanced Membrane. For the second, three formulations are considered: Elasto-Plastic Shell, Composite Shell (specific to deal with composite materials) and Thick Shell (recommended for coining and ironing processes). Since the studied blanks are of small thickness and only metallic materials are analyzed, the option is between membrane and shell formulations. The membrane element has three translational degrees of freedom per node, whereas the shell element has five: three translations and two rotations. Membrane elements can be used to analyze forming processes and lead to faster simulation times. However, complex parts show regions that go through bending and unbending processes as they deform. This coupled with the existence of geometric details with considerably small radii compromises accuracy, when using membrane elements. Therefore, the shell element is the preferred choice between the two, since the rotational degrees of freedom grant it the ability to include the bending effects. More details are given in the next subchapter.

2.2.1. Elasto-Plastic Shell Element

A shell element is the combination of a membrane and a plate element. Many different shell formulations have been proposed, each one presenting specific pros and cons. They can be considered the most complete 2D formulations, having up to six degrees of freedom per node. The shell element implemented in AutoForm® seems to be a combination of a membrane element that has a specific formulation (confidential details)(Kubli, 1995) with a plate element, proposed by Katili (1993). The text presented in ANNEX A focuses

on the plate formulation adopted in the Elasto-Plastic Shell (EPS) element implemented in AutoForm®.

2.2.1.1. Integration points

The evaluation of the stiffness matrix is performed using a trapezoidal Lobatto integration scheme, which can be applied considering a different number of integration points through the blank thickness, to evaluate the stress and strain. The software always considers a single point in the mid plane. Regarding the through-thickness direction, AutoForm® R8 has two predefined choices, those being either 5 or 11 integration points. Banabic (2010) showed in a springback prediction study of a U-rail (benchmark from Numisheet'93) that when using 5 or more integration points the results were already stable. Interestingly, after 9 points there were no significant improvements and with 13 points the computational time started to increase significantly. Therefore, in order to guarantee a reasonable compromise between accuracy and computational cost, AutoForm® recommends the use of 11 points, since it allows capturing the stress gradients resulting from bending effects which, ultimately, are the main cause for springback. This also increases the accuracy of the results of stress and strain in the upper and bottom layers of the sheet.

2.2.2. Adaptive mesh

There are various mesh adaptation strategies but, globally falling in two main categories: h- and p-refinement. In a general sense, h-refinement changes the size of the elements as needed, decreasing it for higher accuracy or increasing otherwise. On the other hand, p-refinement maintains the size but raises the order of the interpolation polynomial for specific elements. For h-refinement there are three typical methods that can be applied, namely element subdivision, mesh regeneration or node reallocation (also known as r-refinement). The first uses the existing elements and boundaries and simply enriches the mesh by division. The second generates an entirely new, finer mesh for the following iteration. Both of these methods enable refinement and de-refinement unlike the r-refinement method, which doesn't alter the number of elements and instead changes the nodes position (Zienkiewicz, Taylor and Zhu, 2013).

AutoForm® uses the element subdivision h-method, dividing or joining triangular elements, using an algorithm developed to take into account a set of criteria to

support the decision. This algorithm associates a refinement level of 0 to the initial element size and increases it as the element is divided. A representation of this procedure is shown in Figure 2.2. Going from a specific level to the next divides the element in four. This can happen successively until the maximum refinement level defined by the user is reached, raising the local density of the mesh. When the refinement level is no longer needed, the opposite happens by combining four elements into one. This can be repeated until the level 0 is recovered. The strategy employed by the software guarantees that the refinement starts before any contact is made with any geometrical features.

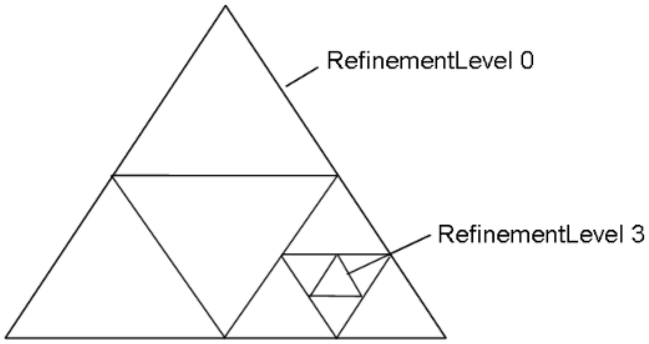

Figure 2.2. Schematic representation of the refinement level used in AutoForm® (*AutoForm® R8 software manual*, 2018).

2.2.2.1. Refinement criteria

The software gives the user the freedom to control four main refinement parameters, the *initial max element size*, the aforementioned *max refinement level*, the *radius penetration* and the *max element angle*. The *initial max element size* selected defines the size associated with the refinement level 0. In practice, the selection of a smaller element size makes the whole mesh finer from the start of the simulation. The *radius penetration* defines the permissible penetration, p, between the sheet and the tools in curvature zones. The *max element angle* is the limit angle, α, that the element can present in relation to a 90º radius. It restricts the minimum number of elements that are permissible to form that radius. These parameters are represented in Figure 2.3. Note that they are not independent, with the stricter dominating over the other.

Another parameter that is worth mentioning is the *tangential refinement*. Unlike the others it is an on or off option that extends the refinement range by a factor of 2.5 times the thickness of the blank. It helps to better capture the stress gradient that exists close to zones with strong curvature.

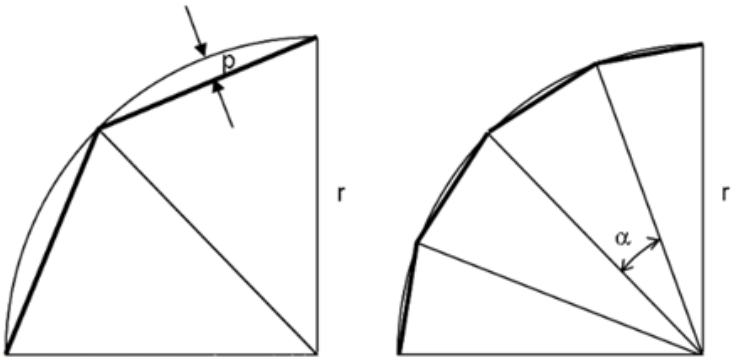

Figure 2.3. Schematic representation of the radius of penetration (left) and the maximum element angle (right) used in AutoForm® (*AutoForm® R8 software manual*, 2018).

2.2.3. Adaptive Time Step

The time step defines the displacement made in each increment. It is controlled by the *max material displacement* parameter, which is the maximum possible tangential displacement of the nodes relatively to the contacting tool. There are other parameters to limit the time step or define an interval of possible values (*min* and *max tool displacement*). When close to bottoming, the software can be set to have smaller displacements. This helps capture the final moments of drawing, where the last geometrical details are made. The user can define both the *end tool displacement step* and the total number of steps.

2.3. Tools and Support Types

AutoForm® R8 gives the user different control options, or support types, for the process tools. They can be rigid, force controlled, spring controlled or gap controlled. Rigid tools are considered attached to the ram or bed of the press, having a very high rigidity and a negligible theoretical deformation. This option is typically used to simulate the punch or the die. Force controlled tools are specific for blankholders or pads. The specified force is applied and lift up of the tool is not allowed. If the initial force is not enough to counter the sheet's reaction force, then the force applied to the tool is automatically raised to avoid the lift up. Throughout the simulation the force can also rise if necessary. This kind of control is very useful. It can be used to determine the minimum blankholder force needed to keep the tools closed during the forming process. Spring controlled tools have similar applications to force controlled tools. However, lift up is possible for spring controlled tools. In other words,

they are controlled by displacement and maintain the user-prescribed force. These two types of support can have elastic deformation, providing a more realistic pressure distribution in the contact area. This is defined with the tool's stiffness. Gap controlled tools, like the name implies, maintain a desired gap between the selected tools. This happens, for example, when spacing blocks are used in the process. It should be noted that no binder pressure is applied when this support is used. When using EPS, the gap controlled tool is considered rigid.

The definition of force, spring and gap controlled tools involves the selection of an opposing tool and of the cushion stroke. This corresponds to the distance the specific tool is from its fully closed position at the end of the process. This distance does not include the blankholder closing stage.

2.3.1. Drawbeads

The drawbeads should be the first feature to deform the blank, right as the blankholder closes. Two different models exist to simulate their effect, the physical model and the equivalent drawbead model. The physical model uses the drawbead geometry directly in the simulation by creating or importing it in the surface of the blankholder. This way, the software considers the bending and unbending of the sheet caused by the drawbead. On the other hand, the equivalent drawbead model calculates the additional restraining forces caused by the intended drawbead's geometry and applies them to the blank. The simulation runs without the geometrical complexity of the drawbead, saving computational time and memory. For a better understanding, Figure 2.4 shows an example comparing the two models.

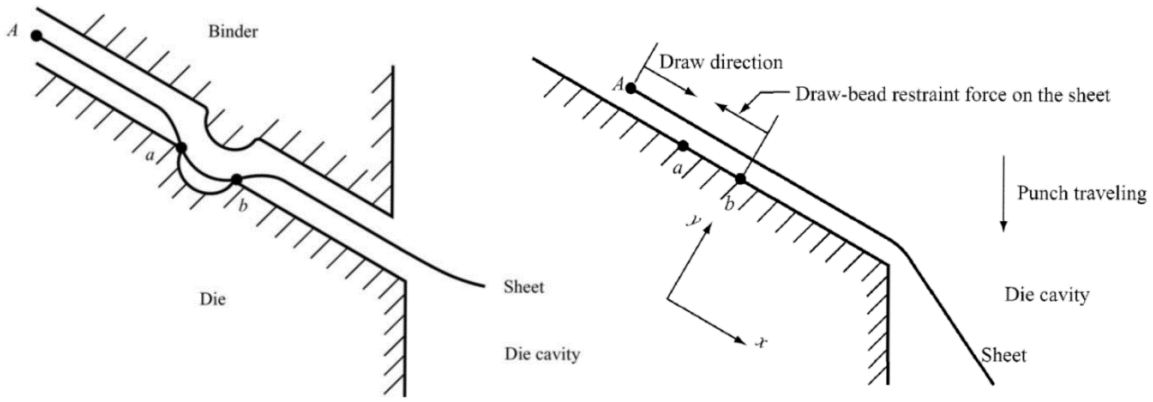

Figure 2.4. Representation of a drawbead equivalent model (Tang and Pan, 2007).

The equivalent drawbead model is recommended when the material that flows through this geometrical detail does not remain on the final part, since it will not affect springback or change significantly the forming results. Otherwise the physical model shows superior accuracy and should be the preferred choice (Tang and Pan, 2007; Banabic, 2010). AutoForm® R8 has both approaches and can even use a combination of them, using the physical model during the blankholder closing and the equivalent drawbead model after.

2.3.2. Binder Model

The binder model describes how the forces are transferred to the blank. In other words, it represents the behavior of the components that apply force to the tools, such as gas cylinders, cushion pins, hydraulic columns, etc. Three methods are available in the software: uniform loading, columns, and cushion pins, each with its own peculiarities. Uniform loading guarantees that a uniform binder pressure is applied. According to the AutoForm® R8 user manual, this simplifies the analysis greatly since the point of application of the binder force can be unknown. Columns are meant to model the binder pressure distribution caused by individual punctual forces, such as the ones applied by cylinders. The local areas of the binder where these punctual forces are defined, are considered rigid. Furthermore, the opposite tool must be rigid also or else this model cannot be selected. For cushion pins, similar to columns, a point of application must be specified to locate each pin. However, this model applies the total force for the whole tool and maintains it independently of the number of selected pins. Since the opposite tool can be either force or spring controlled, this model simulates the local elastic behavior of the binder due to localized pressure.

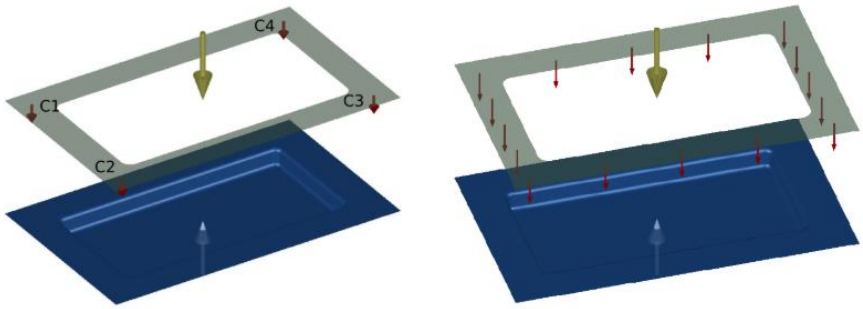

Figure 2.5. Rectangular cup with applied forces of type columns (left) and cushion pins (right) (*AutoForm® R8 software manual*, 2018).

An example showing the application of columns and cushion pins on a simple rectangular cup is shown in Figure 2.5. The forces considered for the columns types are $C1 = C2$ and $C3 = C4$, with $C4 > C1$. The effect of these models as well as the uniform loading are shown in Figure 2.6. The pressure rises from green to red color. The blue area has no applied pressure. Note that if the forces C1 to C4 were all equal, then the columns pressure distribution would be the same as the uniform loading. Also, for non-uniform loadings, tool tilting may occur. This is apparent from the previous columns scenario where the pressure is clearly going to create a tilting moment. This is a disadvantage of using a uniform loading, since the software cannot predict this phenomenon. Although its magnitude is effectively small it can influence material flow by altering the pressure distribution.

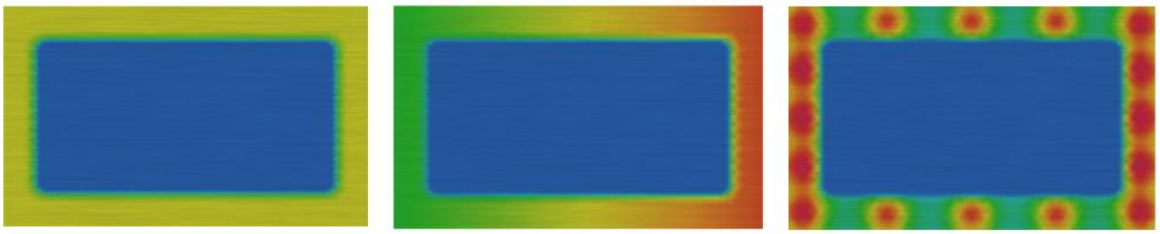

Figure 2.6. Rectangular cup with uniform pressure (left), columns (middle) and with cushion pins (right) (*AutoForm® R8 software manual*, 2018).

In some cases, in order to better reproduce the forming conditions, it is also necessary to add spacers to the model. They help control the pressure application and its distribution, representing balancing or equalizer blocks used in real tooling. They work between the binder and its opposite tool, taking some binder force in the process. To define them, their location, thickness increment relative to the blank and stiffness are needed. The thickness increment establishes the initial gap created by the spacers. It can be set so that the gap has the sheet's thickness, a higher or lower value. The stiffness defines how this gap decreases along the process, with the binder force increase. If the stiffness is too high, AutoForm® recommends an approximation with an elastic beam, although it warns that the spacer stiffness is not only influenced by the spacer itself but also by any mounting parts and the tools themselves.

2.3.2.1. Force Evolution

For force and spring controlled tools there are two ways to define how the binder force evolves during the process. These definitions are valid for all models and whether a

punctual or a global value is defined. The simplest procedure is to prescribe a constant force throughout the cushion stroke. The other is to define a variable force with a linear increase. For force controlled tools this requires only the initial and final values. Spring controlled tools also have two parameters, the preload force and the spring stiffness. Note that if only the preload force is defined, the tools will act with a constant force. The spring stiffness gives the linear slope of the spring force behavior. When defining all these force values the user must take into account the drawbead's uplift force. For force controlled tools an alternative exists, which involves the selection of an initial pressure. The software automatically calculates the corresponding constant force value considering the blank area beneath the binder.

2.3.3. Contact and Friction

Contact is controlled via a search algorithm that detects if there is any node of the sheet penetrating the tools, in order to correct the nodes' position. The contact constraints are determined with the penalty method. The algorithm is controlled by two non-user defined parameters. The *max penetration tolerance* gives the maximum allowed nodal penetration that can be accepted. The *distance error* defines the minimum distance for which contact is assumed to occur. Furthermore, the user must define for each tool which side of the sheet it will contact, upper or lower. The contact search will not work for the non-selected side. For EPS the software uses the current sheet thickness, detecting small gaps that may exist from, for example, material thinning.

Friction is calculated based on the well-known Coulomb's dry friction law.

$$cof = \frac{F_{\mathrm{R}}}{F_{\mathrm{N}}}. \tag{2.10}$$

where cof is the coefficient of friction, F_{N} the normal force and F_{R} the shear force due to friction. The friction shear stress can be obtained with the normal stress or pressure, p, applied on the same contact area as:

$$\tau_{\mathrm{R}} = cof\ p. \tag{2.11}$$

The cof is dependent on the combination of materials of the sheet and tools, as well as the lubricant used in the process. However, it is a typical simplification to consider the cof as constant. In reality, various factors such as sliding velocity, contact pressure and

even the direction in which the friction force is applied can influence this value. One of the strategies used in the software is to consider the influence of the contact pressure. The effective coefficient of friction is given by:

$$cof_{\text{eff}} = cof\ \left(\frac{p}{p_{\text{ref}}}\right)^{e-1}. \tag{2.12}$$

2.4. Material Generator and Editor

AutoForm® R8 has a dedicated material generator that allows the user to create a material file from scratch or edit an existing one. General information about the material needs to be provided, such as its material class, specific weight, Young's modulus, Poisson's ratio, volumetric heat capacity and conductivity. Then, information gathered from experimental tests should be used to define the constitutive model, namely the yield criterion, the hardening law and the forming limit curve.

2.4.1. Yield Criterion

The yield criterion is the condition that must be satisfied in order for plastic deformation to occur. It is a function that expresses, for all stress states, the yielding condition. In a general sense it can be defined by:

$$\Phi(\sigma_{ij}, Y) \equiv \bar{\sigma}(\sigma_{ij}) - Y = 0. \tag{2.13}$$

where $\bar{\sigma}(\sigma_{ij})$ is the equivalent stress and Y is the yield stress, given by the hardening law. This function is represented in the principal stress three-dimensional space by a surface, inside of which the material exhibits an elastic state and a plastic state if located on the surface. Typically, for sheet metal forming only the components of stress acting on the blank surface are considered relevant, i.e. plane stress conditions are considered, with $\sigma_{zz} = \sigma_{xz} = \sigma_{yz} = 0$. This reduces the representation to a yield curve in the plane of the principal stresses.

An associate flow rule is adopted to define the increment of the plastic strain rate, $d\varepsilon_{ij}^{\text{p}}$. Following Drucker's normality principle, where $d\lambda \geq 0$ acts as a scalar multiplier, it can be written:

$$d\varepsilon_{ij}^{\text{p}} = d\lambda \frac{\partial \Phi}{\partial \sigma_{ij}}. \tag{2.14}$$

The yield stress Y is independent of the stress tensor. Knowing this and according to equation (2.13), the partial derivatives of the stress function Φ with respect to the planar components of stress can be given by the respective partial derivatives of the equivalent stress $\bar{\sigma}$.

$$d\varepsilon_{ij}^{\mathrm{p}} = d\lambda \frac{\partial \bar{\sigma}}{\partial \sigma_{ij}}. \tag{2.15}$$

Due to its additional complexity and importance in forming operations, the yield criteria will be given more detail in the next chapter.

2.4.2. Hardening Law

The hardening law describes the strain hardening behavior of the material during plastic deformation. Phenomenological models are typically used to approximate the observed hardening or flow curves for each material. These can be defined with the information gathered from tensile tests. They capture the non-linear increase of stress with plastic deformation that occurs for the majority of metals, including steel. AutoForm® defines the flow curve with three different methods, either by using the phenomenological equations, by a table of true stress-strain data points or by approximation, all in respect to the rolling direction.

The available equations to define the yield stress in function of the equivalent plastic strain evolution ε^{p} are the following:

Ludwick $$Y = K\varepsilon^{n}, \tag{2.16}$$

Swift $$Y = C(\varepsilon_0 + \varepsilon^{\mathrm{p}})^{m}, \tag{2.17}$$

Ghosh $$Y = C(\varepsilon_0 + \varepsilon^{\mathrm{p}})^{m} - D, \tag{2.18}$$

Hockett-Sherby $$Y = \sigma_{\mathrm{sat}} - (\sigma_{\mathrm{sat}} - \sigma_i)e^{-a(\varepsilon^{\mathrm{p}})^{p}}, \tag{2.19}$$

Swift / Hockett-Sherby $$Y = (1-\alpha)[C(\varepsilon_0 + \varepsilon^{\mathrm{p}})^{m}] + \alpha\left[\sigma_{\mathrm{sat}} - (\sigma_{\mathrm{sat}} - \sigma_i)e^{-a(\varepsilon^{\mathrm{p}})^{p}}\right], \tag{2.20}$$

Yoshida-Uemori $$Y = (1-\alpha)\left[Y + R_{\mathrm{sat}}\left(1 - e^{-m\varepsilon^{\mathrm{p}}}\right)\right] + \alpha[C(\varepsilon_0 + \varepsilon^{\mathrm{p}})^{n}], \tag{2.21}$$

ThyssenKrupp Extrapolation Method $$Y = \alpha[C(\varepsilon_0 + \varepsilon^{\mathrm{p}})^{m}] + (1-\alpha)\left[\sigma_{\mathrm{sat}} - (\sigma_{\mathrm{sat}} - \sigma_i)e^{-a\varepsilon^{\mathrm{p}}}\right], \tag{2.22}$$

where all other variables correspond to material parameters.

The table and approximation methods have similar procedures since both need the data points provided by tensile tests. The table needs the information of up to 50 pairs of these points in an ASCII file, previously selected by the user, interpolating the points directly, whereas the approximation can take up to 100000 pairs in a .dat file format. It then determines, automatically, the parameters for the Swift/Hockett-Sherby approximation. The user can tweak the fit of the curve by altering the weight factor α or by providing more information, like the yield stress.

The software considers an isotropic hardening rule by default. This means that, after yielding, the yield curve will expand proportionally in all directions in the principal stress plane.

2.4.3. Forming Limit Curve

The Forming Limit Curve (FLC) is the most well-known tool to perform the analysis of sheet metal forming processes. The FLC can be experimentally obtained, following the international standard ISO 12004-2, and it represents the failure limits for different monotonic loadings in the principal in-plane strain's domain. The experimental tests recommended for its determination are the Marciniak and the Nakajima, which main difference is the geometry of the punch, as shown in Figure 2.7. The Marciniak test uses a cylindrical punch that comes in contact with a carrier blank. This blank possesses a central circular hole and its main goal is to avoid contact with friction between the punch and the specimen. The Nakajima test uses a hemispherical punch, which comes into direct contact with the metal sheet. Both of these tests use a binder and die firmly clamped together to promote deformation and avoid slippage. By variating the sheet width, it is possible to attain the various strain states necessary to describe the FLC.

Although practical and useful, this approach comes with its own flaws. The main one results from the fact that the strain paths represented by these tests are almost-linear and involve no elastic recovery. Therefore, this type of Forming Limit Diagram (FLD) can be referred to as static. Its application in the analysis of complex forming processes, such as deep drawing, can lead to erroneous results. In practical terms, it is known that the change in the strain path corresponds to a shift in the position of the FLC in its domain, i.e. the FLC is strain path dependent. Therefore, whenever a strain state is attained resultant of non-linear

strain paths the FLD prediction can be wrong, either by underestimating or overestimating the limit (Ofenheimer *et al.*, 2008).

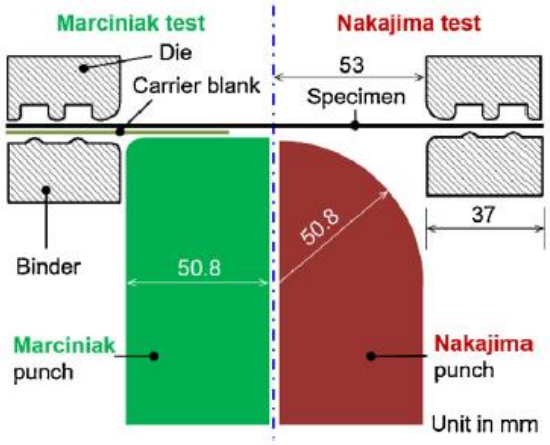

Figure 2.7. Schematic representation of Marciniak and Nakajima tests (Volk *et al.*, 2019).

Several authors proposed the use of stress-based criteria as an alternative to the strain based FLC. These formability criteria are the basis for the Forming Limit Stress Curve (FLSC). Its main advantage is the fact that the stress required to attain strain localization or fracture is not strain path dependent. However, since strain is the only physical measurable quantity, this approach becomes overly dependent on the stress-strain relationship adopted to define the formability criterion. Furthermore, its dependence on the hardening model constitutes another problem. Points with high strain rate and slow rising stress, due to the material hardening behavior, will necessarily be susceptible to error due to the poor resolution in the stress domain. This type of behavior is characteristic of necking, which may be one of the reasons why the FLSC concept as not overcome the FLC one.

Several options exist in AutoForm® R8 to define the FLC. Similar to the hardening law, a table with 50 principal strain pairs can be provided. Other methods include models like Keeler, Arcelor V9 and one developed by Tata Steel®.

3. ANISOTROPIC YIELD CRITERIA

Stamping and deep drawing are processes in which a flat sheet is deformed to create a myriad of complex parts. These blanks are cut from coils of sheet metal, obtained through a rolling process that promotes their anisotropic mechanical behavior. More specifically, the mechanical properties show symmetry in three orthogonal planes, which are characterized by three intersecting axes. One corresponds to the rolling direction (RD), where the crystallographic grains are aligned and stretched. Perpendicular to the RD, along the width of the sheet, is the transverse direction (TD). Finally, the third corresponds to the thickness or normal direction (ND), where the grains are compacted. Usually, a Oxyz coordinate system is used as reference (material axis), where x corresponds to RD, y to TD and z to ND.

The more traditional way to assess the different properties along the in-plane directions corresponds to performing tensile tests, with specimens cut at different orientations to the RD. Therefore, in this introductory section special attention will be given to the information extracted from this type of tests.

Let Y_θ be the analytical uniaxial yield stress along the direction which forms an angle of θ with respect to the RD. The components of the stress tensor in the material axis can be written as:

$$\sigma_{xx} = Y_\theta \cos^2\theta\,, \sigma_{yy} = Y_\theta \sin^2\theta\,, \sigma_{xy} = \sigma_{yx} = Y_\theta \sin\theta\cos\theta. \tag{3.1}$$

Accordingly, the equivalent stress with respect to θ can take the form:

$$\bar{\sigma}|_\theta = Y_\theta F_\theta, \tag{3.2}$$

where F_θ is a function that depends on the angle θ and is specific to the yield criterion considered. It follows that the planar yield stress can be given for whichever yield stress using the following relation:

$$Y_\theta = \frac{\bar{\sigma}|_\theta}{F_\theta} = \frac{Y}{F_\theta}, \tag{3.3}$$

The uniaxial tensile tests also allow to evaluate the Lankford value or anisotropy coefficient, r_θ, which is also used to study the plastic behavior of the material. It defines the

tangent to the yield curve for the corresponding loading direction. Its instantaneous value is defined by:

$$r_\theta = \frac{d\varepsilon^{\mathrm{p}}_{\theta+90}}{d\varepsilon^{\mathrm{p}}_{zz}}, \tag{3.4}$$

where $d\varepsilon^{\mathrm{p}}_{\theta+90}$ and $d\varepsilon^{\mathrm{p}}_{zz}$ represent the increment of plastic strain along the width and the thickness directions of the specimen, respectively. To relate this important parameter to the chosen yield criterion, the strain rate in its incremental form should be given in respect to the material axis:

$$d\varepsilon^{\mathrm{p}}_{\theta} = d\varepsilon^{\mathrm{p}}_{xx}\cos^2\theta + d\varepsilon^{\mathrm{p}}_{yy}\sin^2\theta + d\varepsilon^{\mathrm{p}}_{xy}\sin\theta\cos\theta. \tag{3.5}$$

Since the plastic deformation is considered to be an isochoric phenomenon, it is possible to define:

$$d\varepsilon^{\mathrm{p}}_{zz} = -\left(d\varepsilon^{\mathrm{p}}_{xx} + d\varepsilon^{\mathrm{p}}_{yy}\right). \tag{3.6}$$

Replacing equations (3.5) and (3.6) in equation (3.4):

$$r_\theta = \frac{d\varepsilon^{\mathrm{p}}_{xx}\cos^2\theta + d\varepsilon^{\mathrm{p}}_{yy}\sin^2\theta + d\varepsilon^{\mathrm{p}}_{xy}\sin\theta\cos\theta}{d\varepsilon^{\mathrm{p}}_{xx} + d\varepsilon^{\mathrm{p}}_{yy}} - 1. \tag{3.7}$$

Since the equivalent stress $\bar{\sigma}$ is a first-degree homogeneous function of the components of the Cauchy stress tensor σ_{ij}, Euler's identity gives:

$$\bar{\sigma}\left(\sigma_{ij}\right) = \sigma_{ij}\frac{\partial\bar{\sigma}}{\partial\sigma_{ij}}. \tag{3.8}$$

Taking the associated flow rule, defined in equation (2.15), into account, as well as equations (3.2) and (3.3):

$$r_\theta = \frac{1}{Y_\theta}\frac{\left(\sigma_{ij}\frac{\partial\bar{\sigma}}{\partial\sigma_{ij}}\right)\Big|_\theta}{\left(\frac{\partial\bar{\sigma}}{\partial\sigma_{xx}} + \frac{\partial\bar{\sigma}}{\partial\sigma_{yy}}\right)\Big|_\theta} - 1 = \frac{F_\theta}{\left(\frac{\partial\bar{\sigma}}{\partial\sigma_{xx}} + \frac{\partial\bar{\sigma}}{\partial\sigma_{yy}}\right)\Big|_\theta} - 1. \tag{3.9}$$

It is also common to define the average anisotropy coefficient or the coefficient of normal anisotropy as:

$$r_{\mathrm{m}} = \frac{r_0 + 2r_{45} + r_{90}}{4}, \tag{3.10}$$

where r_0, r_{45} and r_{90} correspond to the Lankford values evaluated with specimens oriented along RD, at 45º with RD and along TD, respectively.

Another loading condition that has become consensual to be important to access in order to properly describe the orthotropic behavior of metallic sheets is the in-plane equibiaxial one. For equibiaxial loading, where $\sigma_{xx} = \sigma_{yy} = \sigma_{\mathrm{b}}$ and $\sigma_{xy} = 0$, the anisotropy coefficient is defined by:

$$r_{\mathrm{b}} = \frac{d\varepsilon_{yy}^{\mathrm{p}}}{d\varepsilon_{xx}^{\mathrm{p}}} = \frac{d\varepsilon_{xx}^{\mathrm{p}} + d\varepsilon_{yy}^{\mathrm{p}}}{d\varepsilon_{xx}^{\mathrm{p}}} - 1. \tag{3.11}$$

In a similar fashion to the approach adopted for uniaxial loading, the equivalent yield stress for the equibiaxial loading, as well as the yield stress are defined to be:

$$\bar{\sigma}|_{\mathrm{b}} = Y_{\mathrm{b}} F_{\mathrm{b}}, \tag{3.12}$$

$$Y_{\mathrm{b}} = \frac{Y}{F_{\mathrm{b}}}, \tag{3.13}$$

where F_{b} is a function specific for the equibiaxial point. Based on the same assumptions mentioned previously, the anisotropy coefficient becomes:

$$r_{\mathrm{b}} = \frac{1}{Y_{\mathrm{b}}} \frac{\left(\sigma_{ij} \frac{\partial \bar{\sigma}}{\partial \sigma_{ij}}\right)\Big|_{\mathrm{b}}}{\left(\frac{\partial \bar{\sigma}}{\partial \sigma_{xx}}\right)\Big|_{\mathrm{b}}} - 1 = \frac{F_{\mathrm{b}}}{\left(\frac{\partial \bar{\sigma}}{\partial \sigma_{xx}}\right)\Big|_{\mathrm{b}}} - 1. \tag{3.14}$$

In the following subsections, some of the yield criterion available in AutoForm® and used in the context of this work will be described. It should be mentioned that all yield criteria are implemented in AutoForm® assuming plane stress conditions, even if their original formulation is 3D.

3.1. Hill 1948

Hill (1948) proposed a yield criterion that is still widely used thanks to the simple approach proposed to determine the parameters. In its original 3D formulation, it is expressed by the following quadratic function:

$$\begin{aligned} F\left(\sigma_{yy} - \sigma_{zz}\right)^2 + G(\sigma_{zz} - \sigma_{xx})^2 + H\left(\sigma_{xx} - \sigma_{yy}\right)^2 + 2L\sigma_{yz}^2 + 2M\sigma_{xz}^2 \\ + 2N\sigma_{xy}^2 = Y^2, \end{aligned} \tag{3.15}$$

where F, G, H, L, M and N are material parameters. Assuming the plane stress condition, equation (3.15) takes the form:

$$(G + H)\sigma_{xx}^2 - 2H\sigma_{xx}\sigma_{yy} + (H + F)\sigma_{yy}^2 + 2N\sigma_{xy}^2 = Y^2. \tag{3.16}$$

Taking equations (2.15) and (3.6) into account, the strain rate components can be expressed as:

$$\begin{aligned} d\varepsilon_{xx}^{\mathrm{p}} &= 2d\lambda\big[(G+H)\sigma_{xx} - H\sigma_{yy}\big], \\ d\varepsilon_{yy}^{\mathrm{p}} &= 2d\lambda\big[(H+F)\sigma_{yy} - H\sigma_{xx}\big], \\ d\varepsilon_{zz}^{\mathrm{p}} &= -2d\lambda\big[G\sigma_{xx} + F\sigma_{yy}\big], \\ d\varepsilon_{xy}^{\mathrm{p}} &= 4d\lambda N\sigma_{xy}. \end{aligned} \tag{3.17}$$

By applying this knowledge in equation (3.7) and (3.11) it is possible to define:

$$\begin{aligned} r_\theta &= \frac{H + (2N - F - G - 4H)\cos^2\theta \sin^2\theta}{F\sin^2\theta + G\cos^2\theta}, \\ r_{\mathrm{b}} &= \frac{F}{G}. \end{aligned} \tag{3.18}$$

Then, following relations for the anisotropy coefficients can be promptly written:

$$r_0 = \frac{H}{G}, r_{90} = \frac{H}{F}, r_{45} = \frac{N}{F+G} - \frac{1}{2}, r_{\mathrm{b}} = \frac{r_0}{r_{90}}. \tag{3.19}$$

If the orthotropic axes coincide with the stress tensor's principal axes, then equation (3.16) changes to:

$$(G+H)\sigma_{11}^2 - 2H\sigma_{11}\sigma_{22} + (H+F)\sigma_{22}^2 = Y^2. \tag{3.20}$$

Considering, as reference, that the moment of yielding during a tensile test performed in RD, makes $Y = \sigma_0$, then $(G+H) = 1$. This means that the parameter H becomes $H = r_0/(1+r_0)$ and the following equation can be deduced for the yield locus:

$$\sigma_0^2 = \frac{r_0 r_{90}(\sigma_{11} - \sigma_{22})^2 + r_{90}\sigma_{11}^2 + r_0\sigma_{22}^2}{r_{90}(r_0+1)}. \tag{3.21}$$

This expression shows that only three inputs (σ_0, r_0 and r_{90}) are needed to define the yield *locus* in the principal stress domain. It should be noted that the same principle can be applied for the TD. This gives a similar expression where the yield stress in the TD is used instead, with $Y = \sigma_{90}$. In this case $H = r_{90}/(1+r_{90})$ and $(H+F) = 1$, giving:

$$\sigma_{90}^2 = \frac{r_0 r_{90}(\sigma_{11} - \sigma_{22})^2 + r_{90}\sigma_{11}^2 + r_0\sigma_{22}^2}{r_0(r_{90}+1)}. \tag{3.22}$$

It is important to mention that the yield surfaces defined by equation (3.21) and (3.22) will most likely be different, because this criterion is not flexible enough to describe both the Lankford values and the yield stress.

In order to perform the finite element analysis, the yield criterion must be defined in the orthotropic axis, as shown in equation (3.16). Therefore, in order to fully define the yield surface, the Lankford value in the 45º direction must also be known. In total, only four experimental values are needed, making it an easy criterion to implement in commercial software.

Nevertheless, if more experimental values are known, it is important to understand how well they are being approximated. This justifies the importance of evaluating also the values of the normalized yield stress in plane strain, pure shear and equibiaxial stress. The normalization is performed considering the yield stress for uniaxial tension along the RD, since the condition $(G + H) = 1$ is commonly adopted.

For the equibiaxial point, where $\sigma_{11} = \sigma_{22} = \sigma_{\mathrm{b}}$, the criterion gives:

$$\frac{\sigma_{\mathrm{b}}}{\sigma_0} = \sqrt{\frac{r_{90}(r_0 + 1)}{(r_0 + r_{90})}}. \tag{3.23}$$

For plane strain, the strain ratio defined as $\rho = \left(d\varepsilon_1^{\mathrm{p}}/d\varepsilon_2^{\mathrm{p}}\right) = 0$. This leads to the relation:

$$\sigma_{11} = \left(1 + \frac{1}{r_{90}}\right)\sigma_{22}. \tag{3.24}$$

Thus, using equation (3.21) and (3.22), the normalized plane strain points relative to RD and TD, are respectively:

$$\frac{\sigma_{\mathrm{ps}_0}}{\sigma_0} = \left(1 + \frac{1}{r_{90}}\right)\sqrt{\frac{r_{90}(r_0 + 1)}{\frac{r_0}{r_{90}} + r_0 + r_{90}\left(1 + \frac{1}{r_{90}}\right)^2}}, \tag{3.25}$$

$$\frac{\sigma_{\mathrm{ps}_{90}}}{\sigma_0} = \left(1 + \frac{1}{r_{90}}\right)\sqrt{\frac{r_0(r_{90} + 1)}{r_{90}(r_0 + 1)}}\sqrt{\frac{r_0(r_{90} + 1)}{\frac{r_0}{r_{90}} + r_0 + r_{90}\left(1 + \frac{1}{r_{90}}\right)^2}}. \tag{3.26}$$

Finally, for pure shear $\sigma_{11} = -\sigma_{22}$ and:

$$\frac{\sigma_{\mathrm{shear}}}{\sigma_0} = \sqrt{\frac{r_{90}(r_0 + 1)}{4r_0 r_{90} + r_0 + r_{90}}}. \tag{3.27}$$

Note that, in this specific case, symmetry exists for the shear performed with the specimen oriented along RD and TD.

This classic yield criterion shows various advantages, some of which were already mentioned. In particular, the direct physical meaning of its parameters facilitates its

understanding. The main drawback is related to its quadratic formulation. This reduces its flexibility, disabling the simultaneous correct definition of the plane strain, shear and equibiaxial points, particularly for highly anisotropic materials or materials that show what is called the anomalous behavior. In fact, when using this criterion, if $r_{\mathrm{m}} < 1$, the yield *locus* is located inside the one given by von Mises; while if $r_{\mathrm{m}} > 1$ it will be outside the von Mises yield *locus*. Some materials (in particular aluminum alloys) have the yield *locus* outside the von Mises surface, though their r_{m}-coefficient is lower than one. To counter this problem, AutoForm® introduces a biaxial stress factor, Biax, to expand or contract the Hill yield locus at the equibiaxial stress point by a desired magnitude. The Biax value can be interpreted as a factor to increase the impact of the equibiaxial yield stress on the yield surface. However, in order to enable the change of this point the anisotropy parameters must be calculated taking σ_{b} into account and not using only the Lankford values. To manage this transformation an approximation to the Hill'90 criterion is made. Although the AutoForm® manual does not give an explanation to the strategy adopted, according to Banabic (2010), since this yield criterion is no longer quadratic the exponent m can be determined as follows:

$$m = \frac{\ln[2(r_{45} + 1)]}{\ln[2\sigma_{\mathrm{b}}/\sigma_{45}]}. \tag{3.28}$$

Naturally this also changes the position of the plane strain and shear points.

3.2. BBC 2005

Banabic, Balan and Comsa proposed in 2005 an advanced anisotropic yield criterion whose main objective was to provide a more accurate representation of the anisotropic behavior of several materials used by the automotive and aeronautical industry, like Dual Phase, Complex Phase and TRIP steels, aluminum and magnesium alloys, to name a few (Banabic, 2010). This criterion defines the equivalent stress by:

$$\bar{\sigma} = [a(\Lambda + \Gamma)^{2k} + a(\Lambda - \Gamma)^{2k} + b(\Lambda + \Psi)^{2k} + b(\Lambda - \Psi)^{2k}]^{\frac{1}{2k}}, \tag{3.29}$$

where $k \in \mathbb{N} \geq 1$ and a, $b > 0$ are material parameters. These conditions ensure the convexity of the yield surface. Λ, Γ and Ψ are functions of further material parameters, L, M, N, P, Q and R, as well as the components of the Cauchy stress tensor.

$$\Lambda = \sqrt{\left(N\sigma_{xx} - P\sigma_{yy}\right)^2 + \sigma_{xy}\sigma_{yx}}, \tag{3.30}$$

$$\Gamma = L\sigma_{xx} + M\sigma_{yy},$$

$$\Psi = \sqrt{\left(Q\sigma_{xx} - R\sigma_{yy}\right)^2 + \sigma_{xy}\sigma_{yx}}.$$

So, nine material parameters are needed to define this criterion. However, only eight need to be determined through experiments, since the exponent k depends on the crystallographic structure of the studied material. The authors recommend the standard values of $k = 3$ and $k = 4$ for BCC and FCC materials, respectively. Likewise, these structures correspond to steels and aluminum alloys. Nevertheless, the authors also mention that this exponent can be altered to best fit the material behavior. This stems from the fact that the standard values agree with initial studies performed for isotropic materials and not anisotropic. For example, An *et al.*, (2011) found that for the high strength steels HC220YD and HC340LAD, the exponent should be approximately $2k = 5.35$ and $2k = 5.58$ respectively.

The majority of the experimental data needed comes from uniaxial tensile tests, namely the uniaxial yield stresses in the 0º, 45º and 90º directions, relative to RD, as well as the respective anisotropic coefficients. The equibiaxial yield stress and anisotropy coefficient are also needed. These can be obtained, for example, from compression or bulge tests. This criterion enables the reproduction of these experimental points, since the material parameters can be determined to fit them (number of parameters is equal to the number of experimental points).

The partial derivatives of the stress function Φ with respect to the planar components of stress are needed to define the flow rule. Note that in this case:

$$\frac{\partial \Phi}{\partial \sigma_{ij}} = \frac{\partial \bar{\sigma}}{\partial \sigma_{ij}} = \frac{\partial \bar{\sigma}}{\partial \Lambda}\frac{\partial \Lambda}{\partial \sigma_{ij}} + \frac{\partial \bar{\sigma}}{\partial \Gamma}\frac{\partial \Gamma}{\partial \sigma_{ij}} + \frac{\partial \bar{\sigma}}{\partial \Psi}\frac{\partial \Psi}{\partial \sigma_{ij}}. \tag{3.31}$$

The explicit expressions of the derivatives are given in ANNEX B.1. These equations enable the definition of the flow rule (equation (2.15)) as a function of the stress components. Now, a relationship between the various experimental parameters and the stress components must be achieved. For dealing with the results from the uniaxial tensile tests, a transformation of Λ, Γ and Ψ is necessary.

$$\Lambda = Y_\theta \Lambda_\theta, \Gamma = Y_\theta \Gamma_\theta, \Psi = Y_\theta \Psi_\theta, \tag{3.32}$$

with

$$\Lambda_\theta = \sqrt{(N\cos^2\theta - P\sin^2\theta)^2 + \sin^2\theta\cos^2\theta}, \tag{3.33}$$

$$\Gamma_\theta = L\cos^2\theta + M\sin^2\theta,$$
$$\Psi_\theta = \sqrt{(Q\cos^2\theta - R\sin^2\theta)^2 + \sin^2\theta\cos^2\theta}.$$

To obtain the equivalent stress defined in equation (3.2), the function F_θ takes the form:

$$F_\theta = [a(\Lambda_\theta + \Gamma_\theta)^{2k} + a(\Lambda_\theta - \Gamma_\theta)^{2k} + b(\Lambda_\theta + \Psi_\theta)^{2k} + b(\Lambda_\theta - \Psi_\theta)^{2k}]^{\frac{1}{2k}}. \quad (3.34)$$

Starting the correlation with the anisotropy coefficients, from equation (3.9):

$$\left(\frac{\partial\bar{\sigma}}{\partial\sigma_{xx}} + \frac{\partial\bar{\sigma}}{\partial\sigma_{yy}}\right)\Big|_\theta = \frac{\partial\bar{\sigma}}{\partial\Lambda}\Big|_\theta \left(\frac{\partial\Lambda}{\partial\sigma_{xx}} + \frac{\partial\Lambda}{\partial\sigma_{yy}}\right)\Big|_\theta + \frac{\partial\bar{\sigma}}{\partial\Gamma}\Big|_\theta \left(\frac{\partial\Gamma}{\partial\sigma_{xx}} + \frac{\partial\Gamma}{\partial\sigma_{yy}}\right)\Big|_\theta + \frac{\partial\bar{\sigma}}{\partial\Psi}\Big|_\theta \left(\frac{\partial\Psi}{\partial\sigma_{xx}} + \frac{\partial\Psi}{\partial\sigma_{yy}}\right)\Big|_\theta. \quad (3.35)$$

The explicit expressions for the derivatives are given in ANNEX B.1, enabling the definition of G_θ, such that:

$$\left(\frac{\partial\bar{\sigma}}{\partial\sigma_{xx}} + \frac{\partial\bar{\sigma}}{\partial\sigma_{yy}}\right)\Big|_\theta = \frac{G_\theta}{{F_\theta}^{2k-1}}, \quad (3.36)$$

resulting in a formula for the anisotropy coefficients with respect to the angle θ:

$$r_\theta = \frac{{F_\theta}^{2k}}{G_\theta} - 1. \quad (3.37)$$

For the equibiaxial anisotropy coefficient, the components of the stress tensor are $\sigma_{xx} = \sigma_{yy} = Y_\mathrm{b}$ and $\sigma_{xy} = \sigma_{yx} = 0$. Therefore, the functions Λ, Γ and Ψ become:

$$\Lambda = Y_\mathrm{b}\Lambda_\mathrm{b}, \Gamma = Y_\mathrm{b}\Gamma_\mathrm{b}, \Psi = Y_\mathrm{b}\Psi_\mathrm{b}, \quad (3.38)$$

with

$$\Lambda_\mathrm{b} = \sqrt{(N-P)^2} = |N-P|,$$
$$\Gamma_\mathrm{b} = L + M, \quad (3.39)$$
$$\Psi_\mathrm{b} = \sqrt{(Q-R)^2} = |Q-R|,$$

and

$$F_\mathrm{b} = [a(\Lambda_\mathrm{b} + \Gamma_\mathrm{b})^{2k} + a(\Lambda_\mathrm{b} - \Gamma_\mathrm{b})^{2k} + b(\Lambda_\mathrm{b} + \Psi_\mathrm{b})^{2k} + b(\Lambda_\mathrm{b} - \Psi_\mathrm{b})^{2k}]^{\frac{1}{2k}}. \quad (3.40)$$

From equation (3.14):

$$\left(\frac{\partial\bar{\sigma}}{\partial\sigma_{xx}}\right)\Big|_\mathrm{b} = \frac{\partial\bar{\sigma}}{\partial\Lambda}\Big|_\mathrm{b} \left(\frac{\partial\Lambda}{\partial\sigma_{xx}}\right)\Big|_\mathrm{b} + \frac{\partial\bar{\sigma}}{\partial\Gamma}\Big|_\mathrm{b} \left(\frac{\partial\Gamma}{\partial\sigma_{xx}}\right)\Big|_\mathrm{b} + \frac{\partial\bar{\sigma}}{\partial\Psi}\Big|_\mathrm{b} \left(\frac{\partial\Psi}{\partial\sigma_{xx}}\right)\Big|_\mathrm{b}. \quad (3.41)$$

The partial derivatives of the equivalent stress with respect to Λ_b, Γ_b and Ψ_b are identical to the ones presented in ANNEX B.1, with θ being substituted for b. The remaining are given also in ANNEX B.1, enabling the definition of G_b such that:

$$r_b = \frac{{F_b}^{2k}}{G_b} - 1. \tag{3.42}$$

The conditions related to the yield stresses are defined with the help of the normalized values of the experimental yield stresses:

$$y_\theta = \frac{Y}{Y_\theta}, y_b = \frac{Y}{Y_b}, \tag{3.43}$$

with

$${F_\theta}^{2k} = {y_\theta}^{2k}, {F_b}^{2k} = {y_b}^{2k}. \tag{3.44}$$

Equations (3.37) and (3.42) can also be written in the form:

$$G_\theta = \frac{1}{r_\theta + 1}{y_\theta}^{2k}, G_b = \frac{1}{r_b + 1}{y_b}^{2k}. \tag{3.45}$$

Equations (3.44) and (3.45) define eight non-linear functions that can be presented.

$$\begin{gathered}
a(N+L)^{2k} + a(N-L)^{2k} + b(N+Q)^{2k} + b(N-Q)^{2k} = {y_0}^{2k}, \\
a\left[\sqrt{(N-P)^2+1} + L + M\right]^{2k} + a\left[\sqrt{(N-P)^2+1} - L - M\right]^{2k} \\
+ b\left[\sqrt{(N-P)^2+1} + \sqrt{(Q-R)^2+1}\right]^{2k} \\
+ b\left[\sqrt{(N-P)^2+1} - \sqrt{(Q-R)^2+1}\right]^{2k} = {y_{45}}^{2k}, \\
a(P+M)^{2k} + a(P-M)^{2k} + b(P+R)^{2k} + b(P-R)^{2k} = {y_{90}}^{2k}, \\
a(N-P+L+M)^{2k} + a(N-P-L-M)^{2k} + b(N-P+Q-R)^{2k} \\
+ b(N-P-Q+R)^{2k} = {y_b}^{2k}, \\
a(P-M)(N+L)^{2k-1} + a(P+M)(N-L)^{2k-1} + b(P+R)(N+Q)^{2k-1} \\
+ b(P-R)(N-Q)^{2k-1} = \frac{r_0}{r_0+1}{y_0}^{2k},
\end{gathered} \tag{3.46}$$

$$
\begin{aligned}
a\sqrt{(Q-R)^2+1}\Big\{&\Big[\sqrt{(N-P)^2+1}+L+M\Big]^{2k-1}\\
&+\Big[\sqrt{(N-P)^2+1}-L-M\Big]^{2k-1}\Big\}\\
&+b\Big\{\Big[\sqrt{(N-P)^2+1}+\sqrt{(Q-R)^2+1}\Big]^{2k}\\
&+\Big[\sqrt{(N-P)^2+1}-\sqrt{(Q-R)^2+1}\Big]^{2k}\Big\}\\
&=\sqrt{(N-P)^2+1}\sqrt{(Q-R)^2+1}\,\frac{r_{45}+0.5}{r_{45}+1}(2y_{45})^{2k},\\
a(N-L)(P+M)^{2k-1}&+a(N+L)(P-M)^{2k-1}+b(N+Q)(P+R)^{2k-1}\\
&+b(N-Q)(P-R)^{2k-1}=\frac{r_{90}}{r_{90}+1}{y_{90}}^{2k},\\
a(N+L)(N-P+L+M)^{2k-1}&+a(N-L)(N-P-L-M)^{2k-1}\\
&+b(N+Q)(N-P+Q-R)^{2k-1}\\
&+b(N-Q)(N-P-Q+R)^{2k-1}=\frac{1}{r_b+1}{y_{\mathrm{b}}}^{2k}.
\end{aligned}
$$

Since these functions are non-linear, the Newton's Method is applied to determine the unknown anisotropy parameters, a, b, L, M, N, P, Q and R. This method demands for the user to define an initial solution for the anisotropy parameters and since it is a non-linear system of equations, it can lead to different solutions. In this context, the authors recommend that the parameters should be bigger than zero. It is important to mention that if parameter k is included in the set of unknowns, then there will be 9 parameters to determine with only 8 equations. In that case, it is necessary to define a minimization problem, which will try to find the set of anisotropy parameters that minimize the error between the yield criterion and the experimental values.

The possibility of using the Biax parameter is also enabled for this criterion. It is easy to implement since it multiplies y_{b} directly in the fourth and last of the equations (3.46). A new set of parameters is determined to define the transformed yield *locus*.

3.3. Vegter Model

Vegter and Van Den Boogaard (2006) proposed an adaptable advanced anisotropic yield criterion using second-order Bézier functions. The 2D yield curve is

divided into several segments. The two extremity points of each segment correspond to different stress conditions imposed by the experimental tests. These two serve as reference points $\vec{\sigma}_i$ and $\vec{\sigma}_j$ that, together with a hinge point $\vec{\sigma}_h$, define the yield curve locally, with:

$$\vec{\sigma}_{locus} = (1-\mu)^2\vec{\sigma}_i + 2\mu(1-\mu)\vec{\sigma}_h + \mu^2\vec{\sigma}_j, \tag{3.47}$$

where μ is the Bézier interpolation factor defined such that $0 \leq \mu \leq 1$, as shown in Figure 3.1.

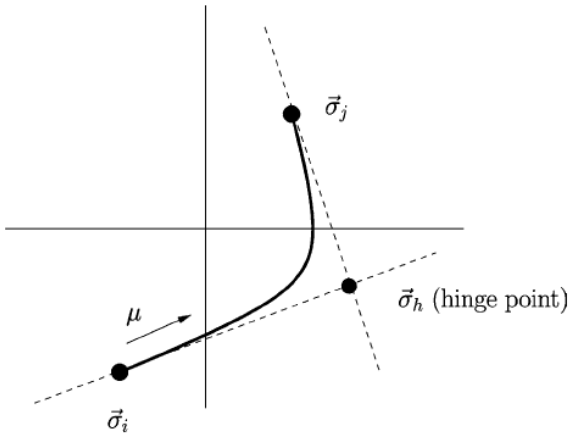

Figure 3.1. Bézier curve defined with two reference points and one hinge point (Vegter and Van Den Boogaard, 2006).

Note that differentiating with respect to μ shows that, at $\mu = 0$ and $\mu = 1$, the Bézier curve has a tangent defined by the vectors $(\vec{\sigma}_h - \vec{\sigma}_i)$ at $\vec{\sigma}_i$ and $\left(\vec{\sigma}_j - \vec{\sigma}_h\right)$ at $\vec{\sigma}_j$, respectively. Therefore, the yield function is continuously differentiable and assembling all the segments forms a smooth, convex, yield *locus* characteristic of polycrystalline metallic materials, as schematically shown in Figure 3.2. The associated flow rule dictates that the strain rate direction must be coaxial with the normal of the yield curve, so it also defines its tangent.

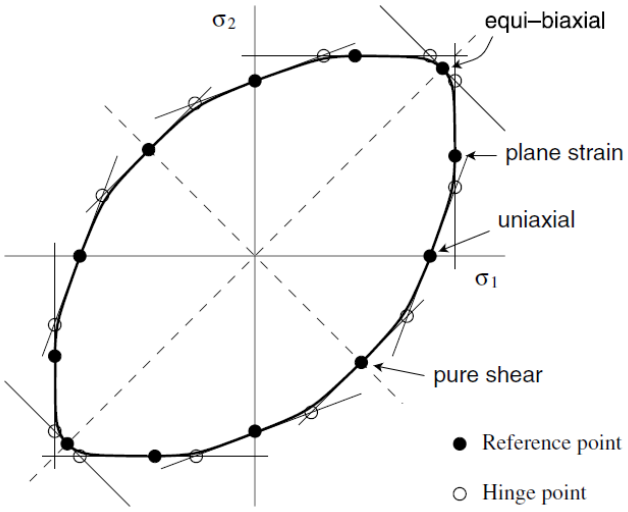

Figure 3.2. Bézier curve defined with two reference points and one hinge point (altered) (Vegter and Van Den Boogaard, 2006).

The normalized interpolation function can be written as:

$$\vec{F} = (1-\mu)^2\vec{A} + 2\mu(1-\mu)\vec{B} + \mu^2\vec{C}, \tag{3.48}$$

with $\vec{A}$ and $\vec{C}$ being the normalized reference stress points, depending on the segment, and $\vec{B}$ the corresponding hinge point. This enables defining the principal stress vector $\vec{\sigma}$ as:

$$\vec{\sigma} = \bar{\sigma}\vec{F}. \tag{3.49}$$

The reference points and their respective normal depend on the angle formed between the RD and the first principal stress direction, γ. Considering the symmetries that exist for orthotropic materials, a Fourier series can be used to interpolate the normalized yield curve considering γ. First, rotating a specimen by 180º gives the same stress state, so $\vec{F}(\gamma) = \vec{F}(\gamma+\pi)$. Symmetry also exists for $\gamma = 0$ and $\gamma = \pi/2$, giving $\vec{F}(\gamma) = \vec{F}(-\gamma)$ and $\vec{F}(\gamma+\pi/2) = \vec{F}(-\gamma+\pi/2)$. To fulfill these conditions, only the even terms of a cosine function can be used. Both the values of stress and the gradients associated with them are needed, so the same formulation applies to the strain ratios. The following Fourier series is adopted:

$$\vec{F}_{\mathrm{k}}(\gamma) = \sum_{m=0}^{n} \vec{\varphi}_{\mathrm{k}_m} \cos 2m\gamma, \tag{3.50}$$

$$\rho_{\mathrm{un}}(\gamma) = \sum_{m=0}^{n} \varrho_m \cos 2m\gamma. \tag{3.51}$$

$\vec{\varphi}_{\mathrm{k}m}$ and ϱ_m are Fourier parameters and n is the total number of tests minus 1; i.e. it is the number of cosine terms used for the expansion of the reference points and/or strain vectors. Note that index k is associated with the type of test performed and un in equation (3.51) corresponds to the uniaxial tensile test. The yield *locus* is fully defined with these Fourier series which approximate the various Bézier curves.

Let the Vegter yield function be defined in the principal stress space by $\boldsymbol{X} = \{\sigma_{11}, \sigma_{22}, \cos 2\gamma\}$. In order to find the strain rate direction, a relation between the stress state components and $\boldsymbol{X}$ must be obtained from:

$$\begin{aligned}
\sigma_{11} &= \frac{1}{2}\left(\sigma_{xx} + \sigma_{yy} + \sqrt{\left(\sigma_{xx} - \sigma_{yy}\right)^2 + 4\sigma_{xy}^2}\right), \\
\sigma_{22} &= \frac{1}{2}\left(\sigma_{xx} + \sigma_{yy} - \sqrt{\left(\sigma_{xx} - \sigma_{yy}\right)^2 + 4\sigma_{xy}^2}\right), \\
\cos 2\gamma &= \frac{\sigma_{xx} - \sigma_{yy}}{\sqrt{\left(\sigma_{xx} - \sigma_{yy}\right)^2 + 4\sigma_{xy}^2}} = \frac{\sigma_{xx} - \sigma_{yy}}{\sigma_{11} - \sigma_{22}}, \\
\sin 2\gamma &= \frac{2\sigma_{xy}}{\sqrt{\left(\sigma_{xx} - \sigma_{yy}\right)^2 + 4\sigma_{xy}^2}} = \frac{2\sigma_{xy}}{\sigma_{11} - \sigma_{22}}.
\end{aligned} \tag{3.52}$$

Making $c \equiv \cos 2\gamma$ and $s \equiv \sin 2\gamma$ as a simplification, from these equations:

$$\frac{\partial \boldsymbol{X}}{\partial \boldsymbol{\sigma}} = \begin{bmatrix} \frac{\partial \sigma_{11}}{\partial \sigma_{xx}} & \frac{\partial \sigma_{11}}{\partial \sigma_{yy}} & \frac{\partial \sigma_{11}}{\partial \sigma_{xy}} \\ \frac{\partial \sigma_{22}}{\partial \sigma_{xx}} & \frac{\partial \sigma_{22}}{\partial \sigma_{yy}} & \frac{\partial \sigma_{22}}{\partial \sigma_{xy}} \\ \frac{\partial c}{\partial \sigma_{xx}} & \frac{\partial c}{\partial \sigma_{yy}} & \frac{\partial c}{\partial \sigma_{xy}} \end{bmatrix} = \begin{bmatrix} \frac{1}{2}(1+c) & \frac{1}{2}(1-c) & s \\ \frac{1}{2}(1-c) & \frac{1}{2}(1+c) & -s \\ \frac{s^2}{\sigma_{11} - \sigma_{22}} & -\frac{s^2}{\sigma_{11} - \sigma_{22}} & -\frac{2sc}{\sigma_{11} - \sigma_{22}} \end{bmatrix}. \tag{3.53}$$

Now the yield function can be defined by:

$$\frac{\partial \Phi}{\partial \boldsymbol{\sigma}} = \left(\frac{\partial \boldsymbol{X}}{\partial \boldsymbol{\sigma}}\right)^{\mathrm{T}} \frac{\partial \Phi}{\partial \boldsymbol{X}}, \tag{3.54}$$

or

$$\begin{Bmatrix} \frac{\partial \Phi}{\partial \sigma_{xx}} \\ \frac{\partial \Phi}{\partial \sigma_{yy}} \\ \frac{\partial \Phi}{\partial \sigma_{xy}} \end{Bmatrix} = \begin{bmatrix} \frac{1}{2}(1+c) & \frac{1}{2}(1-c) & \frac{s^2}{\sigma_{11}-\sigma_{22}} \\ \frac{1}{2}(1-c) & \frac{1}{2}(1+c) & -\frac{s^2}{\sigma_{11}-\sigma_{22}} \\ s & -s & -\frac{2sc}{\sigma_{11}-\sigma_{22}} \end{bmatrix} \begin{Bmatrix} \frac{\partial \Phi}{\partial \sigma_{11}} \\ \frac{\partial \Phi}{\partial \sigma_{22}} \\ \frac{\partial \Phi}{\partial c} \end{Bmatrix}. \tag{3.55}$$

Knowing that the interpolation function $F(\mu, c)$ is given by equation (3.49) it is possible to demonstrate (see ANNEX B.2) that:

$$\begin{Bmatrix} \frac{\partial \Phi}{\partial \sigma_{xx}} \\ \frac{\partial \Phi}{\partial \sigma_{yy}} \\ \frac{\partial \Phi}{\partial \sigma_{xy}} \end{Bmatrix} = \frac{1}{F_1 \frac{\partial F_2}{\partial \mu} - F_2 \frac{\partial F_1}{\partial \mu}} \begin{bmatrix} \frac{1}{2}(1+c) & \frac{1}{2}(1-c) & s^2 \\ \frac{1}{2}(1-c) & \frac{1}{2}(1+c) & -s^2 \\ s & -s & -2sc \end{bmatrix} \begin{Bmatrix} \frac{\partial F_2}{\partial \mu} \\ -\frac{\partial F_1}{\partial \mu} \\ \frac{\bar{\sigma}}{\sigma_{11}-\sigma_{22}} \left(\frac{\partial F_2}{\partial c}\frac{\partial F_1}{\partial \mu} - \frac{\partial F_1}{\partial c}\frac{\partial F_2}{\partial \mu} \right) \end{Bmatrix}. \tag{3.56}$$

A singularity can be observed for $\partial\Phi/\partial\sigma_{xy}$ at the equibiaxial point, since the direction of the principal stresses is undetermined, as highlighted on the third row of equation (3.56). To solve this, the principal components of equation (3.48) are defined as follows:

$$F_i(\mu, c) = (1-\mu)^2 A_i(c) + 2\mu(1-\mu)B_i(c) + \mu^2 C_i(c), \tag{3.57}$$

whose derivatives are:

$$\begin{aligned} \frac{\partial F_i}{\partial \mu} &= 2[-(1-\mu)A_i(c) + (1-2\mu)B_i(c) + \mu C_i(c)], \\ \frac{\partial F_i}{\partial c} &= (1-\mu)^2 \frac{dA_i}{dc} + 2\mu(1-\mu)\frac{dB_i}{dc} + \mu^2 \frac{dC_i}{dc}. \end{aligned} \tag{3.58}$$

This enables to state that:

$$\begin{aligned} &\frac{\partial F_2}{\partial c}\frac{\partial F_1}{\partial \mu} - \frac{\partial F_1}{\partial c}\frac{\partial F_2}{\partial \mu} \\ &\quad = \left[(1-\mu)^2 \frac{dA_2}{dc} + 2\mu(1-\mu)\frac{dB_2}{dc} + \mu^2 \frac{dC_2}{dc} \right] \frac{\partial F_1}{\partial \mu} \\ &\quad - \left[(1-\mu)^2 \frac{dA_1}{dc} + 2\mu(1-\mu)\frac{dB_1}{dc} + \mu^2 \frac{dC_1}{dc} \right] \frac{\partial F_2}{\partial \mu}. \end{aligned} \tag{3.59}$$

Therefore, applying equation (3.49), one can write:

$$\sigma_{11} - \sigma_{22} = \bar{\sigma}[(1-\mu)^2(A_1 - A_2) + 2\mu(1-\mu)(B_1 - B_2) + \mu^2(C_1 - C_2)]. \tag{3.60}$$

Considering that A is the equibiaxial point, then $A_1 = A_2 = F_{\mathrm{bi}}$. This point is independent of γ and so $dA_1/dc = dA_2/dc = 0$. With this, a new equation can be written

$$\frac{\bar{\sigma}}{\sigma_{11}-\sigma_{22}}\left(\frac{\partial F_2}{\partial c}\frac{\partial F_1}{\partial \mu}-\frac{\partial F_1}{\partial c}\frac{\partial F_2}{\partial \mu}\right) = \frac{\left[2\mu(1-\mu)\frac{dB_2}{dc}+\mu^2\frac{dC_2}{dc}\right]\frac{\partial F_1}{\partial \mu}-\left[2\mu(1-\mu)\frac{dB_1}{dc}+\mu^2\frac{dC_1}{dc}\right]\frac{\partial F_2}{\partial \mu}}{2\mu(1-\mu)(B_1-B_2)+\mu^2(C_1-C_2)}. \quad (3.61)$$

Notice that for a number of directions equal to the number of Fourier terms, the Fourier coefficients are obtained by solving a linear system of equations, for the stress values and the strain rate, separately. For instance, if the results are known for 3 directions (n=2), there are 3 Fourier terms related to stresses and other 3 with the strain ratios. The calculation of the hinge point is shown in ANNEX B.2.

Considering as reference Figure 3.2, one can consider that to fully define the yield *locus* one needs to perform 3 uniaxial tensile tests, 3 plane strain tests, two shear tests and an equibiaxial test, leading to a total of 17 parameters (Fourier terms). This experimentally heavy and rather complex formulation is unpractical from an industry standpoint. Further research led to more applicable versions of this model, namely the Vegter lite and the Vegter 2017 versions (Vegter, ten Horn and Abspoel, 2009)(Abspoel *et al.*, 2017). The latter is a new addition to the AutoForm® software, being implemented in the R8 version.

3.4. Vegter 2017

Tata Steel® developed a new approach in an attempt to diminish the experimental burden that the Vegter model brings with its formulation, without losing the accuracy in the description of the material orthotropic behavior (Abspoel *et al.*, 2017). This approach correlates all the experimental results needed as inputs for the original model to the information gathered exclusively from tensile tests. This was done for different classes of materials to assess its validity. The correlation begins with the definition of the equivalent strain using the plastic work principle:

$$Yd\varepsilon_{\mathrm{eq}} = \sigma_{11}d\varepsilon_{11}+\sigma_{22}d\varepsilon_{22}+\sigma_{33}d\varepsilon_{33}. \quad (3.62)$$

For a uniaxial tensile test, this equation reduces to the form:

$$Yd\varepsilon_{\mathrm{eq}} = \sigma_{11}d\varepsilon_{11}. \quad (3.63)$$

For the bulge test, considering incompressibility:

$$Yd\varepsilon_{\mathrm{eq}} = \sigma_{\mathrm{b}} d\varepsilon_{11} + \sigma_{\mathrm{b}} d\varepsilon_{22} = -\sigma_{\mathrm{b}} d\varepsilon_{33} = \sigma_{\mathrm{b}} |d\varepsilon_{33}|. \tag{3.64}$$

Considering isotropic hardening means that the ratio between the first principal stress and the plastic flow stress, F_{un}, as well as the ratio between the biaxial stress and the plastic flow stress, F_{b}, are constant.

$$F_{\mathrm{un}} = \frac{\sigma_{11}}{Y}, F_{\mathrm{b}} = \frac{\sigma_b}{Y}. \tag{3.65}$$

Rewriting:

$$d\varepsilon_{\mathrm{eq}} = F_{\mathrm{un}} d\varepsilon_{11}, d\varepsilon_{\mathrm{eq}} = F_{\mathrm{b}} |d\varepsilon_{33}|. \tag{3.66}$$

Assuming that the yield stress for the uniaxial tensile test along RD is the reference establishes that $F_{\mathrm{un}} = 1$. This means that for the uniaxial tensile test, the equivalent strain is equal to the axial strain, as expected. For the bulge test, by integration:

$$\varepsilon_{\mathrm{eq}} = F_{\mathrm{b}} |\varepsilon_{33}|. \tag{3.67}$$

The procedure compares the equivalent plastic work of the reference uniaxial test in the RD with the other different loading tests, as follows:

$$\sigma_{\mathrm{test}} \varepsilon_{\mathrm{test}} = \sigma_{\mathrm{ref}} \varepsilon_{\mathrm{ref}}. \tag{3.68}$$

The uniaxial stress factors, F_{un_0}, $F_{\mathrm{un}_{45}}$ and $F_{\mathrm{un}_{90}}$should be determined using as reference the mechanical properties obtained in the uniaxial tensile test. Abspoel *et al.* (2017) noted that the yield strength is not a good choice for an input parameter to the model. This comes from the fact that some materials exhibit the Yield Point Elongation phenomenon, where at low strain values the stress-strain curve is unstable. Therefore, the authors suggest to calculate the uniaxial stress factors based on the tensile strength, R_{m}, and the uniform elongation, A_{g}, instead. These parameters were chosen based on experiments that registered a variation of more or less 1% for the uniaxial factors, with various materials evaluated. However, since the R_{m} and A_{g} points do not coincide at equal plastic work for the different directions, a correction must be done. Rewriting the equivalent plastic work expression:

$$\varepsilon_{\mathrm{ref}} = \frac{\sigma_{\mathrm{un},\theta} \varepsilon_{\mathrm{un},\theta}}{\sigma_{\mathrm{ref}}} = F_{\mathrm{un},\theta} \varepsilon_{\mathrm{un},\theta}. \tag{3.69}$$

Once again, noting that the reference is the uniaxial tensile test in the RD, at equal plastic work:

$$F_{\mathrm{un},\theta} = \frac{\varepsilon_{\mathrm{ref}}}{\varepsilon_{\mathrm{un},\theta}} = \frac{\varepsilon_{\mathrm{un},0}}{\varepsilon_{\mathrm{epw},\theta}}. \tag{3.70}$$

where the subscript epw corresponds to equal plastic work.

To find an equivalent point for each orientation θ, Nadai's (or Ludwick's) hardening law is used.

$$\sigma_{\mathrm{un},\theta} = C_{\mathrm{un},\theta}\left(\varepsilon_{\mathrm{un},\theta}\right)^{n_{\mathrm{un},\theta}}. \tag{3.71}$$

Considère's criterion states that at the necking point $\sigma = (d\sigma/d\varepsilon)$, meaning that:

$$\begin{aligned} n_{\mathrm{un},\theta} &= \varepsilon_{A_{\mathrm{g},\theta}} = \ln\left(1 + \frac{A_{\mathrm{g},\theta}}{100}\right), \\ \sigma_{\mathrm{un},\theta} &= \sigma_{A_{\mathrm{g},\theta}} = R_{\mathrm{m},\theta}\left(1 + \frac{A_{\mathrm{g},\theta}}{100}\right). \end{aligned} \tag{3.72}$$

The plastic work is obtained by:

$$W_\theta = \int_0^{\varepsilon} \sigma_{\mathrm{un},\theta}\, d\varepsilon = \frac{C_{\mathrm{un},\theta}}{n_{\mathrm{un},\theta} + 1}\left(\varepsilon_{\mathrm{un},\theta}\right)^{n_{\mathrm{un},\theta}+1}. \tag{3.73}$$

This allows determining that at the onset of necking, for the RD:

$$W_0 = \frac{C_{A_{\mathrm{g},0}}}{\varepsilon_{A_{\mathrm{g},0}} + 1}\left(\varepsilon_{A_{\mathrm{g},0}}\right)^{\varepsilon_{A_{\mathrm{g},0}}+1}. \tag{3.74}$$

Since the same work must be achieved for the other directions, the strain at equal plastic work is defined as:

$$\varepsilon_{\mathrm{epw},\theta} = \left[\left(\varepsilon_{A_{\mathrm{g},\theta}} + 1\right)\frac{W_0}{C_{A_{\mathrm{g},\theta}}}\right]^{\left(\frac{1}{\varepsilon_{A_{\mathrm{g},\theta}}+1}\right)}. \tag{3.75}$$

The uniaxial factors can now be obtained using equation (3.70). To determine the remaining stress factors, namely for the biaxial, plane strain and shear points, the anisotropy coefficients and the uniaxial factors are used.

Starting with the biaxial point, the authors observed that its value rises with the increase of the r-values (for all directions) and the uniaxial stress factors. Qualitatively, this corresponds to the behavior predicted by the Hill'48 yield criterion. To further analyze the correlations, the authors introduce the average of the uniaxial stress factors:

$$F_{\mathrm{un,av}} = \frac{F_{\mathrm{un},0} + 2F_{\mathrm{un},45} + F_{\mathrm{un},90}}{4}. \tag{3.76}$$

The authors analyzed the change of the normalized biaxial factor $F_{\mathrm{bi}}/F_{\mathrm{un,av}}$ depending on r_{m}, for different strain percentages. The results collected are shown in Figure 3.3. Note that higher values of r_{m} tend to increase the dispersion of the results. Inversely, lower values of r_{m} show practically no change in the biaxial factor. An average of the evolution was chosen

to represent the trend. The biaxial factor at 5% strain was selected and validated using FE simulation. This level of strain avoids the initial transitory effects of the stress factor for some materials.

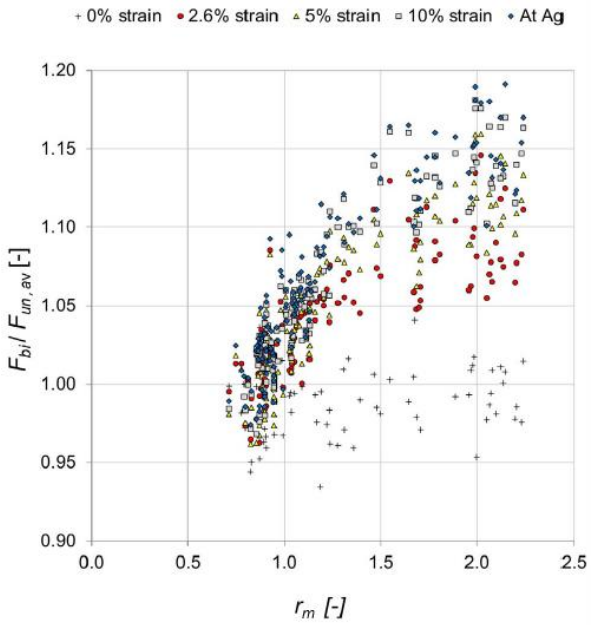

Figure 3.3. Normalized biaxial factor depending on the average *r*-value for different levels of strain (Abspoel *et al.*, 2017).

A Dirac function is used to fit the measured points:

$$F_{\mathrm{bi}} = F_{\mathrm{un,av}}\left(\frac{F_{\mathrm{bi,min}}}{1+f_{\mathrm{Dirac}}}+\frac{F_{\mathrm{bi,max}}}{1+\frac{1}{f_{\mathrm{Dirac}}}}\right), \tag{3.77}$$

$$f_{\mathrm{Dirac}} = e^{[a_{\mathrm{Dirac}}(r_{\mathrm{m}}-F_{\mathrm{b,trans}})]},$$

with $F_{\mathrm{bi,min}} = 0.97$, $F_{\mathrm{bi,max}} = 1.14$, $F_{\mathrm{bi,trans}} = 1.22$ and $a_{\mathrm{Dirac}} = 3.4$. The anisotropy coefficient for the biaxial point is considered equal to the one defined by the Hill'48 criterion. The experiments done reveal that for most materials this is valid. In a scenario where $(r_0/r_{90}) > 1$ it is recommended to measure this parameter experimentally.

The plane strain point rises with the increase of the r-value and the uniaxial stress factor, both for the respective test direction. A similar approach to the one adopted for the biaxial point is followed, where the first stress component of the plane strain factor is taken at 5% strain. The Dirac function in this case is:

$$F_{\mathrm{ps},\theta} = F_{\mathrm{un},\theta}\left(\frac{F_{\mathrm{ps,min}}}{1+f_{\mathrm{Dirac}}} + \frac{F_{\mathrm{ps,max}}}{1+\frac{1}{f_{\mathrm{Dirac}}}}\right), \qquad (3.78)$$

$$f_{\mathrm{Dirac}} = e^{\left[a_{\mathrm{Dirac}}\left(r_\theta - F_{\mathrm{ps,trans}}\right)\right]},$$

with $F_{\mathrm{ps,min}} = 0.827$, $F_{\mathrm{ps,max}} = 1.315$, $F_{\mathrm{ps,trans}} = 0.5$ and $a_{\mathrm{Dirac}} = 1.2$.

The shear point rises with the increase of the uniaxial stress factor for the 90º direction. Although it is influenced by the uniaxial factor for the RD, this always has the value of one, as stated earlier in the text. The authors make a distinction between the 0º-90º and 45º-135º stress spaces. For the former, the following averages are considered:

$$F_{\mathrm{un,av}_{0-90}} = \frac{F_{\mathrm{un},0} + F_{\mathrm{un},90}}{2}, \qquad (3.79)$$

$$r_{\mathrm{m}_{0-90}} = \frac{r_0 + r_{90}}{2}.$$

The Dirac function becomes:

$$F_{\mathrm{sh},0} = F_{\mathrm{sh},90} = F_{\mathrm{un,av}_{0-90}}\left(\frac{F_{\mathrm{sh,min}}}{1+f_{\mathrm{Dirac}}} + \frac{F_{\mathrm{sh,max}}}{1+\frac{1}{f_{\mathrm{Dirac}}}}\right), \qquad (3.80)$$

$$f_{\mathrm{Dirac}} = e^{\left[a_{\mathrm{Dirac}}\left(r_{\mathrm{m}_{0-90}} - F_{\mathrm{sh,trans}}\right)\right]}.$$

For the latter, symmetry in that plane enables to consider that $F_{\mathrm{un,av}_{45-135}} = F_{\mathrm{un},45}$ and $r_{\mathrm{m}_{45-135}} = r_{45}$. Therefore, the stress factor is defined:

$$F_{\mathrm{sh},45} = F_{\mathrm{un,av}_{45-135}}\left(\frac{F_{\mathrm{sh,min}}}{1+f_{\mathrm{Dirac}}} + \frac{F_{\mathrm{sh,max}}}{1+\frac{1}{f_{\mathrm{Dirac}}}}\right), \qquad (3.81)$$

$$f_{\mathrm{Dirac}} = e^{\left[a_{\mathrm{Dirac}}\left(r_{\mathrm{m}_{45-135}} - F_{\mathrm{sh,trans}}\right)\right]}.$$

For both cases, $F_{\mathrm{sh,min}} = 0.757$, $F_{\mathrm{sh,max}} = 0.525$, $F_{\mathrm{sh,trans}} = 0$ and $a_{\mathrm{Dirac}} = 1.6$.

The final point to be determined is the second stress component of the plane strain condition. In this case, the Vegter lite yield criterion is used, since regular experimental tests cannot determine this point. The difference between the original criterion and the lite version is that a weight factor w is introduced. This was an initial attempt to reduce the number of experiments needed to define the yield criterion, where the shear and plane strain points are not considered in the Bézier interpolation and an approximation is made instead. The Vegter lite equation for plane strain is:

$$\begin{bmatrix} F_{\mathrm{ps1},\theta} \\ F_{\mathrm{ps2},\theta} \end{bmatrix} = \frac{(1-\mu)^2 \begin{bmatrix} F_{\mathrm{un1},\theta} \\ F_{\mathrm{un2},\theta} \end{bmatrix} + 2\mu w(1-\mu) \begin{bmatrix} F^{\mathrm{VL}}_{\mathrm{h1},\theta} \\ F^{\mathrm{VL}}_{\mathrm{h2},\theta} \end{bmatrix} + \mu^2 \begin{bmatrix} F_{\mathrm{bi1}} \\ F_{\mathrm{bi2}} \end{bmatrix}}{(1-\mu)^2 + 2\mu w(1-\mu) + \mu^2}, \tag{3.82}$$

where similarities with the original can be seen by recalling equation (3.48). The first and second principal stress components of the Vegter lite hinge points are given by:

$$\begin{aligned} F^{\mathrm{VL}}_{\mathrm{h2},\theta} &= \frac{F_{\mathrm{bi1}} + \rho_{\mathrm{bi},\theta} F_{\mathrm{bi2}} - F_{\mathrm{un1},\theta} - \rho_{\mathrm{un},\theta} F_{\mathrm{un2},\theta}}{\rho_{\mathrm{bi},\theta} - \rho_{\mathrm{un},\theta}}, \\ F^{\mathrm{VL}}_{\mathrm{h1},\theta} &= F_{\mathrm{bi1}} - \rho_{\mathrm{bi},\theta}\left(F^{\mathrm{VL}}_{\mathrm{h2},\theta} - F_{\mathrm{bi2}}\right), \end{aligned} \tag{3.83}$$

with $\rho_{\mathrm{un},\theta} = -[r_\theta/(1+r_\theta)]$, $\rho_{\mathrm{bi},0} = (r_0/r_{90})$, $\rho_{\mathrm{bi},45} = 1$ and $\rho_{\mathrm{bi},90} = (r_{90}/r_0)$. Taking into account the associated flow rule and the equations (B.12) and (B.13), the next definition can be written:

$$\rho_{\mathrm{ps}} = \frac{d\varepsilon_{22}}{d\varepsilon_{11}} = \frac{\dfrac{\partial \Phi}{\partial \sigma_{22}}}{\dfrac{\partial \Phi}{\partial \sigma_{11}}} = \frac{-\dfrac{\partial F_1}{\partial \mu}}{\dfrac{\partial F_2}{\partial \mu}}. \tag{3.84}$$

To find the appropriate μ and w to define the second stress component of the plane strain point, recall that the corresponding strain rate is zero. This means that the denominator of the previous equation must be zero also. After differentiating:

$$\begin{aligned} \mu^2\left[(w-1)\left(F_{\mathrm{bi1}} - F_{\mathrm{un1},\theta}\right)\right] + \mu\left[F_{\mathrm{bi1}} - F_{\mathrm{un1},\theta} - 2w\left(F^{\mathrm{VL}}_{\mathrm{h1},\theta} - F_{\mathrm{un1},\theta}\right)\right] \\ + w\left(F^{\mathrm{VL}}_{\mathrm{h1},\theta} - F_{\mathrm{un1},\theta}\right) = 0. \end{aligned} \tag{3.85}$$

This equation corresponds to a second order polynomial where $a = \left[(w-1)\left(F_{\mathrm{bi1}} - F_{\mathrm{un1},\theta}\right)\right]$, $b = \left[F_{\mathrm{bi1}} - F_{\mathrm{un1},\theta} - 2w\left(F^{\mathrm{VL}}_{\mathrm{h1},\theta} - F_{\mathrm{un1},\theta}\right)\right]$ and $c = w\left(F^{\mathrm{VL}}_{\mathrm{h1},\theta} - F_{\mathrm{un1},\theta}\right)$. μ can be easily obtained with the quadratic formula. Then, the weight factor can be determined from equation (3.82):

$$w = \frac{(1-\mu)^2\left(F_{\mathrm{un1},\theta} - F_{\mathrm{ps1},\theta}\right) + \mu^2\left(F_{\mathrm{bi1}} - F_{\mathrm{ps1},\theta}\right)}{2\mu(1-\mu)\left(F_{\mathrm{ps1},\theta} - F^{\mathrm{VL}}_{\mathrm{h1},\theta}\right)}. \tag{3.86}$$

with $w > 0$. An iterative process is done to determine μ and w, to assure that $F_{\mathrm{ps1},\theta}$ and $F_{\mathrm{ps2},\theta}$ obey to equation (3.78). The Bézier curves located between the second components of the uniaxial and plane strain points, as well as between plane strain and the biaxial point, need to be defined. The factor $\alpha_{ps,\theta}$ is introduced in the formulation:

$$\alpha_{\mathrm{ps},\theta} = \frac{F_{\mathrm{ps2},\theta} - F_{\mathrm{h2},\theta\_\mathrm{unps}}}{F_{\mathrm{h2},\theta\_\mathrm{bips}} - F_{\mathrm{h2},\theta\_\mathrm{unps}}}. \tag{3.87}$$

The two new hinge points can be calculated with:

$$F_{\mathrm{h2},\theta\_\mathrm{unps}} = \frac{F_{\mathrm{ps1},\theta} + \rho_{\mathrm{ps},\theta} F_{\mathrm{ps2},\theta} - F_{\mathrm{un1},\theta} - \rho_{\mathrm{un},\theta} F_{\mathrm{un2},\theta}}{\rho_{\mathrm{ps},\theta} - \rho_{\mathrm{un},\theta}},$$
$$F_{\mathrm{h2},\theta\_\mathrm{bips}} = \frac{F_{\mathrm{bi1}} + \rho_{\mathrm{bi}} F_{\mathrm{bi2}} - F_{\mathrm{ps1},\theta} - \rho_{\mathrm{ps},\theta} F_{\mathrm{ps2},\theta}}{\rho_{\mathrm{bi}} - \rho_{\mathrm{ps},\theta}}, \tag{3.88}$$

where, in this case, $\rho_{\mathrm{ps},\theta} = 0$. Figure 3.4 illustrates all these stress factors and the corresponding hinge points. Having all the factors determined, all that is left is to apply the original Vegter formulation to obtain the yield curve.

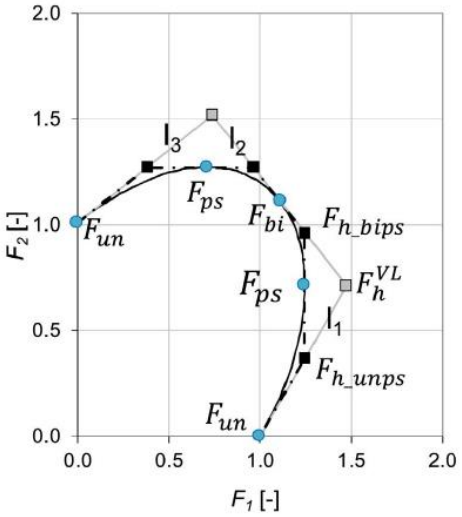

Figure 3.4. Representation of the stress factors, F, and hinge points, F_h, for the Vegter and Vegter lite models (Abspoel *et al.*, 2017).

3.4.1. Convexity check

One detail that cannot be overlooked with the Vegter models is the convexity check. For some highly anisotropic materials, the yield locus might become non-convex, since it is purely interpolated with stress values and strain ratios. Tata Steel® developed an algorithm for this purpose, considering the curvature of the 3D surface generated by the three planar stress components, σ_{xx}, σ_{yy} and σ_{xy}. This surface is discretized into several cross-sections, either parallel or nearly perpendicular to the equibiaxial line. The curvature is calculated for each cross-section. A warning will appear if convexity is not met and it is advised to change the input parameters.

3.5. Summary

Table 3.1 shows all the criteria present in AutoForm® R8 and the corresponding input values required. Note that Vegter (Full) is the original formulation, as described in section 3.3. At the moment, it can only be used with information provided in an ASCII material file, unlike the 2017 version. Barlat 1989 yield criterion was not used in this work, although it is one possible option. It is typically used to study aluminum alloys and its main advantage over Hill'48 is the varying exponent, which BBC 2005 also provides. In the software, the exponent appears as M for all the criteria that possess it. In the case of BBC 2005, it is equivalent to $2k$ and for Hill'48 it is equal to 2. The software also gives the option to use BBC 2005 with the biaxial information of either Hill'48 or Barlat'89, which is represented by the arrows in the table.

Table 3.1. Inputs needed for the yield criterion used in AutoForm® (*AutoForm® R8 software manual*, 2018).

Test	Uniaxial Tensile Test												Biaxial		Shear			Plane Strain		
Value	σ_0	σ_{45}	σ_{90}	r_0	r_{45}	r_{90}	$A_{g,0}$	$A_{g,45}$	$A_{g,90}$	$R_{m,0}$	$R_{m,45}$	$R_{m,90}$	σ_b	r_b	τ_0	τ_{45}	τ_{90}	$\sigma_{ps,0}$	$\sigma_{ps,45}$	$\sigma_{ps,90}$
Vegter 2017																				
Vegter (Full)																				
BBC 2005 (8)																				
BBC 2005 (7)																				
BBC 2005 (6)																				
Barlat 89																				
Hill 48																				

4. NON-LINEAR STRAIN PATHS

As stated previously, the FLC alone is not enough to characterize the formability of materials subjected to non-linear strain paths. A phenomenological approach to study multi-step forming operations using the FLC concept was proposed by Volk *et al.*, (2012) and was implemented in AutoForm®. The concept is explained in the following section.

4.1. Time Dependent Evaluation Method

Volk and Hora (2011) start by discussing the importance of accurately evaluating experimentally the beginning of the strain instability, to ensure a proper definition of the FLC. Later named Time Dependent Evaluation Method (TDEM), its premise is the notion that the remaining plastic strain localizes in small bands or regions, leading to high thinning rates. Their studies remark that the thinning rate is a suitable physical quantity to identify the beginning of the instability.

The TDEM is divided into several steps, starting with the creation of a grid in the specimen whose cross points serve as references for a global coordinate system. These can be treated as the global coordinates of a finite element mesh and studied accordingly. The experimental test should then be recorded with sufficient pictures per unit time, with focus on the elements located at the instability zone. For every picture k, i elements are selected, each with its respective thinning rate, $\dot{\varepsilon}_i^k$. By sorting them, from the smallest to biggest, Γ^k is obtained, such as:

$$\Gamma^k = \{\dot{\varepsilon}_1^k, \dot{\varepsilon}_2^k, \dots, \dot{\varepsilon}_n^k\}, \text{ with } \dot{\varepsilon}_{i-1}^k \leq \dot{\varepsilon}_i^k \text{ for } i = 2, \dots, g \text{ and } k = 1, \dots, b, \tag{4.1}$$

where g is the total number of elements and b the total number of pictures. To determine the thinning rate, or the strain rate in the thickness direction, the deformation gradient **F** and its derivative are needed. Defining **u** as the displacement vector and **X** as the reference position vector (initial coordinates), **F** and its time derivative $\dot{\mathbf{F}}$ can be defined, in index notation, as follows:

$$F_{ij} = I_{ij} + \frac{\partial u_i}{\partial X_j}. \tag{4.2}$$

$$\dot{F}_{ij} = \frac{\partial F_{ij}}{\partial t}. \tag{4.3}$$

The velocity gradient tensor **L** can be obtained from equations (4.2) and (4.3) as follows:

$$L_{ij} = \dot{F}_{ij} {F_{ij}}^{-1}. \tag{4.4}$$

The deformation rate tensor **D** is defined as:

$$D_{ij} = \frac{1}{2}\left(L_{ij} + {L_{ij}}^{\mathrm{T}}\right). \tag{4.5}$$

This tensor is deviatoric, which means that its in-plane eigenvalues D_1 and D_2, allow to determine the thinning rate as follows:

$$\dot{\varepsilon} = |D_3| = -(D_1 + D_2). \tag{4.6}$$

The maximum thinning rate $\dot{\bar{\varepsilon}}_{\max}$ is defined by the arithmetic mean value of the five highest thinning rates in the second last picture:

$$\dot{\bar{\varepsilon}}_{\max} = \frac{1}{5}\sum_{i=g-4}^{g} \dot{\varepsilon}_i^{b-1}. \tag{4.7}$$

The following step requires the definition of the thinning rate limit, $\alpha\dot{\bar{\varepsilon}}_{\max}$, which corresponds to the value after which it is assumed that an element achieves necking. This allows defining the set N, constituted by all the elements that surpass $\alpha\dot{\bar{\varepsilon}}_{\max}$, and N^k by the thinning rates present in N, for every picture k:

$$N = \forall\, Element\ with\ \dot{\varepsilon}_i^{b-1} \geq \alpha\dot{\bar{\varepsilon}}_{\max}, \text{ and} \tag{4.8}$$

$$N^k = \{{}^N\dot{\varepsilon}_1^k, {}^N\dot{\varepsilon}_2^k, \dots, {}^N\dot{\varepsilon}_n^k\}. \tag{4.9}$$

The factor α is chosen so that the set N^k has the desired proportion of number of elements per grid size. Finally, this enables to calculate $\dot{\bar{\varepsilon}}_{\mathrm{rep}}^k$ as the arithmetic mean value of all elements (n) present in each set N^k, such as:

$$\dot{\bar{\varepsilon}}_{\mathrm{rep}}^k = \frac{1}{n}\sum_{i=1}^{n} {}^N\dot{\varepsilon}_i^k. \tag{4.10}$$

Figure 4.1 represents the characteristic diagram obtained by plotting the representative thinning rate $\dot{\bar{\varepsilon}}_{\mathrm{rep}}^k$ for every picture. Two different trends can be observed. One is the stable and nearly homogeneous beginning of deformation. The other is the unstable deformation until fracture occurs, originated by the necking. The beginning of the instability is

determined by fitting linear trend lines, using the least square method, to each trend. It will correspond to the closest value relative to the cross point of the two regression lines (marked in green in Figure 4.1). Then, the limit in-plane strains are calculated as the mean value of the points in the localized area.

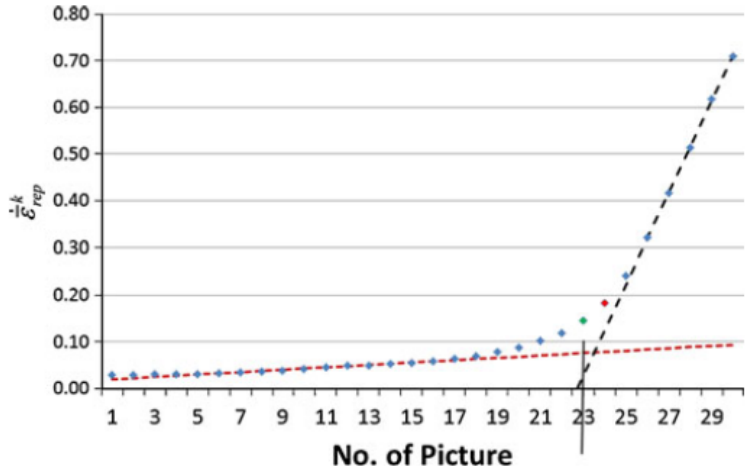

Figure 4.1. Detection of the beginning of the strain instability based of the linear curve fitting using the least square method (Volk and Hora, 2011).

4.2. Generalized Forming Limit Concept

In order to systematize the influence of strain path changes on the FLC, Volk *et al.*, (2012) performed an extensive experimental study focused on bi-linear strain paths. Figure 4.2 shows the results corresponding to the formability evaluation using the TDEM for a dual phase steel, HC300X, with a thickness of 1 mm. The pre-strain is performed using either oversized tensile test specimens (points 1 and 2) or oversized Marciniak test specimens (points 3 to 6). These oversized specimens enable the post forming with standard Nakajima tests, following four post-strain directions. The results are shown in the curves identified with the same numbers. Each post-strain point shown corresponds to the analysis of three samples, for a total of 72 experiments. The monotonic FLC is also plotted for reference. It should be noted that for some loading sequences the formability of the material increases, as is the case of uniaxial pre-strain followed by biaxial post-strain. However, the opposite can also be observed, for instance for biaxial pre-strain followed by plane strain.

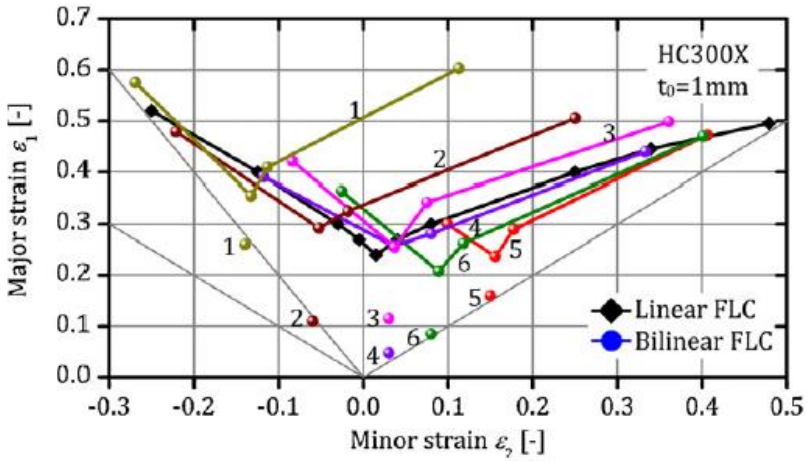

Figure 4.2. Experimental forming limit diagram for bilinear strain paths using time dependent evaluation method for six different pre-strains (Volk *et al.*, 2012).

Every strain path can be defined by its strain ratio β:

$$\beta = \varepsilon_2/\varepsilon_1, \tag{4.11}$$

where ε_1 and ε_2 are the major and minor in-plane strains, respectively. If a straight line is drawn from the origin until it intersects the linear FLC and is measured, the total strain path length l_{FLC} can be obtained. Similarly, any random point in that line creates a linear strain path length l with the origin. This means that, for a fixed β value, there is a unique strain path length $l(\beta)$ given by:

$$l(\beta) = \sqrt{(1+\beta^2)\varepsilon_1^2}. \tag{4.12}$$

Therefore, this strain path length can be compared with the corresponding total strain path length $l_{\mathrm{FLC}}(\beta)$. This is done by introducing the strain path length ratio $\lambda(\beta)$ as follows:

$$\lambda(\beta) = l(\beta)/l_{\mathrm{FLC}}(\beta). \tag{4.13}$$

When considering bi-linear strain paths, Volk *et al.*, (2012) suggest that the pre and post forming strain path length ratios, λ_{pre} and λ_{post} respectively, can also be calculated separately for each specific bilinear strain history. According to the authors, this enables a way to analyze the forming limit for bilinear strain paths. In this context, the total strain path length ratio λ is introduced to serve as a predictor for the beginning of the instability, as follows:

$$\lambda = \lambda_{\mathrm{pre}} + \lambda_{\mathrm{post}} = \frac{l(\beta_{\mathrm{pre}})}{l_{\mathrm{FLC}}(\beta_{\mathrm{pre}})} + \frac{l(\beta_{\mathrm{post}})}{l_{\mathrm{FLC}}(\beta_{\mathrm{post}})} \tag{4.14}$$

This enables to parameterize the forming limit strain as a function of the strain ratio and the strain path length. However, it should be noted that in order to evaluate the post forming strain path length $l(\beta_{\text{post}})$, it is necessary to know the post-forming FLC for that specific bilinear path. Only then can the post forming strain path length be determined and compared to the total strain path length of the linear FLC for the same post-strain ratio, $l_{\text{FLC}}(\beta_{\text{post}})$. Figure 4.3 shows the interpolation of four post-strains of the previously mentioned experiments, forming a non-linear FLC. These points were initially plotted together with the linear FLC for reference. The pre-strain was performed considering a biaxial strain path ($\beta = 1.0$), leading to point 5, with a total strain path length indicated in blue. The post-strain was performed close to uniaxial tensile conditions for point 51 ($\beta \approx -0.5$), close to plane strain for points 52 and 53 ($\beta \approx 0.0$) and close to biaxial strain for point 54 ($\beta \approx 1.0$). Note that these post-strain points are plotted at the beginning of the strain instability, as determined using the TDEM. The diagram on the right represents the value of total strain path length ratio in respect to necking, for each of the bilinear strain paths. It clearly shows that, for points 51, 52 and 53, when $\beta_{\text{pre}} \neq \beta_{\text{post}}$, the total strain path length ratio is inferior to 1. This is to be expected considering that a biaxial expansion followed by any different monotonic loading typically leads to a loss in formability. This loss is translated into a decrease of the total strain path length ratio. It should be clear that considering the non-linear FLC as the post forming reference would lead to the post forming strain path length ratio to be equal to 1.0 for all points and, consequentially, for the total strain path length ratio to be higher than 1.0 for every path where $\beta_{\text{pre}} \neq \beta_{\text{post}}$. Therefore, the total strain path length ratio would lose its meaning, highlighting the importance of using the linear FLC as the reference for both total pre- and post-strain path length. Logically, since the post-strain is performed until necking occurrence, if there was no change between β_{pre} and β_{post} then $\lambda = 1.0$ and the linear FLC would be reached for the four strain paths. Therefore, Volk and Suh (2014) recognized that the total strain path length ratio can be seen as a measure of exhausted formability.

Figure 4.4 expresses the parameterization focusing only on point 51, in order to better explain the procedure. The biaxial pre-forming ($\beta_{\text{pre}} = 0.97$) was performed until $\varepsilon_1 = 0.180$ and $\varepsilon_2 = 0.167$. The uniaxial post-forming ($\beta_{\text{pre}} = -0.36$) corresponds to $\varepsilon_1 = 0.120$ and $\varepsilon_2 = -0.040$. Note that to evaluate λ_{post} it is necessary to reposition the strain

path on the origin to establish the linear FLC as the reference. Furthermore, the necking point after post-forming happens to nearly coincide with the linear FLC, but for a value of $\lambda = 0.63$, substantially inferior to 1.0.

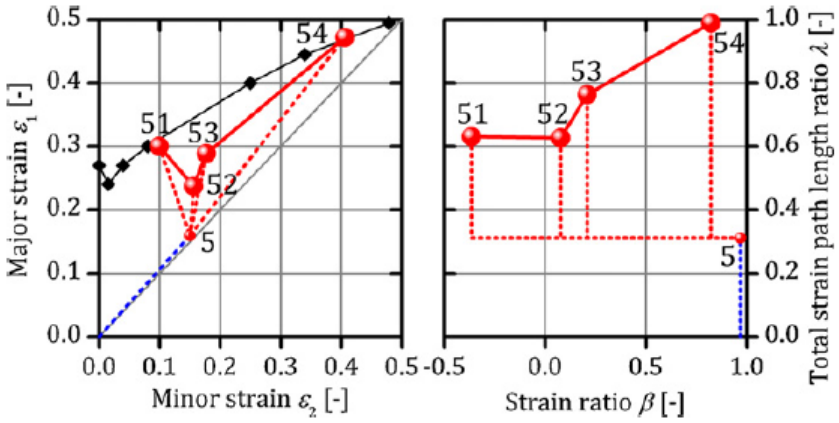

Figure 4.3. Parameterization of the four experimentally evaluated necking points, for a pre-strain under biaxial loading conditions (point 5) and linear interpolation between the necking points, in the plane defined by the strain ratio and the total strain path length ratio (Volk *et al.*, 2012).

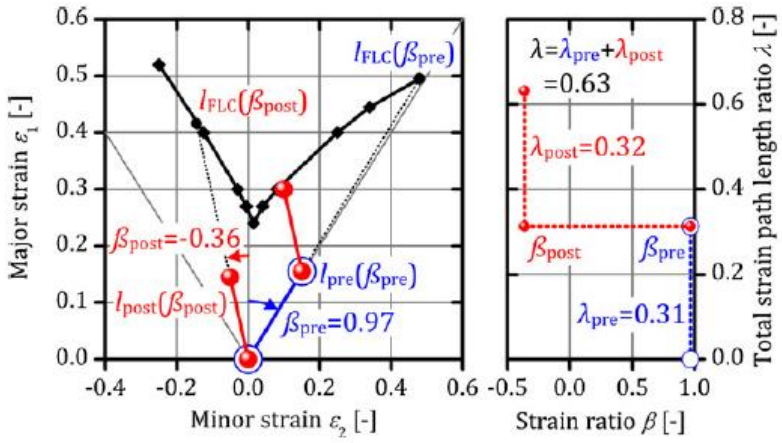

Figure 4.4. Parameterization of the bilinear strain path with biaxial pre-forming and uniaxial post-forming (Volk *et al.*, 2012).

Volk *et al.*, (2012) suggest the use of the space defined by the pre-strain ratio (β_{pre}) and the pre-strain path length ratio (λ_{pre}) to build a metamodel that enables the estimate of the post-strain path length for any strain ratio. They suggest to mark specific points in this space such that it is possible to divide it in four-node elements. Figure 4.5 shows an example of this procedure, such that points 1 to 6 are equivalent to the ones in Figure 4.2, i.e. they correspond to points on the safe side of the FLC. Points 7 to 9 present

$\lambda_{\mathrm{pre}} = 0$, which means that no deformation has occurred and, consequently, they are free to post-form until reaching the limit of the linear FLC. Points 10 to 12 come directly from the FLC and show $\lambda_{\mathrm{post}} = 0$, i.e. there is no formability left for post-strain. The definition of these points enables the construction of a mesh of 12 base points (or nodes) that form several domains (8 finite elements). The authors proposed the use of four-node Lagrange elements, meaning that an isoparametric approximation is adopted to define the pre-strain ratio (β_{pre}) and the pre-strain path length ratio (λ_{pre}), for any strain path, as follows:

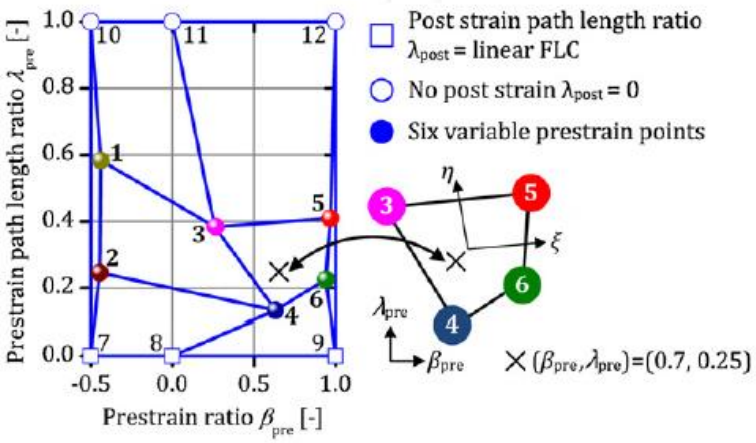

Figure 4.5. Metamodel to enable the estimate of the post-strain path length for any strain ratio, based on the linear interpolation (four-node Lagrange element) of reference points (altered) (Volk *et al.*, 2012).

$$\beta_{\mathrm{pre}} = \sum_{i=1}^{4} \beta_i \psi_i(\xi, \eta) \tag{4.15}$$

$$\lambda_{\mathrm{pre}} = \sum_{i=1}^{4} \lambda_i \psi_i(\xi, \eta) \tag{4.16}$$

where ψ_i represents the isoparametric shape functions and ξ and η the natural coordinates. Figure 4.5 shows the example of the location of a new point presenting $\beta_{\mathrm{pre}} = 0.70$ and $\lambda_{\mathrm{pre}} = 0.25$. Moreover, for each one of the 12 base points, the metamodel also stores the experimental values available for β_{post} and λ_{post} (non-linear post-forming FLC), as schematically shown in Figure 4.6, for the point selected in Figure 4.5. This enables to predict the post-strain length ratio for whichever pre-strain state desired or, in other words, for arbitrary β_{pre}, λ_{pre} and β_{post}. The estimation is based on the necking points for the corresponding domain, with a scalar product approximation between the calculated path

length ratio and the interpolation functions. This is also schematically represented in Figure 4.6, assuming that $\beta_{\text{post}} = -0.3$ for the point in analysis. Note that, since for each pre-strain point the non-linear post-forming FLC is stored, the strain state can also be calculated inversely, i.e. by using equations (4.11) and (4.12) after relocating the point to its equivalent position in the linear FLC.

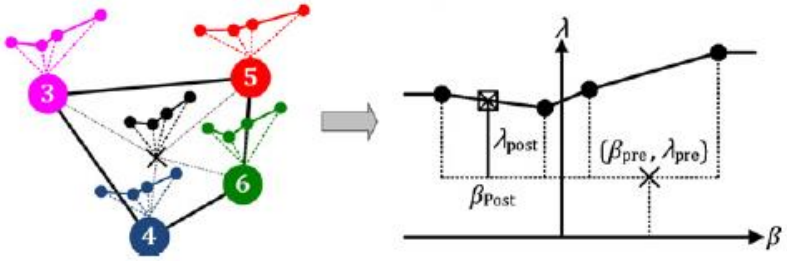

Figure 4.6. Prediction using isoparametric approximation of the post forming strain path length ratio (Volk *et al.*, 2012).

It should be mentioned that the total strain path length ratios can be stored in a database for software implementation (Jocham *et al.*, 2015), in order to avoid its evaluation during the numerical simulation. A good way to look at this is by constructing the response surfaces of the total strain path length ratio as function of β_{pre} and β_{post} for a specific λ_{pre}, as shown in Figure 4.7.

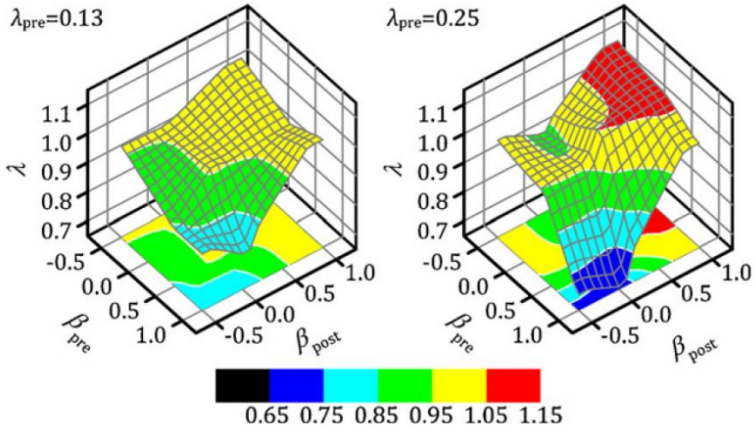

Figure 4.7. Response surfaces of total strain path length ratio for different pre-forming strain path length ratio (Volk *et al.*, 2012).

With the logic exposed for bi-linear strain paths, Volk and Suh (2014) proposed a phenomenological approach which became the basis for evaluating non-linear strain paths

in AutoForm®, i.e. the Generalized Forming Limit Concept (GFLC). It extends the approach from bilinear strain-paths to arbitrary non-linear ones, consisting of an unlimited number of individual strain increments. This is possible since the established metamodel takes a given pre-strain state and predicts the remaining formability. But it can also be used the other way around. Given a post-strain it can calculate the equivalent pre-strain for each direction. In other words, it searches for the pre-strain states that have the same exhausted formability (λ_{post}). This is defined by the authors has the principle of equivalent pre-forming, as shown in Figure 4.8, for $\lambda_{\text{post}} = 0.5$ and three different post-forming directions. One important thing to note is that the points that have equivalent pre forming do not necessarily have the same equivalent plastic strain. This is the reason why the equivalent plastic strain is not a good measure for determining non-linear strain paths.

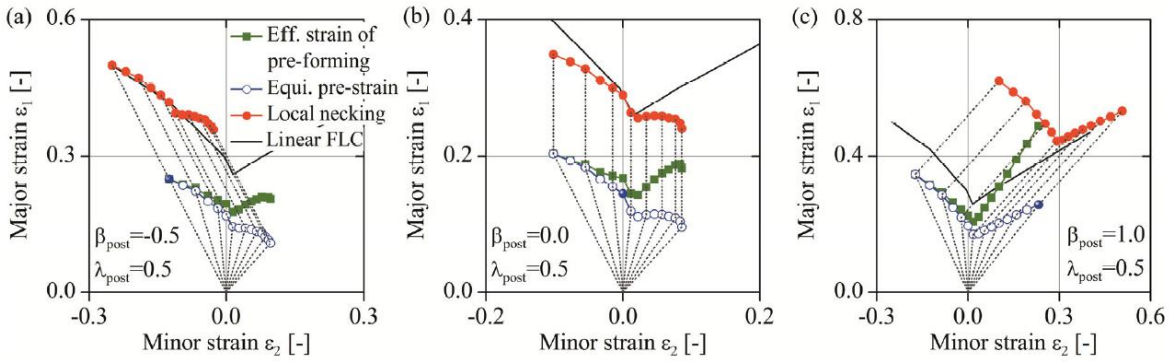

Figure 4.8. Distribution of equivalent pre-strains of HC300X with the same exhausted formability for three post forming directions: (a) uniaxial, (b) plane strain and (c) biaxial direction (Volk and Suh, 2014).

To expand the concept to multilinear strain paths a new parameter is introduced, the corrected strain path length ratio:

$$\lambda_{\text{cor}} = \lambda_{\text{pre}} + \left[1 - \left(\lambda_{\text{pre}} + \lambda_{\text{post}}\right)\right] = 1 - \lambda_{\text{post}}. \tag{4.17}$$

This parameter enables the transformation of a bilinear strain path into a linear equivalent with the same remaining formability. In other words, it serves as the correction of the pre-strain path length ratio λ_{pre}, of a previous strain ratio β_{pre}, to an equivalent one with the current strain ratio β_{post}, hence the name.

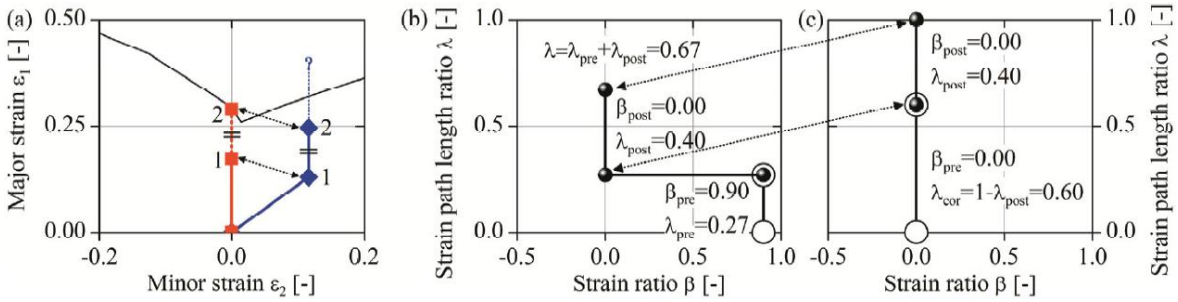

Figure 4.9. Application of the principle of equivalent pre-forming and modified parameterization with the fixed λ=1: (a) equivalent pre and post-strain in plane strain direction, (b) parameterization of the bilinear deformation history, (c) its linearization with corrected strain path length ratio λ_{cor} (Volk and Suh, 2014).

Figure 4.9 (a) shows a non-linear strain path in blue that presents $\beta_{\mathrm{pre}} = 0.97$; $\lambda_{\mathrm{pre}} = 0.27$ and $\beta_{\mathrm{post}} = 0.0$; $\lambda_{\mathrm{post}} = 0.40$. The linear corrected one, in orange, highlights that point 2 was obtained by exhausting all of the remaining formability in plane strain (λ_{post}), or in other words, it represents necking. Point 1 is translated to its new position by changing its original λ_{pre} to λ_{cor}, as shown in Figure 4.9 (b) and (c). Note that repositioning point 1 in the plane strain direction, via λ_{cor}, and adding the same exact post-forming length leads to the intersection of point 2 with the linear FLC, as expected. Therefore, any arbitrary point between 1 and 2 would still have some formability remaining. Thus, for any bilinear strain history that does not end with necking, either by not reaching or even surpassing it, it is possible to define the relative position of the end point of a linear equivalent history, in relation to the linear FLC. Since multilinear strain paths can be subdivided in diverse bilinear strain segments, the previous analysis can be applied as many times as needed.

Volk *et al.* (2013) used the example in Figure 4.10 to illustrate the application of this concept, for the multilinear strain path shown in blue. The values presented in Table 4.1 are used to help understanding the procedure. First, all the linear paths (P) are considered isolated from one another and their respective parameters determined, namely β_{pre} and λ_{pre}. This is done so that the nomenclature can be maintained without the need to introduce more variables. Then, each bilinear segment (S) is sequentially analysed with the metamodel. By accessing the total strain path length ratio database, the post-forming for the specific bilinear segment in study can be calculated with equation (4.14). If needed, the value can be obtained

based on the interpolation between the known four post-forming points. Starting with the first segment (S0→2), after λ_{post} is calculated, λ_{cor} is determined with equation (4.17) and the first path (P0→1) changes its orientation to match the second path (P1→2). With equal β the general forming effect of both paths can be added. A new linear path is created, corresponding to the red line in Figure 4.10. At this time, the second segment (S1→3) is constituted by the newly created linear path and the next one. The process is simply repeated until only one final linear segment exists. This example highlights the importance of this evaluation method. What appeared to be a failed forming attempt that could easily lead to failure, turned out to have remaining formability.

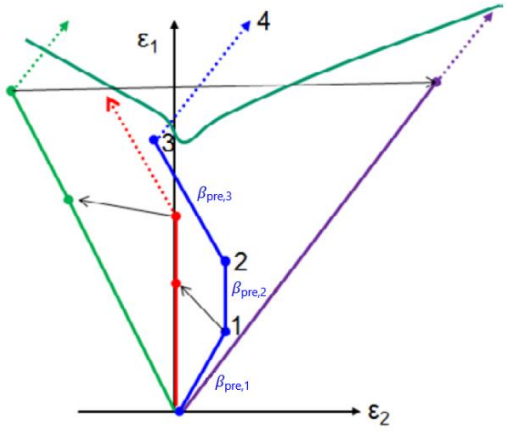

Figure 4.10. FLD of an application of the GFLC to an arbitrary stretch condition with four individual strain segments and calculation of beginning instability in the final equibiaxial direction (altered) (Volk *et al.*, 2013).

Posterior studies pointed out to the high accuracy of this phenomenological approach and metamodel, which always enables the prediction of the failure strains with an accuracy higher than 90%. This also validated the authors' hypothesis that the number of studied nodes is enough for the desired prediction quality (Jocham *et al.*, 2017). Moreover, high accuracy in the prediction of the local necking for the steel HC450X with the metamodel based on the data collected for the HC300X was also observed (Volk *et al.*, 2012). The same occurred when the metamodel for the aluminum AA6016-T4 was applied to predict the behavior of the AW-5754 (Jocham *et al.*, 2015). Therefore, the phenomenological approach can be extended not only to the same material grade but also to the material class, since they seem to share the same formability behavior. Nowadays, it is considered a reliable tool for evaluating non-linear strain paths and it was even applied as a

calibration method for experiments, such as the Nakajima and Marciniak tests (Volk and Gaber, 2017).

Table 4.1. Values of the different parameters for the application of the GFLC to an arbitrary stretch condition with four individual strain segments and calculation of beginning instability in the final equibiaxial direction (Volk *et al.*, 2013).

	β_{pre}	λ_{pre}	β_{post}	λ_{post}	λ_{cor}
P0→1	0.5	0.2	Evaluation of bilinear model ↓		
P1→2	0	0.3			
P2→3	-0.5	0.36			
P3→4	1				
S0→2	0.5	0.2	0	0.73	0.27
S1→3	0	0.27+0.3	-0.5	0.47	0.53
S2→4	-0.5	0.53+0.36	1	0.18	0.82
S3→4	1	0.82	1	0.18	

5. CASE STUDIES

Three case studies, consisting of different automotive body panels, were considered in this work and are presented in this chapter. The first (case study A) corresponds to a fender and the second (case study B) to an inner liftgate (see Figure 5.1). The analysis of these cases is focused on the impact of small changes in the description of the orthotropic behavior of the material on the prediction of defects, by either the linear or the non-linear FLC. The third component (case study C) is another inner liftgate (Figure 5.1), which is currently in the production line. In this case, the analysis focused on trying to understand why defects such as wrinkles occur for specific coils, which involved a thorough description of the process and material properties. Based on the analysis, some changes to the originally proposed method plan are also discussed.

Case study A Case study B Case study C

Figure 5.1. Case studies: fender and inner liftgates.

5.1. Common Features

In this section, the common features considered for the three case studies are summarized. These are considered in all the simulations made, except when stated otherwise. The values used for the numerical parameters described in chapter 2, are those recommended by AutoForm® for a final validation of the tool's design. This translates in fine meshes and large CPU times, but the performance was not considered has a relevant issue. The blanks were discretized with EPS elements, with 11 points of integration through the thickness. The mesh refinement control parameters are listed in Table 5.1, which also resumes the control

parameters for the tools. The drawbeads are modelled using their geometry, since at the final validation of the tool's design all CAD models are already created. A pressure dependent friction model is used, with a $cof = 0.15$, $p_{\mathrm{ref}} = 2$ MPa and $e = 0.9$ (see equation (2.12)). Considering the size of the components, AutoForm® recommends a tool stiffness of 10 MPa/mm, which was used for all non-rigid tools.

Table 5.1. Numerical parameters defined according with AutoForm®.

	Parameter	Value
Mesh refinement	*radius penetration*	0.22 [mm]
	max element angle	22.5º
	initial max element size	10.0 [mm]
	max refinement level	5 [-]
	tangential refinement	on
Tools control	*max material displacement*	2.2 [mm]
	min tool displacement	1.87 [mm]
	max tool displacement	5.5 [mm]
	end tool displacement step	0.25 [mm], in the 5 final steps

All the components in this study are cold drawn, so the temperature effects can be neglected. It is assumed that the forming process is isothermal and no thermal expansion occurs. It should be noted that some material parameters, like the volumetric heat capacity and conductivity, are defined but not used in the simulations.

5.2. Materials

The Volkswagen® group has a standard material library that is used by the sheet metal method planning engineering team. It consists of a collection of .mat (or .mtb) files, to use directly in AutoForm®, that define the elastic and thermal material properties, the hardening law, the yield surface and the FLC.

Two galvanized steels (code Z) were used in this study: a DX54D and a DX56D, according to the EN10346 standard. These are equivalent to CR3 and CR4 (code GI), respectively, according to the VDA 239/100 standard. The material chosen for component A is the DX54D steel, while components B and C both use DX56D. The DX54D blank has an initial thickness of 0.6 mm while the DX56D blanks have 0.7 mm. The standard material library defines the isotropic hardening of both materials with the Swift-Hockett/Sherby law

(see equation (2.19)). Table 5.2 shows the corresponding material parameters and Figure 5.2 (left) compares the two hardening curves. In order to consider the biaxial strain, which is significantly larger than the uniaxial one, the software extrapolates the stress values until $\varepsilon^{\mathrm{p}} = 1$. The FLC is defined, in both cases, with a table of up to 50 pairs of strain values, which are represented in Figure 5.2 (right).

Table 5.2. Swift-Hockett/Sherby material parameter defined in the material library.

Material	α	C [MPa]	ε_0	m	σ_{sat} [MPa]	σ_i [MPa]	a	p
DX54D	0.2	605	0.01	0.275	430	160	6.25	0.835
DX56D	0.15	585	0.01	0.28	415	155	6.75	0.85

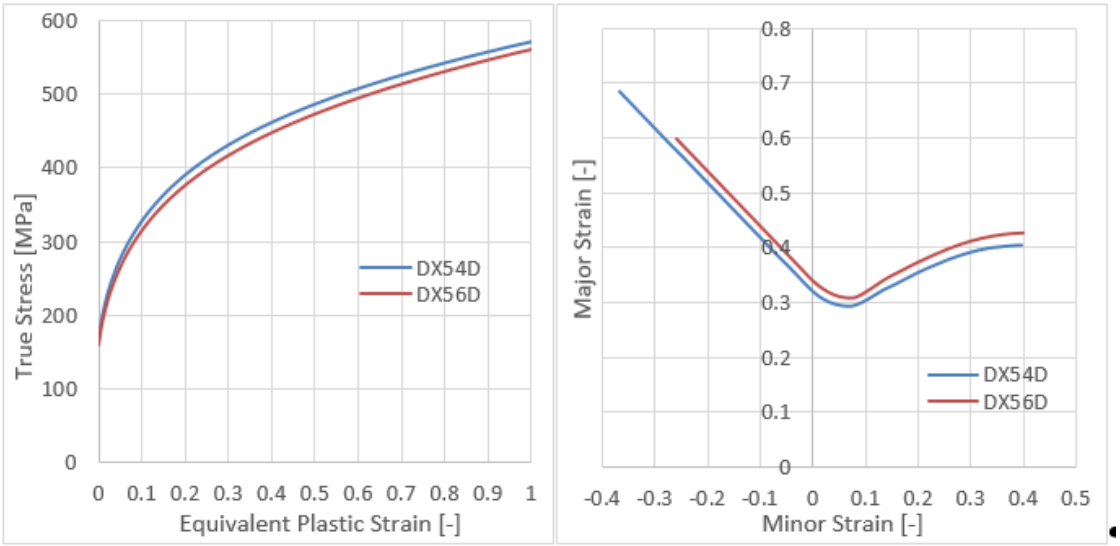

Figure 5.2. Stress *vs*. equivalent plastic strain curves (left) and FLCs (right) for DX54D and DX56D.

The standard material library considers the Hill'48 criterion for both materials. The input parameters used in the definition of the Hill'48 yield *locus* are presented in Table 5.3. The parameters shown in Table 5.4 are calculated using the equations presented in subchapter 3.1, enabling the user to observe possible discrepancies with the experimental behavior of the material. Figure 5.3 represents the two yield curves (left) and their normalized version (right), with the horizontal axis corresponding to the first principal stress and the vertical axis the second principal stress. The comparison between the two materials is made to highlight their similarities.

Table 5.3. Input parameter values of the Hill'48 criterion defined in the material library.

Material	σ_0 [MPa]	r_0	r_{45}	r_{90}
DX54D	168.4	1.5	1.2	1.9
DX56D	160.2	1.7	1.4	2.1

Table 5.4. Output parameter values of the Hill'48 criterion defined in the material library.

Material	σ_{45}/σ_0	σ_{90}/σ_0	σ_{ps0}/σ_0	σ_{ps90}/σ_0	σ_b/σ_0	σ_{shear}/σ_0	r_b
DX54D	1.127	1.045	1.284	1.341	1.182	0.567	0.789
DX56D	1.1151	1.0373	1.321	1.370	1.2215	0.560	0.81

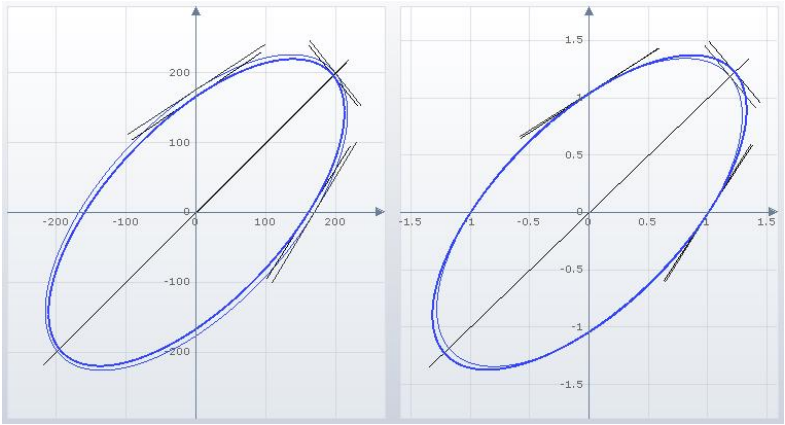

Figure 5.3. Hill'48 yield curves (left) and their normalized version (right) for DX54D (fine line) and DX56D (thick line), as they appear in AutoForm®.

5.2.1. Influence of the Equibiaxial Stress Value

Previous studies pointed out that the DX54D and the DX56D steels show an equibiaxial yield stress lower than the one given by the Hill'48 criterion (ten Horn, Vegter and Mouatassim, 2005; Wessel *et al.*, 2020). The change of this point in the yield *locus* can influence not only the equibiaxial stress but also the plane strain and shear stress states. The importance of these variations in the yield *locus* and, consequentially, on the prediction of forming defects on automotive parts is analyzed in this study.

Since there was no experimental information about the try-out material, the analysis of the influence of the equibiaxial stress value was made considering both the Hill'48 and the BBC 2005 criterion, since the last is known to be more flexible (see Table 3.1). The original material file was modified to consider the BBC 2005 criterion, considering the same uniaxial and equibiaxial stresses and coefficient of anisotropy has the ones

estimated by Hill'48. The exponent $M = 6$ ($M = 2k$ in equation (3.29)) was chosen, has recommended for BCC materials. Figure 5.4 and Figure 5.5 show the comparison between the normalized yield curves of the two criterion, for the DX54D and DX56D, respectively. The comparison between the two yield curves shows a slight difference in the shear stress point and a more noticeable one for the plane strain. The following approach was to use the Biax parameter to alter the shape of the yield *locus*, for both Hill'48 and BBC 2005. The values of $Biax = 0.9$ and $Biax = 1.1$ were considered to try and capture a 10% variation in this parameter, taking as reference the defined material in the library. The analysis of Figure 5.4 and Figure 5.5 shows that the change of the Biax parameter alters all the characteristic points of the *locus*, except the uniaxial stress states. Table 5.5 and Table 5.6 show the variation of the output normalized stresses, for the Hill'48 and BBC 2005 criteria, with respect to Biax, for the DX54D and DX56D steels, respectively.

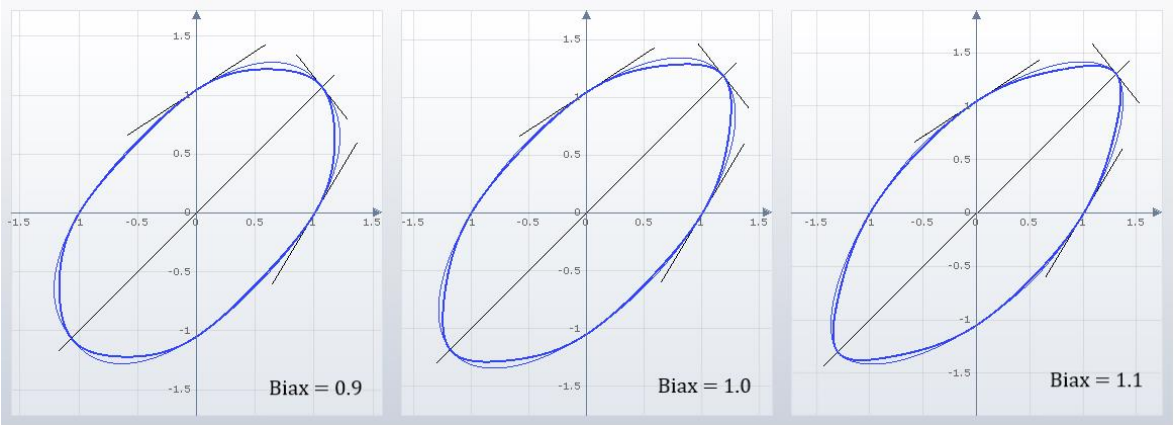

Figure 5.4. Comparison between the Hill'48 (fine line) and BBC 2005 (thick line) normalized yield curves for DX54D, as they appear in AutoForm®.

Table 5.5. Output parameter values of the yield criteria defined in the material library for DX54D.

Biax	Yield Criterion	σ_{ps0}/σ_0	σ_{ps90}/σ_0	σ_b/σ_0	σ_{shear}/σ_0
0.9	Hill'48	1.213	1.277	1.0638	0.559
	BBC 2005	1.168	1.218	1.0638	0.550
1	Hill'48	1.284	1.341	1.182	0.567
	BBC 2005	1.247	1.285	1.182	0.556
1.1	Hill'48	1.366	1.412	1.3002	0.573
	BBC 2005	1.346	1.375	1.3002	0.560

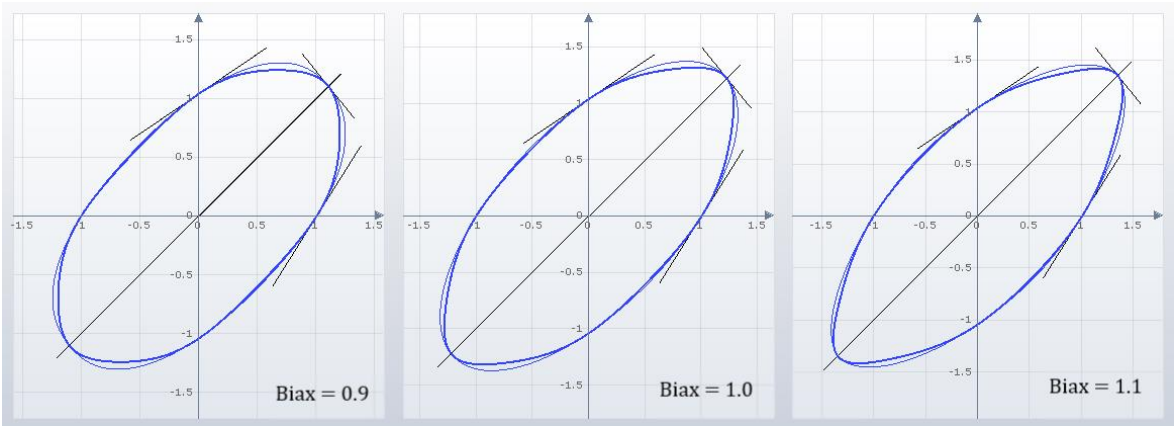

Figure 5.5. Comparison between the Hill'48 (fine line) and BBC 2005 (thick line) normalized yield curves for DX56D, as they appear in AutoForm®.

Table 5.6. Output parameter values of the criteria defined in the material library for DX56D.

Biax	Yield Criterion	σ_{ps0}/σ_0	σ_{ps90}/σ_0	σ_b/σ_0	σ_{shear}/σ_0
0.9	Hill'48	1.244	1.299	1.0994	0.554
	BBC 2005	1.196	1.237	1.0994	0.546
1	Hill'48	1.321	1.370	1.2215	0.560
	BBC 2005	1.283	1.314	1.2215	0.551
1.1	Hill'48	1.408	1.447	1.3437	0.566
	BBC 2005	1.387	1.411	1.3437	0.555

5.3. Case Study A

The fender will be produced in a single-action press. The die constitutes the ram of the press, while the punch and binder form the bed. The punch and die are considered rigid since they are fixed to the bed and ram of the press. The binder force is applied with cushion pins. The binder is considered to be spring controlled with a cushion stroke of 200 mm. However, a uniform preload of 940 kN was defined instead of using the cushion pin locations. This procedure is valid since a partial bearing was established in the finite element model, i.e. a noncontact area between the binder and the blank was predefined. Note that the partial bearing is directly connected with a try-out strategy, where the technicians rectify the surfaces of the tools so that only a specific region is used to apply the binder pressure to the metal sheet. Figure 5.6 shows the pressure distribution predicted by the model where a partial bearing was defined, using the drawbead line. It is clear that there is a pressure ring

associated to the drawbead geometry, but the surface immediately after the innermost drawbead shows no pressure. Moreover, considering that the cushion pins are positioned significantly far from the pressure ring, it is not justifiable to implement them in the numerical model, unlike in the example given in Figure 2.6. The same applies to the other two case studies. Note that in AutoForm®, the partial bearing can be defined with the line of the drawbead or manually by the user.

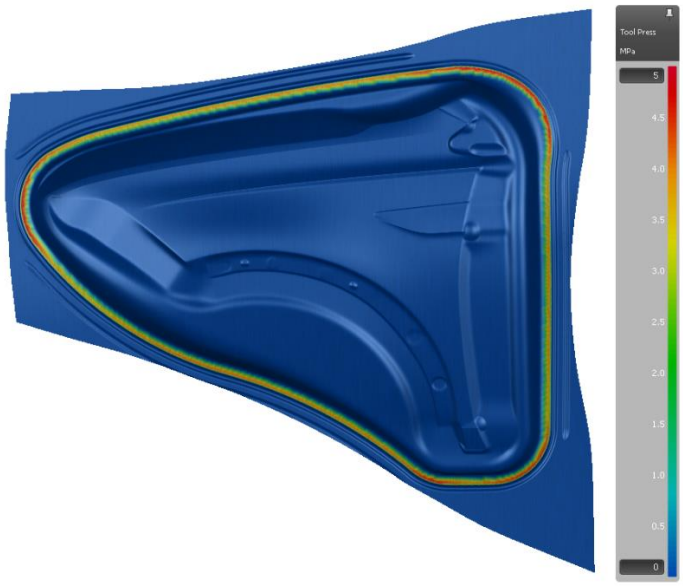

Figure 5.6. Pressure ring in the final step of the fender's forming process, taken from AutoForm®.

The analysis of formability was performed using both yield criteria, combined with the linear and non-linear FLC. As shown in Figure 5.8, the strain space associated with the linear FLC is divided in six zones: thickening, compression, insufficient stretch, safe, risk of splits and splits. The non-linear FLC is divided only in three zones: safe, risk of splits and splits. The risk of splits zone was user defined with a 20 % margin regarding the FLC. Figure 5.8 shows the results obtained with the Hill'48 yield criterion, while Figure 5.9 shows the ones obtained with the BBC 2005. Globally, the results allow identifying three critical regions: one in the front-end region, located close to the plane strain state; another on the small details in the top right end region, located close to the uniaxial stress state; and, the last in the small detail, highlighted with the red transparent circle in Figure 5.7. The strain path for the last critical region was selected for further analysis, since it clearly shows a non-linear trend. The closest point, relative to the non-linear FLC, is chosen to represent the strain-path. Note that its respective position is plotted also in the linear FLC, in Figure 5.8

and Figure 5.9. The strain path is identical in all non-linear FLC representations; starts with a combination of plane strain and equibiaxial strain, changes to an almost equibiaxial path and ends in plane strain. The selected point exhausts more formability than the one predicted by the linear FLC, due to these strain path changes, whatever the yield criterion considered and the value for the Biax parameter. In this context, this example highlights the importance of the non-linear FLC.

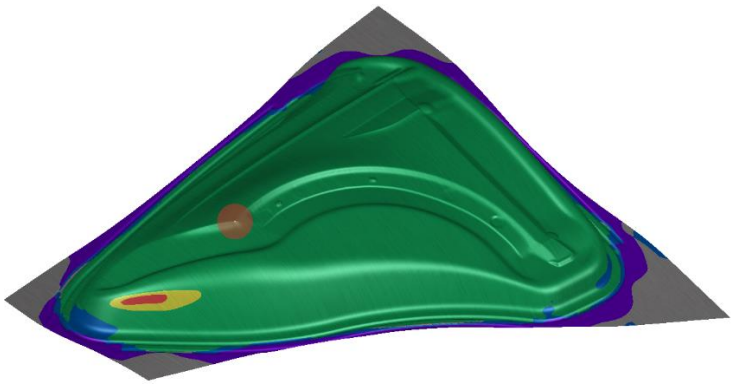

Figure 5.7. Critical regions of case study A for the BBC 2005 criterion using Biax = 0.9. For the color code, refer to the caption of Figure 5.8.

Regarding the influence of the Biax parameter, this example shows that it can even change the number and location of the critical regions, whatever the yield criterion adopted. Moreover, it is interesting to note that although the yield curves of both criteria seem quite identical (see Figure 5.4), the predictions with the Hill'48 are more conservative, whatever the value selected for the Biax parameter. This is certainly related to the changes induced by the yield *locus* shape in the strains distributions in the part. The previous experience with similar parts indicates that splits tend to occur in the more critical region determined with Biax = 0.9. This corresponds to the red and yellow regions in Figure 5.7. Since the strain path for these material points is linear throughout the drawing process, close to plane strain, this indicates that the yield *locus* for this material should be better represented by the one obtained with this value of Biax. This goes in line with the previous research on this material class, which indicates that the equibiaxial stress is lower than the one predicted by the Hill'48 criterion.

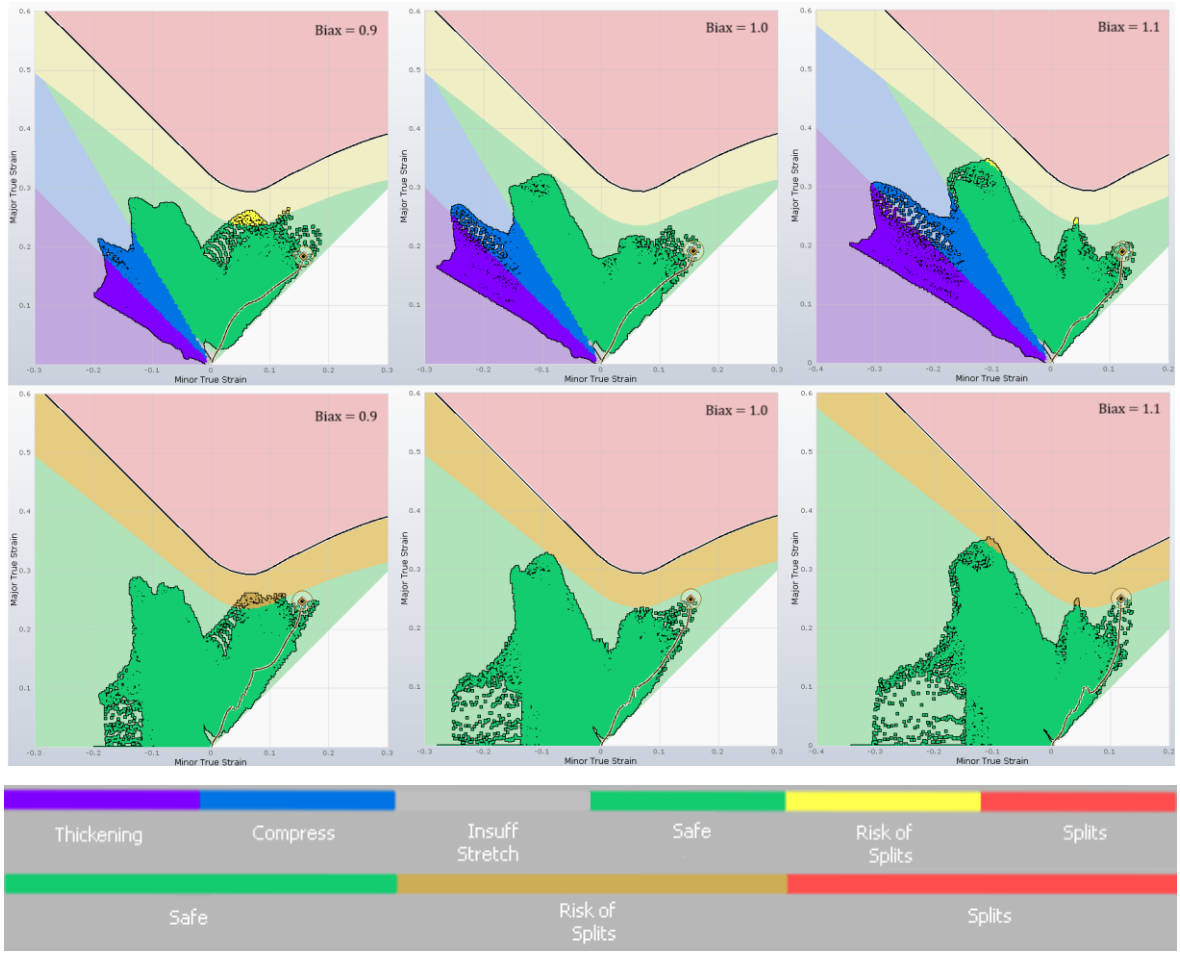

Figure 5.8. Case study A FLCs (above) and non-linear FLCs (below) with Hill'48, taken from AutoForm®. Color code of the linear FLCs (above) and of the non-linear FLCs (below), taken from AutoForm®.

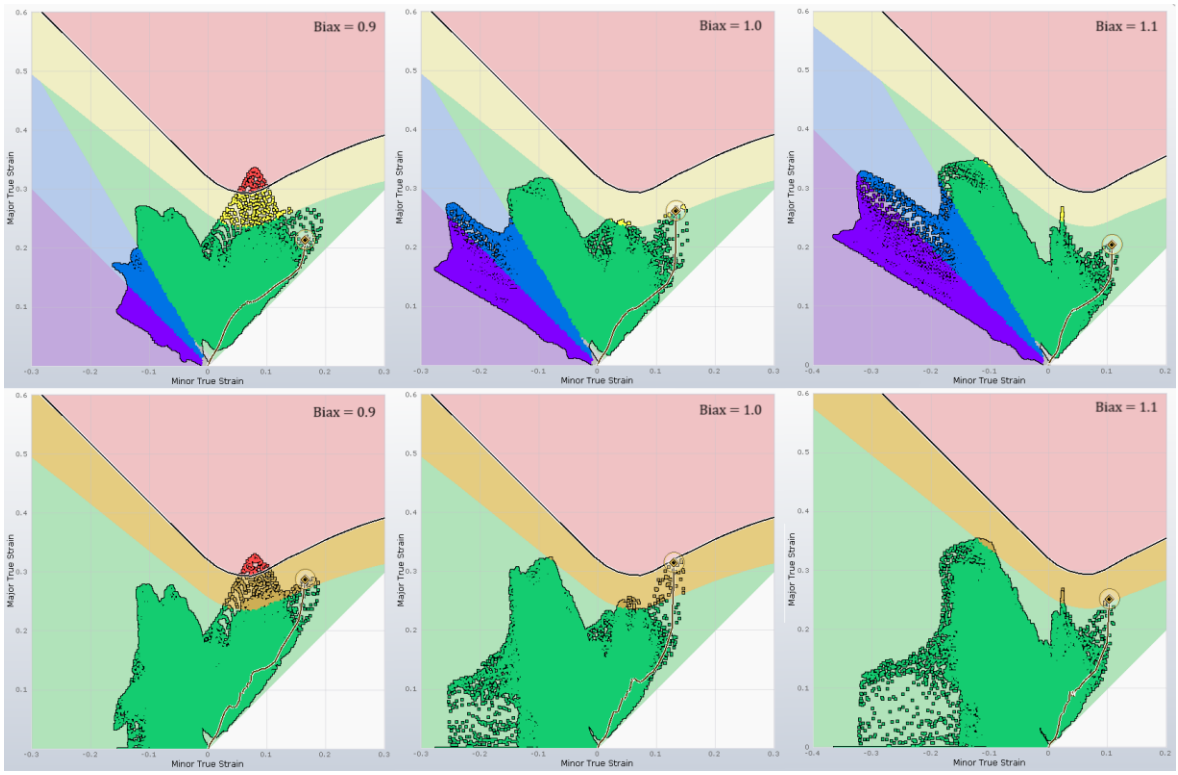

Figure 5.9. Case study A FLCs (above) and non-linear FLCs (below) with BBC 2005, taken from AutoForm®. For the color code, refer to the caption of Figure 5.8.

5.4. Case Study B

A triple-action press is normally necessary for producing inner liftgates, due to their greater geometrical complexity. When defining the process, the ram must include the die and the upper blankholder, which pair with the bed's punch and lower blankholder. Special attention must be given to the tools' kinematic. The blankholder forces must be defined considering the order by which the tools will close. Two ideal scenarios can happen: the lower blankholder has enough force to withstand the upper blankholder force, maintaining its position during the upper stroke; or the upper blankholder has more force than the lower one, forcing it down immediately after they close. This establishes which of the cushion strokes is done first. The way the sheet interacts with the punch and die is completely different in each case, altering the strain paths in the part. In fact, these interactions create deformation in the blank during the cushion stroke that result in additional reaction forces that counter the binder force. These should always be considered, independently of the kinematic scenario.

As in case study A, a cushion system is used to apply the binder force. The difference between the previous case and this one is the existence of an upper set of cushion pins, transferring a force of 900 kN into the upper blankholder. The lower blankholder is prescribed with a force of 1500 kN, resulting in the first kinematic scenario. This means that, after the blankholders close, the lower blankholder sustains the upper one. An initial binder force of 900 kN is applied to the sheet. While the die lowers to the prescribed cushion stroke of 100 mm, the force applied by the lower blankholder rises to compensate the blank's deformation. Ideally, the defined lower blankholder force should not be reached at the end of the die cushion stroke. This means that there must be a difference between the upper and lower blankholder forces, big enough to account for the resultant force from the sheet deformation. Once the die cushion stroke is reached, the upper blankholder contacts with the ram and, from this point on, the transferred force is no longer constant, being free to increase as needed. This rise in force displaces the lower blankholder, which will maintain its prescribed 1500 kN of force throughout the lower cushion stroke of 80 mm.

In this case, the support type chosen for both blankholders was force controlled. The preliminary numerical simulations showed that the force of 900 kN imposed to the upper blankholder was not enough to keep the blankholders closed. Therefore, some virtual try-outs were performed that lead to a value of force for the upper blankholder close to 1100 kN. This value was used to perform numerical simulations with both yield criteria, considering the different values for the Biax parameter (see Figure 5.5). Figure 5.10 and Figure 5.11 show the formability predictions, using the linear and non-linear FLC, considering the Hill'48 and BBC 2005 criteria, respectively.

In this case, the analysis of the closest point, relative to the non-linear FLC, always leads to an identical region in the part, whose location is highlighted with the red transparent circle in Figure 5.12. This point was chosen to represent the strain-path, in both the linear and the non-linear FLC. The particular point selected goes through the curvature region (close to plane strain path) and is then expanded in the almost vertical wall (close to equibiaxial path). Note that the linear FLC would not predict this location of a potential split, unlike the non-linear FLC, for Biax values of 0.9 and 1.0, for both yield criteria. In fact, the region that is in the risk zone for the non-linear FLC has remaining formability in the linear FLC. This is certainly related to the lower formability predicted for combined biaxial and

strain paths (see Figure 4.2). These results highlight the importance of taking into account the strain paths changes in the formability analysis, whatever the yield criteria adopted. As for case A, globally, the formability predictions with Hill'48 are more conservative. Nevertheless, the only numerical simulation for which the selected point is not the closest to the non-linear FLC is the one performed with the BBC 2005 criterion and Biax $= 1.1$. The higher equibiaxial resistance leads to a lower increase in the principal strains, but this is certainly related to the change induced to the plane strain values (see Figure 5.5).

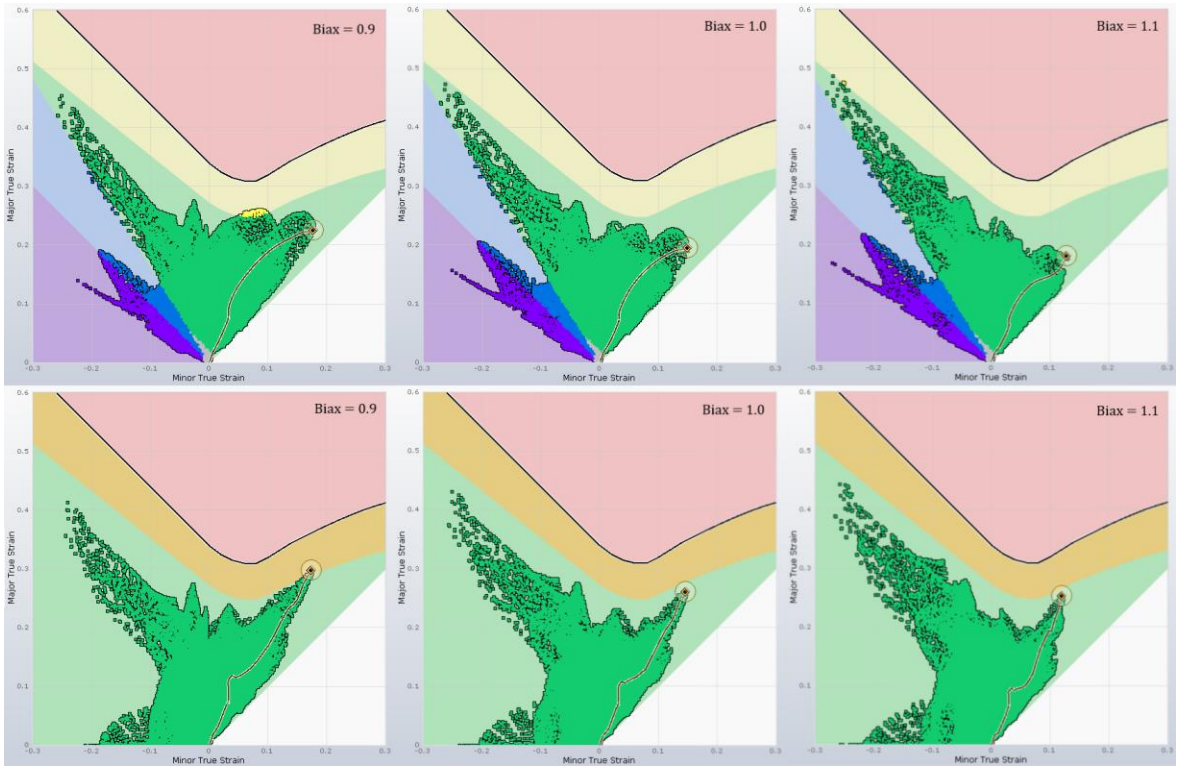

Figure 5.10. Case study B FLCs (above) and non-linear FLCs (below) with Hill'48, taken from AutoForm®. For the color code, refer to the caption of Figure 5.8.

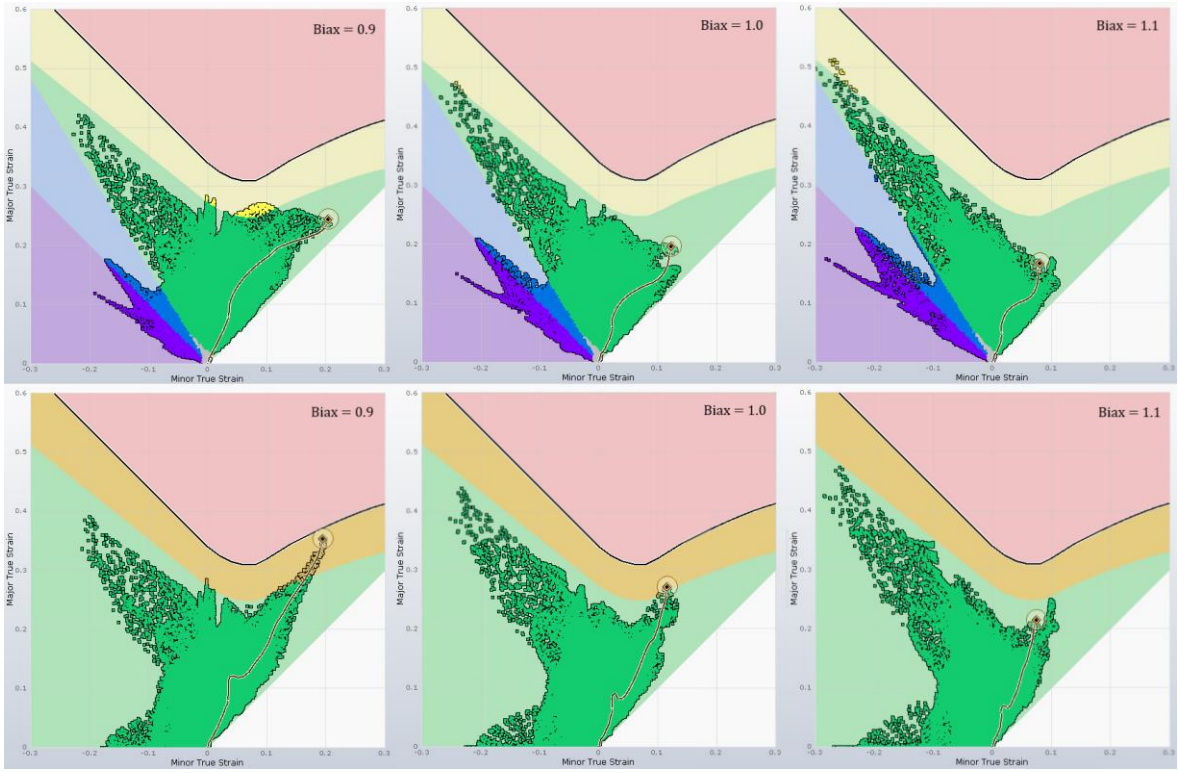

Figure 5.11. Case study B FLCs (above) and non-linear FLCs (below) with BBC 2005, taken from AutoForm®. For the color code, refer to the caption of Figure 5.8.

Figure 5.12. Case study B: Formability analysis of the final step using BBC 2005 and $\mathrm{Biax} = 0.9$, taken from AutoForm®. For the color code, refer to the caption of Figure 5.8

5.5. Case Study C

The method plan implemented for the inner liftgate selected as case study C uses the same kinematic behavior for the tools as the case study B. Figure 5.13 shows the tools used in the simulation. A uniform force was chosen for the upper blankholder, within a range between 1000 kN and 1100 kN. This interval is supposed to capture the spring behavior of the set of nitrogen gas cylinders selected to apply the force. The upper cushion stroke of 120 mm is the first to occur. The lower blankholder has a uniform force of 1400 kN, provided by cushion pins, and a cushion stroke of 50 mm. Both blankholders were modelled with force control and neither lacked force, throughout the simulation.

As previously mentioned, the material selected for this component is the DX56D. The numerical simulation of the forming process previously described, which will be designated by initial method plan, was performed considering the information available in the Volkswagen® group standard material library (see Figure 5.3). The formability results based on the linear and non-linear FLCs are represented on Figure 5.14. The figure shows some points within the risk of presenting splits, but only if a safety margin of 20% is considered. Also, the points within the risk of presenting wrinkles are located in the regions that will be trimmed. Therefore, this method plan was validated for production.

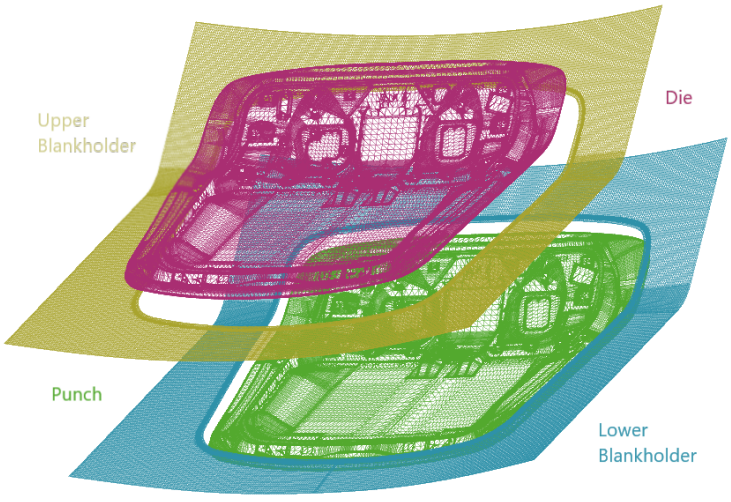

Figure 5.13. Case study C: Mesh representation of the tools for the initial method plan.

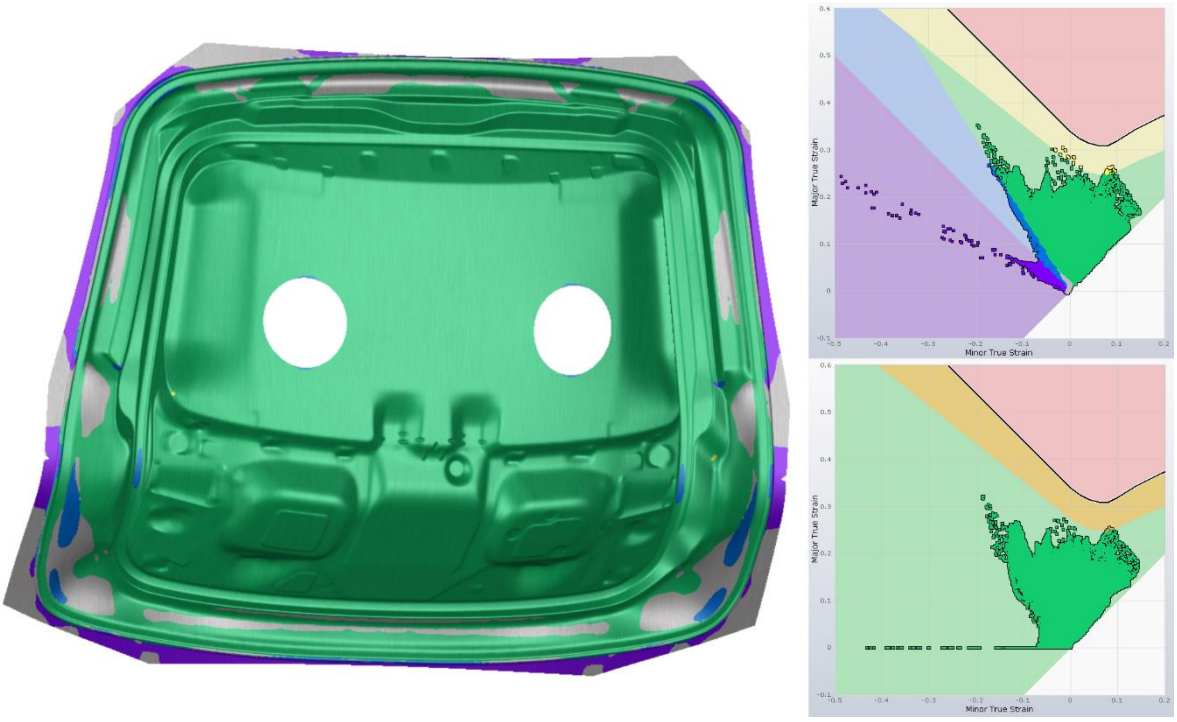

Figure 5.14. Case study C: Final step forming results of the initial method plan (left) and linear and non-linear FLCs (right). For the color code, refer to the caption of Figure 5.8.

However, the analysis of the process implemented in the production revealed that a different kinematic was being used for the tools. The lower blankholder initially withstands the upper blankholder force but, eventually, goes down in the middle of the upper cushion stroke. This means that, at some point in the upper cushion stroke, the sum of the forces of the upper blankholder and of the die exceed the cushion force. From there on, two scenarios can happen: the lower cushion stroke is completed and then the remaining upper cushion one; or an unpredictable process can unfold. It should be mentioned that, this alternative method plan was implemented in the production, due to the occurrence of a defect that was not predicted by the numerical simulations of the initial method plan, as will be discussed in the following subchapter. This alternative method plan enables the production of good quality inner liftgates. Unfortunately, for a few material coils it leads to the occurrence of wrinkles, because different mechanical properties alter the force required to deform the sheet and, consequentially, the tool kinematic. This means that time and money are consumed in try-out, to achieve a defect free part and, in the end, some of these coils can still be rejected.

5.5.1. Analysis of the Initial Process conditions

Some alterations were made to the initial method plan in order to improve the control and reduce the occurrence of defects. One of them was the change of the drawbeads geometry to help retain the sheet during the forming process. Therefore, the changes made to the drawbeads were measured, in order to alter the CAD files and enable their inclusion in the numerical models that will be used in the following analysis. Another was the separation of the set of cylinders into independent sets, to enable a better pressure control of the upper blankholder. The impact of these changes to the initial method plan is discussed in this section.

5.5.1.1. Cylinders force

The upper blankholder force is imposed by twelve standard FIBRO® nitrogen gas cylinders, each showing a minimum and maximum charging pressure of 25 and 150 bar, respectively. Figure 5.15 (left) shows the increase of the initial force with the charge pressure. At 150 bar the cylinder applies a force of 100 kN, meaning that the effective area of the cylinder is $A = 6.667 \times 10^{-3}$ m^2. Figure 5.15 (right) shows the increase of the pressure rise factor with the displacement. Since each cylinder has a maximum nominal stroke of 160 mm, that was the curve selected to determine the pressure rise factor.

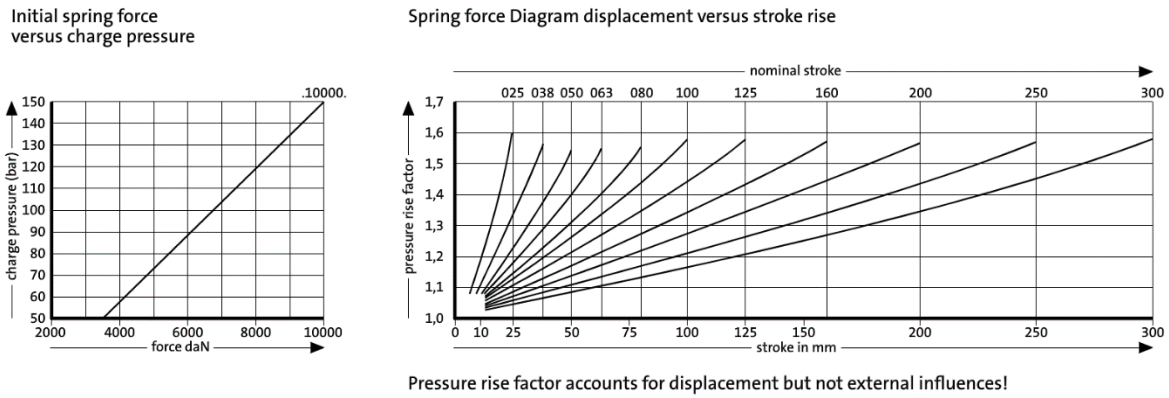

Figure 5.15. Force diagrams of the FIBRO® standard nitrogen gas cylinder, order nº 2480.12.10000.160 (*FIBRO® Standard Parts Catalog*, 2014).

Considering that at 160 mm the pressure rise factor is 1.58, the slope in Figure 5.15 (right) is $m = [(1.58 - 1)/160] = 3.625 \times 10^{-3}$ /mm. The pressure of the cylinder p_{cyl} is related to its charge value, p_{charge}, by:

$$p_{\mathrm{cyl}} = p_{\mathrm{charge}} + mdp_{\mathrm{charge}}, \tag{5.1}$$

where d is the displacement in mm. This means that the force of the cylinder, F_{c}, can be given as a function of its displacement and initial charge pressure, as follows:

$$F_{\mathrm{c}} = A(1 + md)p_{\mathrm{charge}} \times 10^2. \tag{5.2}$$

Note that, since p_{charge} is in bar, the factor 10^2 is introduced to calculate the force in kN.

In the initial setup, all the twelve cylinders shared the same charge pressure. Thus, the total force applied to the upper blankholder was twelve times the value given in equation (5.2). According to the process conditions for the initial method plan, the maximum stroke of each cylinder was 120 mm. This means that it is impossible to attain the range of force between 1000 and 1100 kN. Note that to achieve a final force of 1100 kN after the upper cushion stroke, each cylinder would have around 95.8 bar of charge pressure and the total initial force would be approximately 766.55 kN. This is probably the main reason why problems started to occur in the try-out, leading to the alteration of the process in the production.

5.5.1.2. Experimental and Virtual Try-out

Experimental try-outs were made considering the initial method plan, but with three different conditions for the cylinders and the cushion force. Figure 5.16 shows the positions of the cylinders relative to the blankholder and the punch. The color code indicates the set of cylinders that work with equal charge pressure. Table 5.7 shows the cushion force and the cylinders initial pressure, used in the experimental try-outs. Try-out number one serves as the reference, with a cushion force of 1400 kN has defined in the initial method plan. In the try-out number two, the upper blankholder force is changed. In both cases, the pressures for the cylinders were taken directly from two production conditions. In the try-out number three, the cushion force was reduced to around 1100 kN, while the upper blankholder force is equal to the one used in try-out number one.

Regarding the virtual try-out, some challenges arise when trying to replicate the process kinematics. Note that the range of force considered for the upper blankholder may lead to the tools opening during the process. This means that spring controlled is the most accurate way to model both blankholders. As shown previously in Figure 5.6, cushions pins can be modelled with a uniform loading, when trying to capture the pressure ring effect.

Nevertheless, since the cylinders show different forces, the columns model seems more appropriated. However, columns can only be defined with an opposite rigid tool, which cannot move. This is not ideal, considering that the lower blankholder needs to move once the upper cushion stroke ends.

Figure 5.16. Position of the cylinders in the upper blankholder and corresponding sets defined by color.

Table 5.7. Experimental try-out forces used.

Try-out Number	Cylinder Charge Pressure [bar]				Cushion Force [kN]
	Green	Yellow	Blue	Red	
1	60	100	100	125	1400
2	90	80	110	120	1400
3	60	100	100	125	1100

To work around the previously mentioned difficulties, a model was built considering two drawing processes, defined in succession, without springback in between. The first process contemplates the upper cushion stroke with a rigid lower blankholder and a spring controlled upper one, enabling the use of the columns model. In the second process, the lower cushion stroke is made with both blankholders defined with spring control. It should be noted that for the cushion strokes to be maintained in the simulation, the initial position of the punch in the first drawing had to be moved 50 mm down. This numerical model will be designated by two drawing processes, in the subsequent analysis. The numerical simulations were also performed considering the same kinematic conditions as for the initial method plan, by altering the total force of the upper blankholder and the

cushion force, according to the information presented in Table 5.7. This numerical model will be designated by single drawing process, in the subsequent analysis.

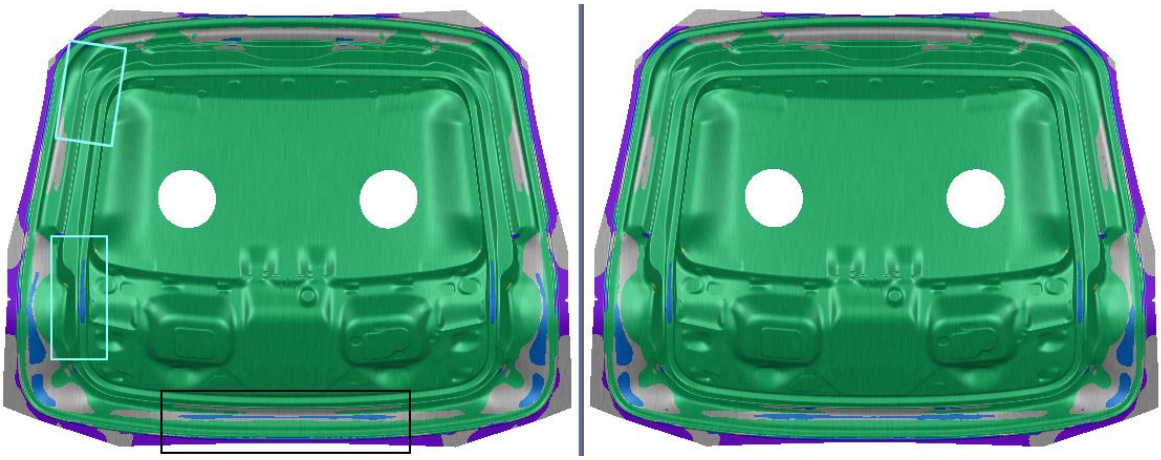

Figure 5.17. Forming results for the two drawing processes (left) and for the single drawing (right). For the color code, refer to the caption of Figure 5.8

The numerical simulations were performed with both models, considering the BBC 2005 criterion with Biax $= 0.9$ (see Figure 5.5), based on the analysis made in the two previous case studies, which indicate that it can lead to a more accurate representation of the yield surface. The results obtained for the conditions of try-out number one, with the single and the two consecutive drawing processes, are compared in Figure 5.17. The differences in formability are minor, with the risk of splits being predicted for the same location as seen in Figure 5.14. The minor differences in formability result from the different pressure distribution during the upper cushion stroke, which is compared in Figure 5.18. Due to the assumptions considered in the single process, the pressure ring presents a uniform pressure, which does not reflect the uneven distribution of pressure imposed to the cylinders, captured by the two drawing processes model.

In the production, a high pressure value is prescribed to the cylinders located in the lower region of the part (see Figure 5.16 and Table 5.7) to impose more stretch and prevent the occurrence of wrinkles. The formability analysis indicates a zone in compression stress state, which can be associated with wrinkles (see the rectangle in Figure 5.17). To further analyze this type of defects, a criterion based on the lack of contact with the tools and the curvature between consecutive elements can be used, which indicates that the

wrinkles are generated at an instant corresponding to the middle of the simulation. The wrinkles appear in two almost symmetrical zones as can be seen in red in Figure 5.19, which presents the distribution of the wrinkle criterion in the part. The wrinkles are smashed by the radius of the die when it contacts the sheet, creating defects.

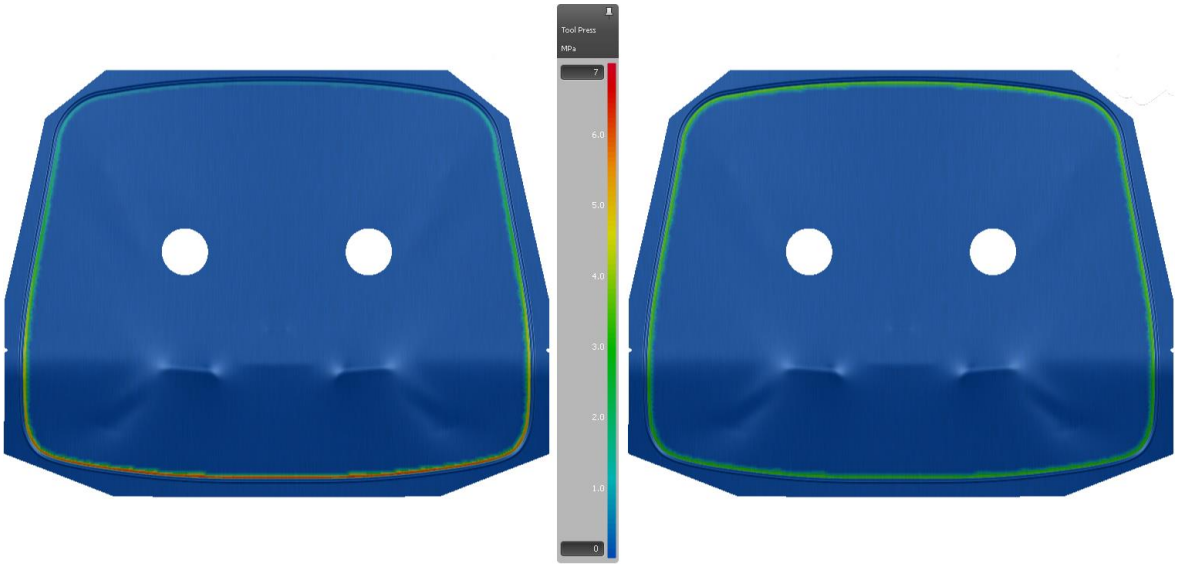

Figure 5.18. Pressure distribution of the two drawing processes (left) and of the single drawing (right).

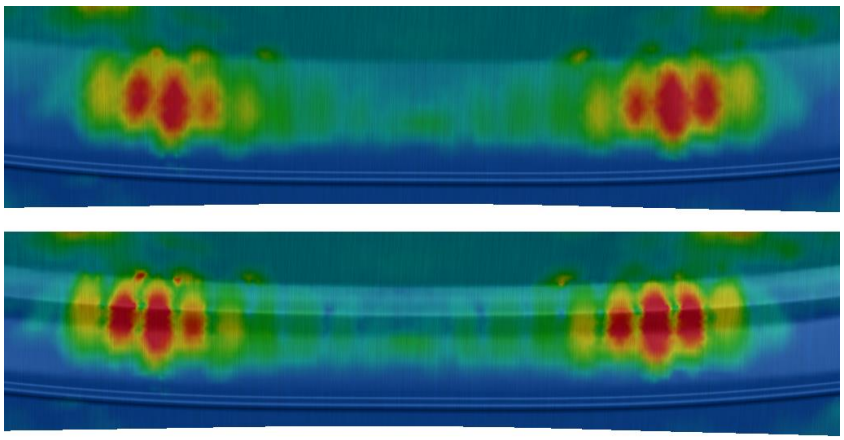

Figure 5.19. Wrinkling criterion distribution: wrinkles occur at an instant corresponding to the middle of the simulation (above) and the defect created by the contact of the die radius (below).

Although the wrinkling shown in Figure 5.19 corresponds to the results using the single drawing process model, the two drawing processes model also predicts the

occurrence of wrinkles in the region marked with a black rectangle in Figure 5.17. However, for the initial method plan, this type of defect is not visible in the part. The resulting tool forces are shown in Figure 5.20, for both the single and the two drawing processes. This figure shows that the initial upper blankholder force was not the predefined 1000 kN, of the initial method plan. This explains the occurrence of wrinkles, since there is not enough binder force to promote the stretching of the sheet. Moreover, Figure 5.20 highlights that the two drawing processes model has one inconvenience: the repositioning of the tools between the different drawings. Even though the surfaces are exactly the same, the software considers them as being different. This translates into a small alteration of the tools' forces. Nevertheless, this alteration is almost unnoticeable and it allows describing the differences in the pressure distribution (see Figure 5.18) and the resulting tilt of the tools during the process. For these reasons, the two drawing processes model is used in the following analysis, except if stated otherwise.

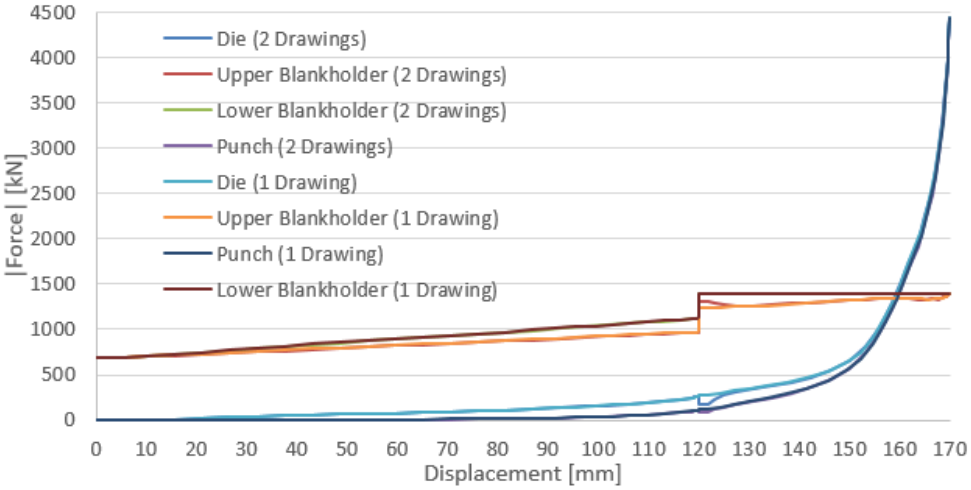

Figure 5.20. Tool forces comparison between the two drawing processes and the single drawing.

5.5.1.3. Draw-In Results

The deep drawn parts from the three experimental try-outs were 3D scanned to obtain their geometry in .stl files. These were converted into .igs files to extract the coordinates of the points that define the resultant surfaces in CATIA V5®. The coordinates of the points from the FE mesh of the final step of the simulations were also extracted. A Matlab® code was written to determine the points that constitute the boundaries of the parts. The Matlab® boundary function (MathWorks®, 2014) was used to determine the external

boundaries. To define the holes a convex hull gift wrapping algorithm, also known as Jarvis's march algorithm, (Cormen *et al.*, 2009) was used, but with the inverse purpose.

Figure 5.21 and Figure 5.22 present the experimental and the numerical draw-in results, respectively. Note that the theoretical blank format is used in the simulations. However, in production the trimming tools do not achieve the perfectly collinear borders of the blank, so in the corner regions some differences are naturally present. Also, in the experimental process there is a region where the binder applies pressure to the sheet outside the partial bearing. This is reflected in the formation of two ears in the top part of the component and the reduction in material flow (Figure 5.21) and also in a slightly higher positioning of the holes compared to the simulation. Despite these differences, the results show that the draw-in is sensible to the force conditions, particularly to the decrease of the cushion force, with the experimental and numerical results showing a similar trend. The expansion of the holes is also identical. Therefore, the defined material file seems to approximate the material behavior satisfactorily, at least for the coil used in the experimental try-out.

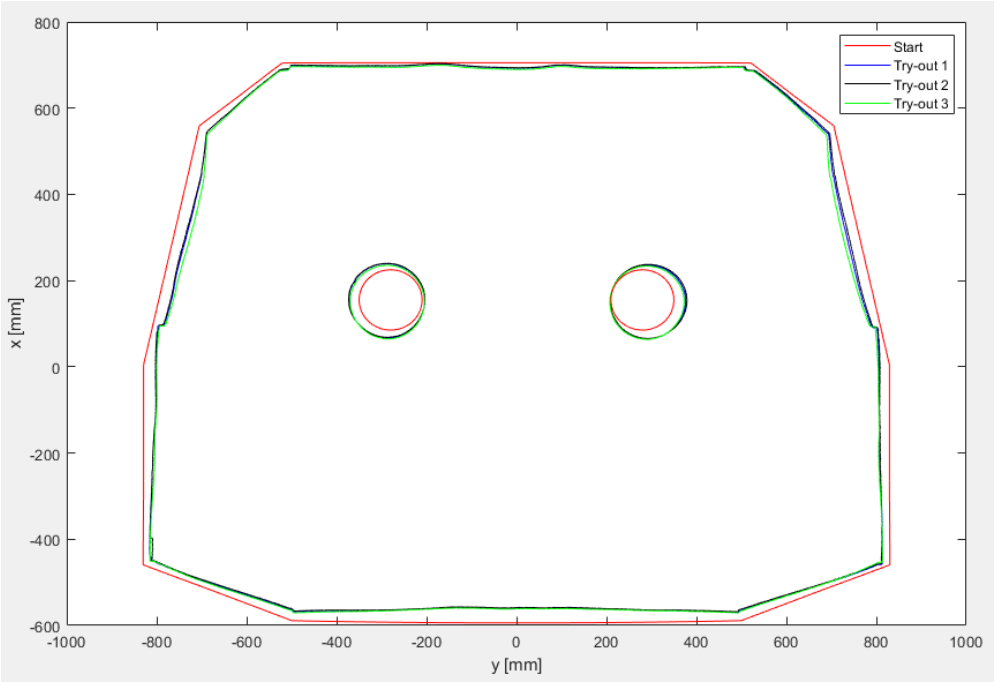

Figure 5.21. Draw-in comparison between the experimental results. The initial position of the blank is shown in red.

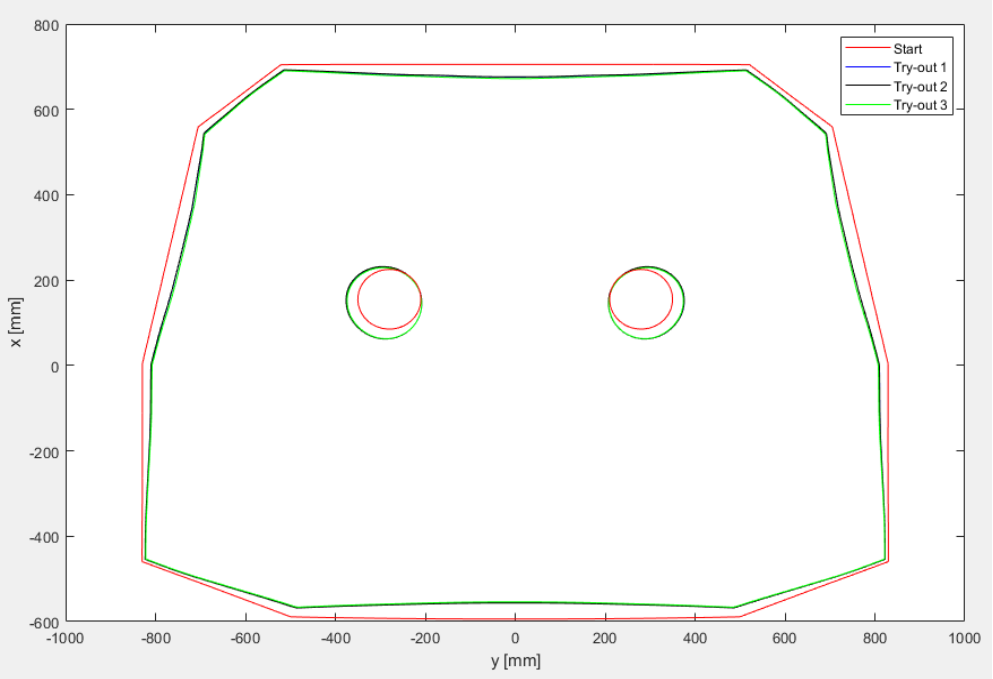

Figure 5.22. Draw-in comparison between the numerical results. The initial position of the blank is shown in red.

5.5.2. Analysis of the Alternative Kinematic

When defining the tools' kinematics for a triple-action press, AutoForm® automatically imposes the restriction that one of the blankholders' force must always be higher than the other one. If a force variation is defined, the maximum value cannot exceed the other's minimum. In practice, this automatic correction fixes the process conditions, guaranteeing its stability. Furthermore, this means that AutoForm® cannot simulate the tools' kinematic used in the alternative method plan. The division of the process into several different drawings is not feasible, since it requires the knowledge of the forces' evolution, which are unpredictable.

In order to improve the knowledge about the defects that appear with the alternative method plan, an experimental try-out was performed considering the inverse kinematics for the process, i.e. the lower cushion stroke is performed followed by the upper. The experimental part shows defects in two regions that are marked with the light blue rectangles in Figure 5.17, in the simulation corresponding to the two drawing processes. It is important to mention that these defects are not present in the parts being produced, since the forming conditions are fine-tuned in order to avoid them.

The two drawing processes model was used to simulate the previously described conditions, assuming a lower blankholder force with an arbitrary value of 400 kN. The material behavior was described by the BBC 2005 criterion with Biax $= 0.9$ (see Figure 5.5). Note that the single drawing process was found to be unable to completely close the blankholders at the end of the lower cushion stroke and that is why it is not shown. Figure 5.23 and Figure 5.24 show the results obtained for the regions showing defects, with the experimental result on the left side, the one predicted with the two drawing processes model in the middle, and the initial method plan on the right. The two drawing processes model is able to capture both types of defects, with wrinkles appearing at an instant corresponding to 5 mm before the end of the process, which ultimately lead to the final defects. Moreover, these types of defects are avoided in the initial method plan, which indicates that they are a consequence of the process kinematics.

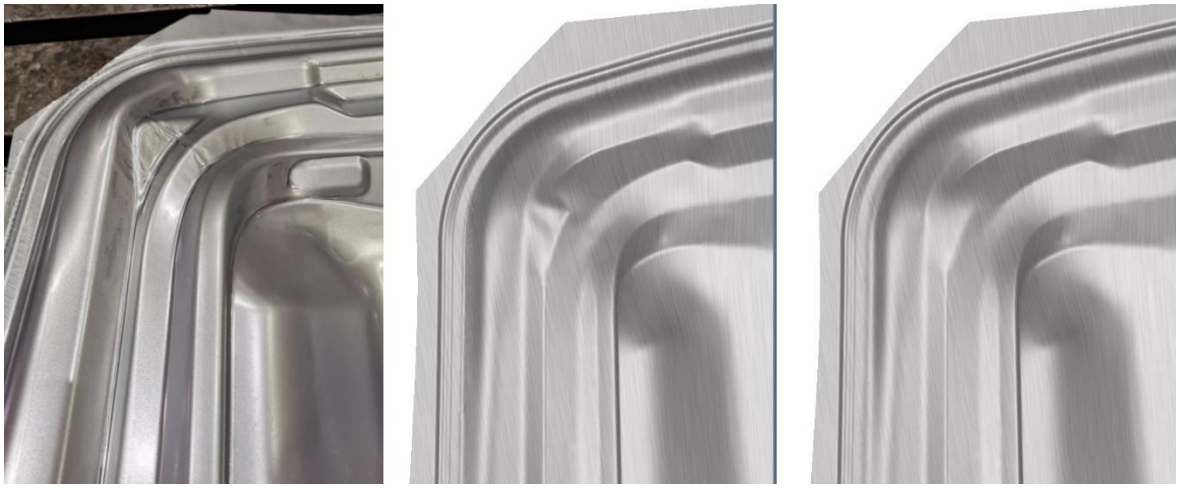

Figure 5.23. First defect that appears on the try-out with low cushion force (left), its detection at 5 mm before the end of the simulation (middle) and the equivalent with the initial method plan at approximately the same time step (right).

Figure 5.24. Second defect that appears on the try-out with low cushion force (left), its detection at 5 mm before the end of the simulation (middle) and the equivalent with the initial method plan at approximately the same time step (right).

5.5.3. Proposal of a New Method Plan

As discussed in the previous sections, the numerical simulation of the tools' kinematic adopted in the alternative method plan is unfeasible. Although this process can lead to some problems, a procedure is already established to try to minimize them, which enables the production of good quality parts. In this sense, any proposal to change the method plan needs to present clear advantages, while minimizing the required alterations. Taking into account these constraints, the kinematic proposed in the initial method plan is considered as reference. Nevertheless, as discussed in the previous sections, the opening of the tools during the upper cushion stroke is inevitable. The solution would be to increase the upper blankholder force and, in this sense, approximate the solution to what was originally envisioned. However, this would only be possible if the set of cylinders was completely changed for ones that have a lower variation of force per stroke. The ideal solution would be substituting the cylinders for cushion pins, but this is impossible since the press is not prepared to use an upper cushion system. On the other hand, it should be noted that the cushion strokes cannot be altered, since they are defined such that the blankholders close without the sheet establishing contact with any other tool. In other words, they are defined considering the depth of the geometrical details of the punch and the die. With the premise that no changes to the process conditions can be made, the only possible solution that seems

feasible to tackle the problem is to alter the tools in such a way that the wrinkling defects (see Figure 5.19) are corrected. The solution that will be discussed in this section involves the definition of two drawbeads, one in the region where the wrinkles appear and another in the opposite side. This last one had to be introduced to avoid the appearance of wrinkles also on that region of the part.

The results presented in the previous sections indicate that the BBC 2005 criterion with Biax $= 0.9$ (see Figure 5.5) can describe the material behavior accurately. Nevertheless, it was decided to use this example also to analyse the possibility of defining the material behavior using the material generator in AutoForm®. The following section describes the procedure adopted to create the new material file.

5.5.3.1. Material Characterization

Volkswagen Autoeuropa® has at its disposal a Zwick/Roell® tensile testing machine. Therefore, it was decided to perform tensile tests at 0º, 45º and 90º with respect to the RD. The mean value of the results extracted from the three tests performed for each direction are shown in Table 5.8, where $R_{\mathrm{p0.2}}$ is the proof strength at 0.2% of the extensometer gauge length; R_{m} is the tensile strenght; A_{g} is the percentage of total elongation at maximum force; and A_{t} is the percentage of total elongation at fracture.

Table 5.8. Results from the tensile tests.

Angle	$R_{\mathrm{p0.2}}$ [MPa]	$R_{\boldsymbol{m}}$ [MPa]	A_{t} [%]	A_{g}[%]	r_{θ}
0º	150,98	297,65	43,97	24,55	1,89
45º	157,85	304,41	41,41	23,96	1,7
90º	156,56	296,27	43,28	23,86	2,23

The true stress-strain information from the tensile test performed with the specimen oriented along RD, was provided in a .bat file, as well as the R_{m} value, to define the hardening curve. These results were fitted by the Swift-Hockett/Sherby law and the resulting parameters are given in Table 5.9, which also shows the parameters available in the Volkswagen® group standard material library. The software automatically calculates an initial yield stress of $\sigma_0 = 152.6$ MPa from the experimental data. Using the 160.2 MPa from the library as the reference, it represents a variation of around 4.74 %, well below the ±20 MPa that is known to exist (Banabic, 2010). Figure 5.25 shows the two hardening

curves, highlighting that the difference between the curves increases for higher equivalent plastic strain values. Moreover, the observed difference for the strain corresponding to the onset of necking ($A_g = 24.55$ %) propagates to the extrapolation for higher strain values. Based on previous results, the part attains maximum equivalent plastic strain values of around 45 %. Therefore, based on Figure 5.25 it is expected to observe some differences in the predicted forming forces attained with the two material characterizations, with the parameters available in the Volkswagen® group standard material library leading to slightly higher values. This point is mentioned here to highlight, once again, the difficulties in reproducing accurately the alternative method plan.

Table 5.9. Swift-Hockett/Sherby material parameter obtained from the AutoForm® approximation.

Data	α	C [MPa]	ε_0	m	σ_{sat} [MPa]	σ_i [MPa]	a	p
Experimental	0.25	514.7	0.00479	0.224	483.9	159	3.49	0.716
Library	0.15	585	0.01	0.28	415	155	6.75	0.85

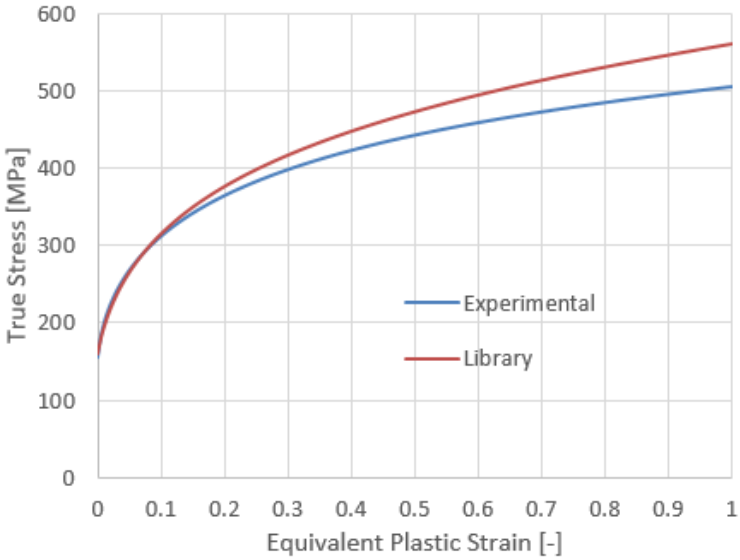

Figure 5.25. Comparison between the DX56D stress *vs*. equivalent plastic strain curves for the material library parameters (red) and the ones generates with tensile test results (blue).

The coefficients of anisotropy are compared in Table 5.10. Using the values from the standard material library as reference, the maximum variation is of approximately 21.43 % for r_{45}. This value slightly exceeds the 20 % which is the typical maximum deviation in literature (Banabic, 2010). The difference in the normalized yield curves for the Hill'48 yield

criterion are shown in Figure 5.26, highlighting the minor differences in the normalized principal stress space.

Table 5.10. Comparison between the values of the coefficients of anisotropy.

Data	r_0	r_{45}	r_{90}
Experimental	1.89	1.7	2.23
Library	1.7	1.4	2.1

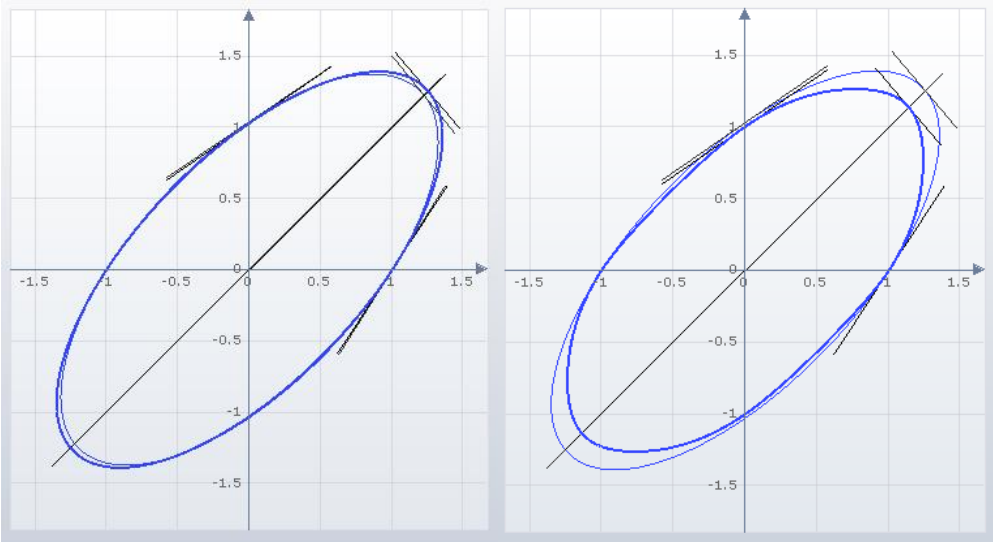

Figure 5.26. Left: Normalized Hill'48 yield curves for the material properties from the library (fine line) and from the tensile tests data (thick line). Right: Normalized yield curves obtained from tensile test data for Hill'48 (fine line) and Vegter 2017 (thick line).

The differences registered between the predicted values for other reference stress states using the experimental data and the one from the library (refer to Table 5.11 and Table 5.4, respectively) are significant. The anisotropy coefficients are known to affect the yield *locus*, but the Hill'48 criterion may not be flexible enough. In this context, it is possible to observe that the equibiaxial point is actually higher for the experimental material than for the one given in the standard material library (Figure 5.26 (left)). This gives reasoning for using a more advanced anisotropic yield criterion. From the summary presented in Table 3.1, the Vegter 2017 is chosen, because it can be defined using only the data provided by the uniaxial tensile tests. The output parameters obtained with the Vegter 2017 yield criterion are compared with the ones obtained by the Hill'48 yield criterion, identified with the same

experimental data, in Table 5.11. Moreover, the normalized yield curves are shown in Figure 5.26 (right). The comparison highlights the difference in the normalized equibiaxial stress value attained with both criteria. The value given by Vegter 2017 is equivalent to using a Biax $= 0.9083$ in the identification performed with Hill'48.

Table 5.11. Output parameter values of the Hill'48 and Vegter 2017 criteria based on the tensile test data.

Yield Criterion	σ_{45}/σ_0	σ_{90}/σ_0	σ_{ps0}/σ_0	σ_{ps90}/σ_0	σ_b/σ_0	σ_{shear}/σ_0	r_b
Hill'48	1.0764	1.0275	1.350	1.387	1.2507	0.554	0.848
Vegter 2017	1.0219	0.9999	1.238	1.260	1.136	0.533	0.848

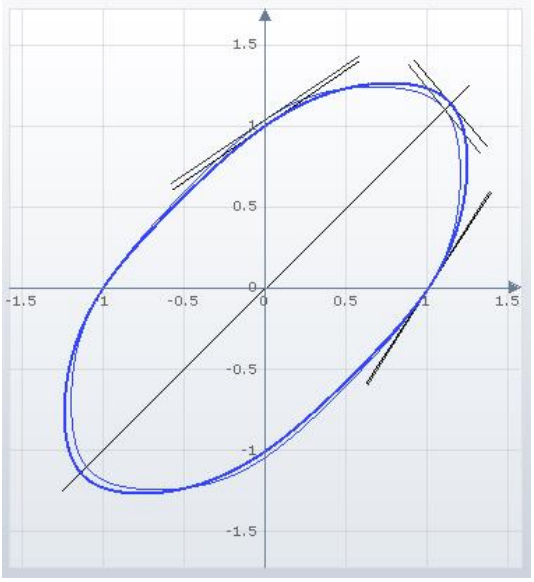

Figure 5.27. Normalized yield curves obtained from the material library data for BBC 2005 with Biax = 0.9 (fine line) and from the tensile tests for Vegter 2017 (thick line).

The draw-in results presented in previous sections indicate that the BBC 2005 criterion with Biax $= 0.9$ (see Figure 5.5) can describe the material behavior accurately. In this context, Figure 5.27 presents the normalized yield *locus* obtained with that yield criterion and with Vegter 2017. Although, some differences can be highlighted, especially in the equibiaxial and plane strain points, globally they are much smaller than the ones obtained when comparing with the Hill'48, either using the information of the standard material library, or based on the experimental results. The clear advantage is that the Vegter 2017 captures the behavior using the information from simple uniaxial tensile tests results.

The selection of the Biax for the BBC 2005 criterion requires performing a biaxial stress test or some inverse analysis procedure. Finally, the draw-in for the experimental try-out number two was compared with the results obtained using the Hill'48 from the standard material library and the Vegter 2017, as shown in Figure 5.28. Globally, the results show that the yield criteria have a minor influence in the draw-in results.

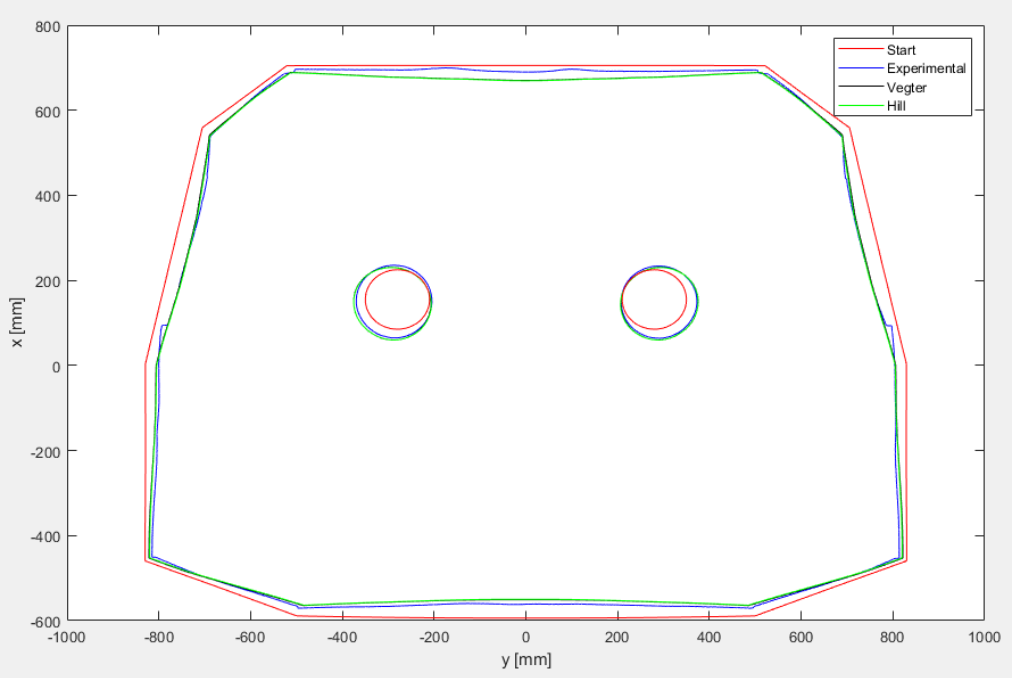

Figure 5.28. Draw-in comparison between the experimental try-out (blue) and the simulation results for Vegter 2017 (black) and Hill'48 based on the library data (green), in relation to the start of the drawing process (red), for try-out number two conditions.

5.5.3.2. Introduction of Two Supplementary Drawbeads

As previously mentioned, two supplementary drawbeads were introduced, one in the lower part and another in the upper, as can be seen in Figure 5.29. The definition of the drawbeads' geometry involved several virtual try-outs, but in this section, only the results corresponding to the final one will be discussed. The drawbeads' 3D profiles were created in AutoForm® in order to include their physical model (see section 2.3.1) in the tool's geometry. The supplementary lower drawbead creates an uplift force of 42 kN and a restraining force of 56 N/mm. The one introduced in the top region has an uplift force of 85 kN and a restraining force of 83 N/mm. Spring controlled tools are used to model the blankholders, with a cushion force of 1200 kN and all the cylinders' pressure set to 80 bar.

This translates to a total initial force of 640 kN and a final one of around 920 kN, which is similar to the one observed in the alternative kinematic method (see Figure 5.20), which lead to the wrinkling defect.

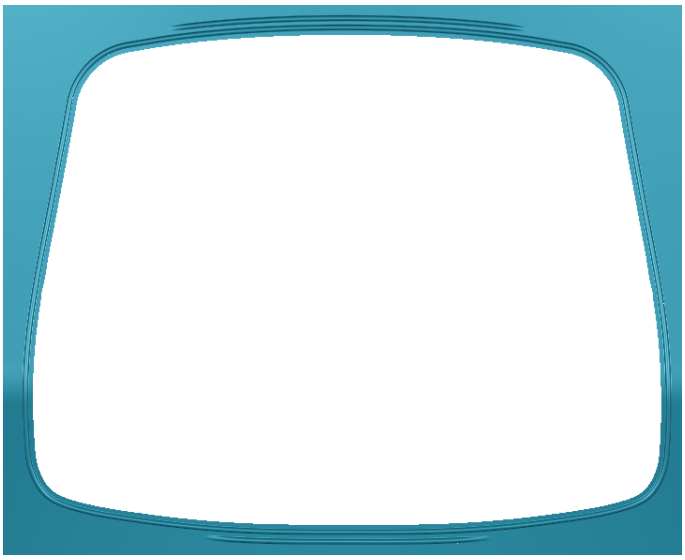

Figure 5.29. Additional drawbeads, in the lower and upper part of the upper blankholder.

The numerical simulations were performed considering three different approaches to model the material behavior: (i) Hill'48 yield criterion from the standard material library; (ii) Hill'48 and (iii) Vegter 2017, both with parameters identified using uniaxial tensile test results. For all three cases, the table of strain values of the FLC available in the standard material library (see Figure 5.2) was used to complete the .mat file

Figure 5.30 presents the formability results obtained with the Hill'48 yield criterion, defined with the material library information, showing that the part has good quality, comparable to the original method plan (see Figure 5.14). Figure 5.31 shows the formability results obtained with the Hill'48 yield criterion, identified using the uniaxial tensile tests results. Although the differences between the two identifications for the Hill'48 are marginal in the stress space (see Figure 5.26 (left)), there is some impact in the formability. For the Hill'48 identified using the uniaxial tensile tests results, the points on the right side of the FLC rise and are closer to the 20% safety margin of the non-linear FLC. Moreover, several regions of the part present insufficient stretch, which can also be related with the change made to the hardening law (see Figure 5.25). In fact, there is a difference in the maximum forces attained at the end of the forming process, showing a lower value for

the Hill'48 yield criterion, identified using the uniaxial tensile tests results. These results indicate that some problems can be prevented by investing in the experimental characterizing of the material, using simple tests.

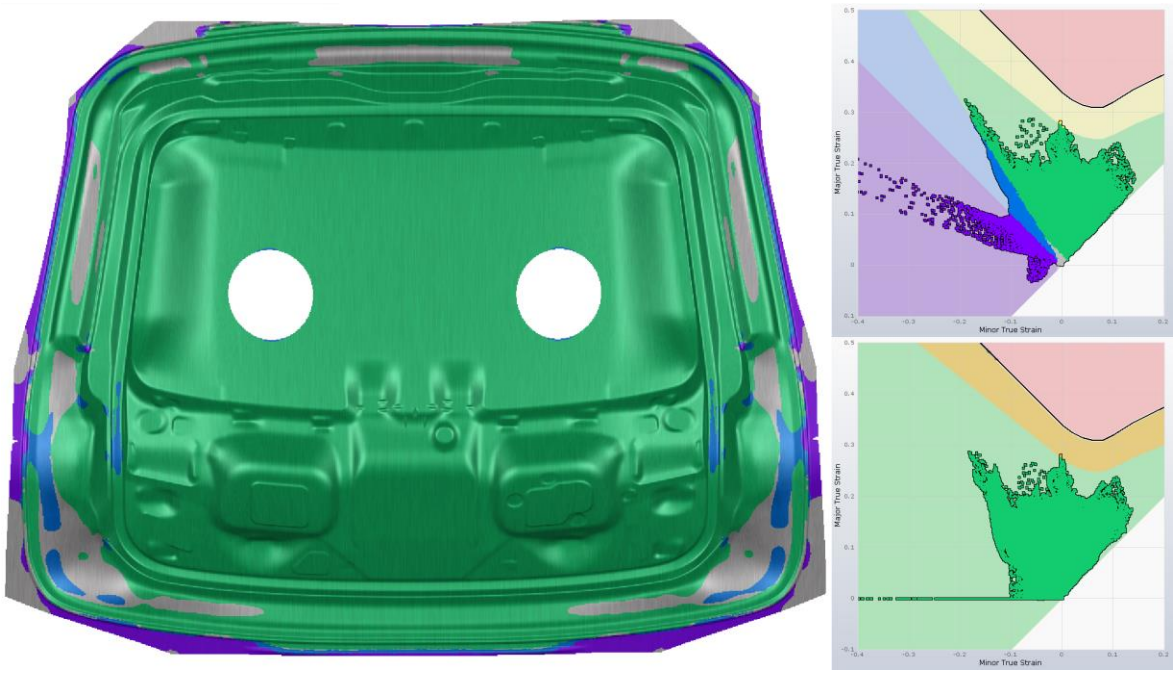

Figure 5.30. Forming results for the proposed solution using Hill'48 with the material library data. For the color code, refer to the caption of Figure 5.8.

The results obtained with the Vegter 2017 yield criterion are shown in Figure 5.32. In this case, there is a clear aggravation of zones for which the risk of splits is predicted, when compared to both the Hill'48 criterion results. Interestingly the zone for which insufficient stretch is predicted is reduced, when compared with the Hill'48 identified based on the uniaxial tensile test results. Interestingly, the maximum forces attained at the end of the forming process show the lowest value for the Vegter 2017, which indicates that the lower hardening behavior is compensated by the change in shape of the yield *locus*. Therefore, one can assume that the shape of the yield *locus* between the equibiaxial and the plane strain state (see Figure 5.26) also impacts this prediction. In any case, it should be mentioned that the wrinkling defect (see zone submitted to compression stress state in Figure 5.17) is always avoided. The previous results shown that the Vegter 2017 yield criterion seems to lead to a better description of the material orthotropic behavior. In this particular

case, the new method plan can be considered valid, if a safety margin of 10 % is chosen for the non-linear FLC, as shown in Figure 5.32.

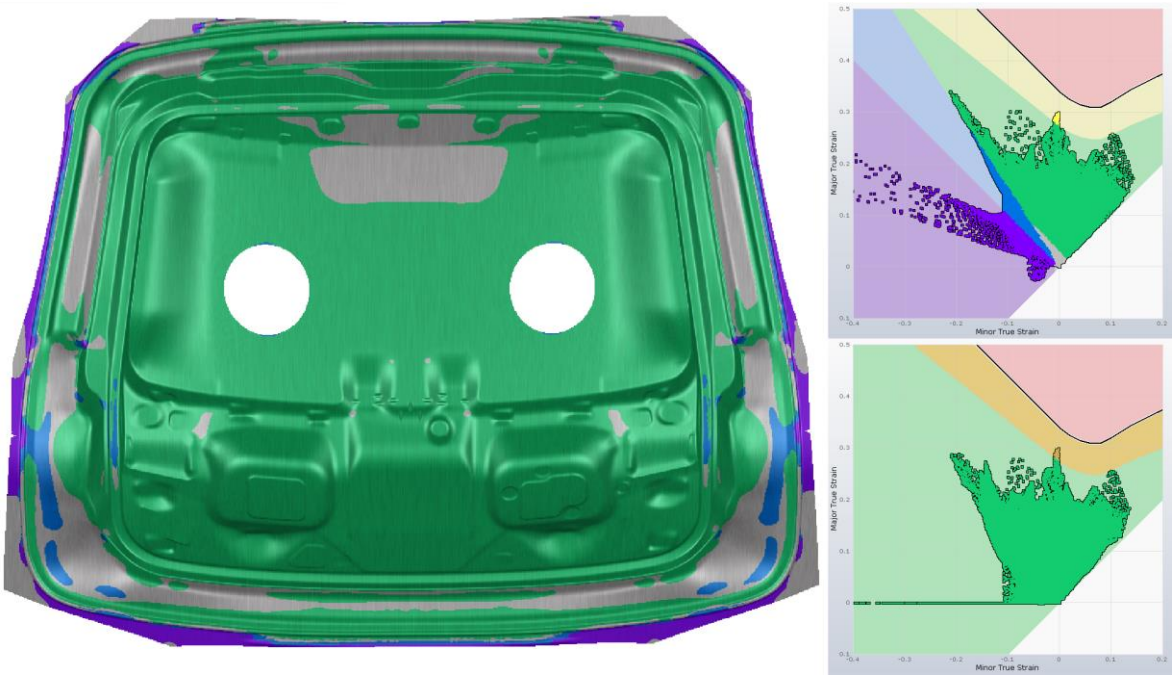

Figure 5.31. Forming results for the proposed solution using Hill'48 with parameters identified using uniaxial tensile test results. For the color code, refer to the caption of Figure 5.8.

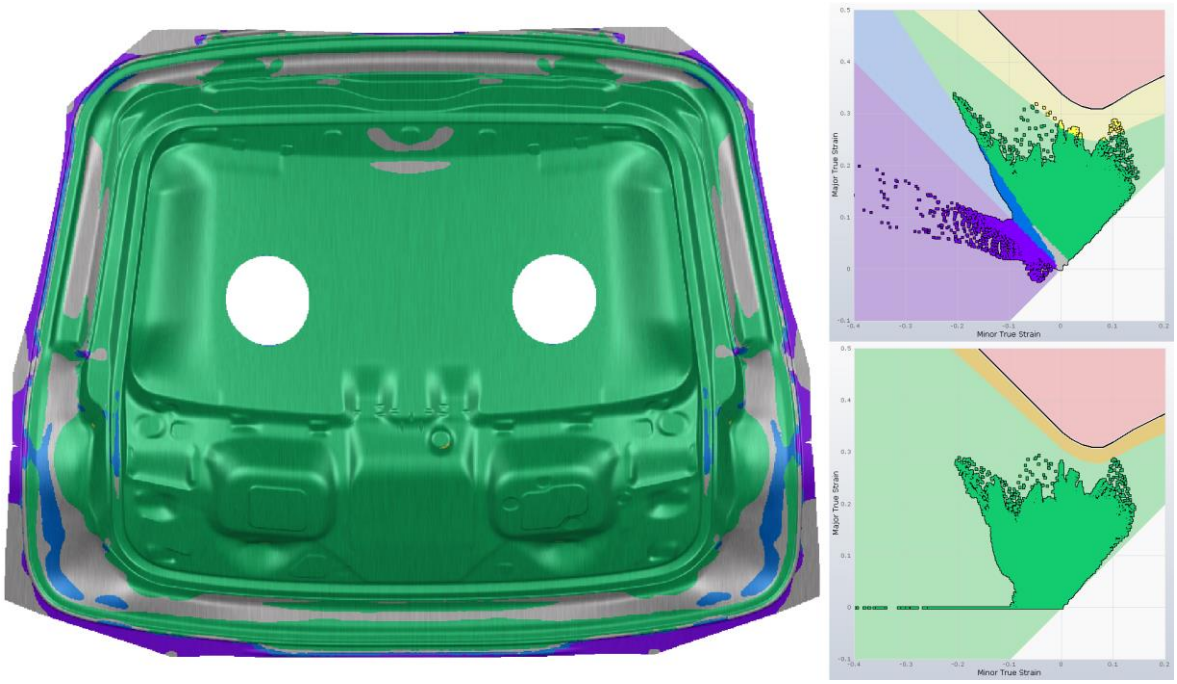

Figure 5.32. Forming results for the proposed solution using Vegter 2017 with parameters identified using uniaxial tensile test results. For the color code, refer to the caption of Figure 5.8.

Note that the formability results presented in this section were obtained with the single drawing process model. Although the two drawing processes can capture the pressure distribution and tilt of the tools (see Figure 5.18), the required repositioning alters the wrinkling prediction considerably. Figure 5.33 compares the distribution predicted for the wrinkling criterion in the critical wrinkling zone, obtained with the single (right) and the two drawing processes (left), at two instants, corresponding to the end of the upper cushion stroke (top) and the immediate step afterwards (bottom). As previously mentioned, the change of tools between the two drawing processes induces a drop in the force (see Figure 5.20), which generates an instability that will remain in the component. This aspect was detected in these final simulations by comparing the two models, as illustrated in Figure 5.33. Only for the two drawing processes model there is a clear and abrupt change in the wrinkling parameter at the time step, immediately after the end of the upper cushion stroke.

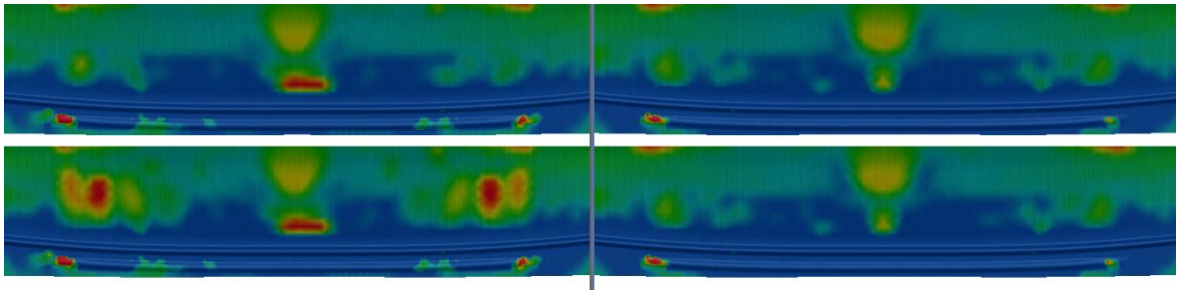

Figure 5.33. Distribution of the wrinkling criterion for the proposed solution using Vegter 2017 for the two drawing processes model (left) and the single one (right), at the end of the upper cushion stroke (above) and at the time step immediately after (below).

6. CONCLUSIONS AND FUTURE WORK

Sheet metal forming is a complex process with several process parameters that influence the different boundary conditions imposed to the blank sheet. Therefore, in order to assure accurate numerical simulation results, it is fundamental that the inputs and premises considered in the model approximate well the physical model. Otherwise, it will translate to the unviable detection of possible defects. Besides process parameters, the influence of the description of the plastic behavior of the material was studied and its impact on the results of drawing processes analyzed. The main conclusions and recommendations for future work are summarized in this chapter.

6.1. Conclusions

The formability analysis performed for case studies A and B showed the impact of the equibiaxial stress value in the prediction of potential splits. The study considered a 10 % variation of the Biax parameter, also highlighting its impact on the plane strain and shear stress states. Globally, the formability prediction is more conservative when using the Hill'48 yield criterion, when compared with the BBC 2005. For the case study A, the variation induced in the plane strain state, caused by a Biax $= 0.9$, leads to the change of the location of the critical region to the one that is more prone to be observed in experimental tests.

The advantage of the non-linear FLC was attested as a mean to validate designs which involve complex strain paths. For case study B, the non-linear FLC points out the critical zone, typically observed for inner liftgates, which the linear FLC does not capture. Also, it reveals that the region in the linear FLC that surpasses the safety margin has in fact remaining formability. It is clear from case studies A and B that non-linear strain paths that occur on the right side of the FLC need to be given special attention. There is a high probability that the points situated in this region show a higher exhausted formability than the one presented in the linear FLC.

For case study C, the usage of the columns model enabled the detection of tilt for the tools, which compromises the desired uniform pressure distribution on the pressure

ring and, consequentially, on the part. This tilt can only be solved by altering the working surfaces' orientation, which at the production phase would entail the manufacture of completely new tools. It seems that the process was designed with a single-action press in mind, since it becomes a perfect solution when cylinders apply force to a blankholder that acts directly against a rigid die. An alternative to work around this problem was proposed: the two drawing processes model, which enabled the use of columns to control the force. Although this model captures the pressure distribution correctly, the adjustment of the tools between the two fictitious processes induces wrinkles. Therefore, the application of the two drawing processes model is considered to be a good strategy for possible adjustments in the design phase, but not to perform the validation. Furthermore, the columns model works against a rigid tool, which means that the pressure values that it presents are not as reliable as the ones with a defined tool stiffness. Albeit the tool forces do not vary significantly, it is not an ideal solution to the problem. The spring controlled tool seems to be a better approximation to the physical model, since it is the only option that captures the possible opening of the tools. Force controlled tools albeit useful should only be used in an initial estimate of the necessary binder force.

The spacers model was also tested but proved to be difficult to apply. The spacer's stiffness value is very unpredictable and it is very time consuming to uncover with precision, even when considering no thickness increment, which is the other control parameter.

6.2. Future Work

The AutoForm® forming solver is optimized to work under ideal kinematic conditions. This limited the analysis of case study C since the production kinematic conditions could not be simulated.

Ideally, the software should be able to predict, during the drawing process, which of the two blankholders should displace. A drastic reduction of the time step when the blankholder forces become close to each other would probably be needed. Also, the columns model should be implemented in such a way that it could work against non-rigid tools, even if their stiffness is high. This would allow its use when modeling triple-action presses in a single drawing process.

The characterization of the mechanical behavior with tensile tests in the 0º, 45º and 90º with respect to RD is recommended, since it provides valuable information concerning the standard material model available. The material generator is a practical and easy tool to be used, enabling the creation of new material file contributing to a more accurate library. The Vegter 2017 yield criterion is also recommended as long as convexity is guaranteed. If that is not the case, an approximation with the BBC 2005 is also an option, which requires the knowledge of the equibiaxial stress value. Finally, it would be interesting to have a proper comparison of the yield surfaces in a space corresponding to the plane stress components.

BIBLIOGRAPHY

A. Ofenheimer, D. Kitting, M. Koplenig, H. Grass, W. Volk, A. and Lipp, R. Illig, H. K. (2008) 'Cost effective strategy to predict formability in two-step sheet forming operations', *Numisheet*. ., pp. 265–269. Available at: https://graz.pure.elsevier.com/en/publications/cost-effective-strategy-to-predict-formability-in-two-step-sheet- (Accessed: 14 May 2020).

Abspoel, M. *et al.* (2017) *A new method for predicting advanced yield criteria input parameters from mechanical properties*, *Journal of Materials Processing Technology*. Elsevier Ltd. doi: 10.1016/j.jmatprotec.2017.05.006.

An, Y. *et al.* (2011) 'A novel yield locus description by combining the Taylor and the relaxed Taylor theory for sheet steels', *International Journal of Plasticity*, 27(11), pp. 1758–1780. doi: 10.1016/j.ijplas.2011.05.003.

AutoForm® R8 software manual (2018).

Banabic, D. (2010) *Sheet Metal Forming Processes*, *Springer-Verlag Berlin Heidelberg*. Berlin, Heidelberg: Springer Berlin Heidelberg. doi: 10.1007/978-3-540-88113-1.

Belytschko, T. *et al.* (2014) *Nonlinear Finite Elements for Continua and Structures Second Edition*. doi: 10.1088/1751-8113/44/8/085201.

Cormen, T. H. *et al.* (2009) *Introduction to Algorithms, Third Edition*. 3rd edn. Massachusetts Institute of Technology.

FIBRO® Standard Parts Catalog (2014).

Hill, R. (1948) 'A theory of the yielding and plastic flow of anisotropic metals', *Proceedings of the Royal Society of London. Series A. Mathematical and Physical Sciences*. The Royal Society, 193(1033), pp. 281–297. doi: 10.1098/rspa.1948.0045.

ten Horn, C. H. L. J., Vegter, H. and Mouatassim, M. El (2005) 'Increased accuracy in forming simulation of complex Renault part through Corus-Vegter material model', in Oñate, E. and Owen, D. R. J. (eds) *VIII International Conference on Computational Plasticity COMPLAS VIII*, p. 4.

Jocham, D. *et al.* (2015) 'Prediction of fromability for multi-linear strain paths', (JUNE). Available at:

https://www.researchgate.net/publication/283497054_Prediction_of_formability_for_multi-linear_strain_paths (Accessed: 17 May 2020).
Jocham, D. *et al.* (2017) 'Experimental prediction of sheet metal formability of AW-5754 for non-linear strain paths by using a cruciform specimen and a blank holder with adjustable draw beads on a sheet metal testing machine', *International Journal of Material Forming*. International Journal of Material Forming, 10(4), pp. 597–605. doi: 10.1007/s12289-016-1304-9.
Katili, I. (1993) 'A new discrete Kirchhoff-Mindlin element based on Mindlin-Reissner plate theory and assumed shear strain fields—part I: An extended DKT element for thick-plate bending analysis', *International Journal for Numerical Methods in Engineering*. John Wiley & Sons, Ltd, 36(11), pp. 1859–1883. doi: 10.1002/nme.1620361106.
Kubli, W. (1995) 'Prozessoptimierte implizite FEM-Formulierung für die Umformsimulation grossflächiger Blechbauteile'. ETH Zürich. doi: 10.3929/ethz-a-001503805.
MathWorks® (2014) *Matlab's boundary function*. Available at: https://www.mathworks.com/help/matlab/ref/boundary.html (Accessed: 28 October 2020).
Smith, D. (1990) *Die Design Handbook*. 3rd edn. Society of Manufacturing Engineers. Available at: https://books.google.pt/books?id=JDd61NujspYC&printsec=frontcover&hl=pt-PT&source=gbs_ge_summary_r&cad=0#v=onepage&q&f=false (Accessed: 25 October 2020).
Tang, S. C. and Pan, J. (2007) *Mechanics Modeling of Sheet Metal Forming*. SAE International. Available at: https://www.sae.org/publications/books/content/r-321/ (Accessed: 3 October 2020).
Teixeira-Dias, F. *et al.* (2018) *Método dos Elementos Finitos - Técnicas de Simulação Numérica em Engenharia*. 2ª edição, *ETEP - Edições Técnicas e Profissionais*. 2ª edição. Available at: https://www.lidel.pt/pt/catalogo/engenharia-ciencias-da-terra/mecanica/metodo-dos-elementos-finitos-2/.
Vegter, H. and Van Den Boogaard, A. H. (2006) 'A plane stress yield function for anisotropic sheet material by interpolation of biaxial stress states', *International Journal of Plasticity*. Pergamon, 22(3), pp. 557–580. doi: 10.1016/j.ijplas.2005.04.009.
Vegter, H., ten Horn, C. and Abspoel, M. (2009) 'The Corus-Vegter Lite material model:

Simplifying advanced material modelling', *International Journal of Material Forming*, 2(SUPPL. 1), pp. 511–514. doi: 10.1007/s12289-009-0640-4.

Volk, W. *et al.* (2012) 'Failure prediction for nonlinear strain paths in sheet metal forming', *CIRP Annals - Manufacturing Technology*, 61(1), pp. 259–262. doi: 10.1016/j.cirp.2012.03.111.

Volk, W. *et al.* (2013) 'Phenomelogical and Numerical Description of Localised Necking using Generalised Forming Limit Concept', *Proceedings of the IDDRG Conference*, pp. 1–7. Available at: https://www.researchgate.net/publication/279757322_Phenomenological_and_numerical_description_of_localized_necking_using_generalized_forming_limit_concept.

Volk, W. *et al.* (2019) 'Models and modelling for process limits in metal forming', *CIRP Annals*. CIRP, 68(2), pp. 775–798. doi: 10.1016/j.cirp.2019.05.007.

Volk, W. and Gaber, C. (2017) 'Investigation and Compensation of Biaxial Pre-strain during the Standard Nakajima- and Marciniak-test Using Generalized Forming Limit Concept', *Procedia Engineering*. Elsevier B.V., 207, pp. 568–573. doi: 10.1016/j.proeng.2017.10.1022.

Volk, W. and Hora, P. (2011) 'New algorithm for a robust user-independent evaluation of beginning instability for the experimental FLC determination', *International Journal of Material Forming*. Springer, 4(3), pp. 339–346. doi: 10.1007/s12289-010-1012-9.

Volk, W. and Suh, J. (2014) 'Prediction of formability for non-linear deformation history using generalized forming limit concept (GFLC)', in. AIP, pp. 556–561. doi: 10.1063/1.4850035.

Wessel, A. *et al.* (2020) 'Effect of different anisotropic 3D yield functions on a roller hemming simulation', in *Procedia Manufacturing*. Elsevier B.V., pp. 1358–1365. doi: 10.1016/j.promfg.2020.04.264.

Wick, C., Benedict, J. T. and Veilleux, R. F. (eds) (1984) *Tool and Manufacturing Engineers Handbook Volume 2: Forming*. 4th edn. Society of Manufacturing Engineers. Available at: https://www.amazon.com/Tool-Manufacturing-Engineers-Handbook-Vol/dp/0872631354 (Accessed: 25 October 2020).

Zienkiewicz, O. C. and Taylor, R. L. (2000) *The Finite Element Method, Volume 2: Solid Mechanic*. 5th Editio. Butterworth-Heinemann.

Zienkiewicz, O., Taylor, R. and Zhu, J. Z. (2013) *The Finite Element Method: its Basis*

and Fundamentals: Seventh Edition, Butterworth-Heinemann. Elsevier Ltd. doi: 10.1016/C2009-0-24909-9.

ANNEX A: PLATE ELEMENT

Katili (1993) developed a C^0 continuous plate bending element whose formulation, based on the Reissner-Mindlin theory, introduces a generalization of the discrete Kirchhoff technique to include the effects of shear deformation through-the-thickness (transverse shear). The Reissner-Mindlin theory considers that the normal to the mid plane remains straight after deformation, but does not necessarily remain normal to that mid plane. The rotation of the normal is also considered independent of the deflection that happens to the mid plane. The in-plane displacements u, v and out of plane, w, are defined as:

$$u = z\vartheta_x(x,y), v = z\vartheta_y(x,y), w = w(x,y), \tag{A.1}$$

where ϑ corresponds to the rotation degree of freedom, considering the coordinate system shown in Figure A.1. The coordinate z is $-0.5h \leq z \leq 0.5h$, with h being the element thickness.

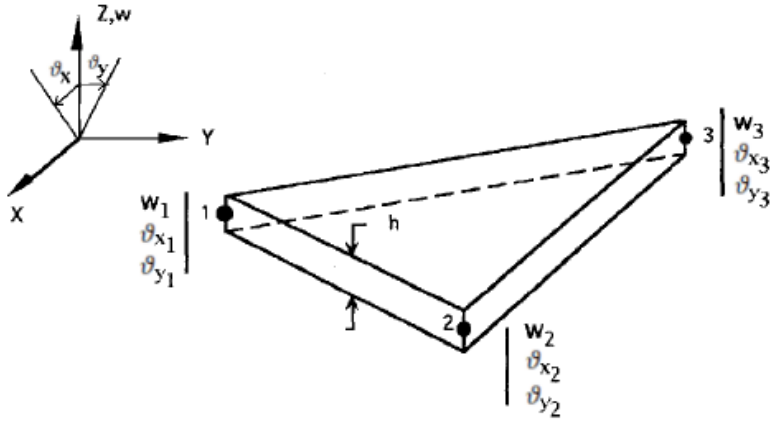

Figure A.1. Degrees of freedom and coordinate system of the plate bending element (altered) (Katili, 1993).

The equilibrium equations for a static distributed load f_z are as follows:

$$\begin{aligned} T_{x,x} + T_{y,y} + f_z &= 0, \\ M_{x,x} + M_{xy,y} - T_x &= 0, \\ M_{xy,x} + M_{y,y} - T_y &= 0, \end{aligned} \tag{A.2}$$

where the comma in the subscript is used to represent the derivative. T_x, T_y, M_x, M_y and M_{xy} are the shear forces and the bending moments per unit length, as shown in Figure A.2. These can be related with the stress components by:

$$T_x = \int_{-\frac{1}{2}h}^{\frac{1}{2}h} \sigma_{xz} dz \, , T_y = \int_{-\frac{1}{2}h}^{\frac{1}{2}h} \sigma_{yz} dz,$$
$$M_x = \int_{-\frac{1}{2}h}^{\frac{1}{2}h} \sigma_{xx} z dz \, , M_y = \int_{-\frac{1}{2}h}^{\frac{1}{2}h} \sigma_{yy} z dz \, , M_{xy} = \int_{-\frac{1}{2}h}^{\frac{1}{2}h} \sigma_{xy} z dz \, . \tag{A.3}$$

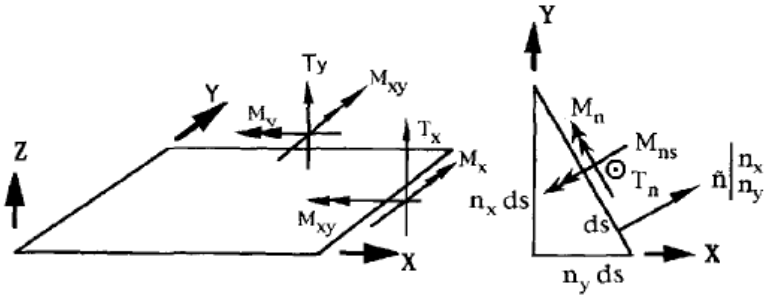

Figure A.2. Bending moments and shear force**s** (Katili, 1993)**.**

Assuming the sign convention of Figure A.2, the kinematic relationships are:

$$\boldsymbol{\chi} = \begin{Bmatrix} \vartheta_{x,x} \\ \vartheta_{y,y} \\ \vartheta_{x,y} + \vartheta_{y,x} \end{Bmatrix},$$
$$\boldsymbol{\Upsilon} = \begin{Bmatrix} \Upsilon_{xz} \\ \Upsilon_{yz} \end{Bmatrix} = \begin{Bmatrix} w_{,x} + \vartheta_x \\ w_{,y} + \vartheta_y \end{Bmatrix}, \tag{A.4}$$

where $\boldsymbol{\chi}$ is the curvature vector and $\boldsymbol{\Upsilon}$ the transverse shear strains. They are related to the bending moments and shear forces by the constitutive relations $\boldsymbol{H_b}$ and $\boldsymbol{H_s}$, respectively. These relations depend on the behavior of the material, whether isotropic or anisotropic, and its current state, whether elastic or plastic.

$$\begin{Bmatrix} M_x \\ M_y \\ M_{xy} \end{Bmatrix} = \boldsymbol{H_b} \begin{Bmatrix} \vartheta_{x,x} \\ \vartheta_{y,y} \\ \vartheta_{x,y} + \vartheta_{y,x} \end{Bmatrix},$$
$$\begin{Bmatrix} T_x \\ T_y \end{Bmatrix} = \boldsymbol{H_s} \begin{Bmatrix} \bar{\Upsilon}_{xz} \\ \bar{\Upsilon}_{yz} \end{Bmatrix}. \tag{A.5}$$

$\bar{Y}$ refers to an assumed value of transverse shear strain. For illustration purposes consider a linearly elastic, isotropic, homogeneous plate, where $\boldsymbol{H}_{\mathbf{b}}$ and $\boldsymbol{H}_{\mathbf{s}}$ are given by:

$$\boldsymbol{H}_{\mathbf{b}} = \frac{Eh^3}{12(1-\upsilon^2)}\begin{bmatrix} 1 & \upsilon & 0 \\ \upsilon & 1 & 0 \\ 0 & 0 & \frac{1}{2}(1-\upsilon) \end{bmatrix}, \qquad \boldsymbol{H}_{\mathbf{s}} = \frac{\kappa Eh}{2(1+\upsilon)}\begin{bmatrix} 1 & 0 \\ 0 & 1 \end{bmatrix}, \tag{A.6}$$

with υ being the Poisson ratio, E the Young modulus and κ the shear correction factor. The strain field presented in equation (2.9) is not enough to reproduce the kinematic behavior of the element completely, namely the rotations. Thus, the rotations are interpolated by a complete rigid body and constant-curvature field expansion, using N_i with $i = 1, 2, 3$, and a set of higher order functions P_k with $k = 4, 5, 6$, defined for the mid-points of the element's segments (see Figure A.3). This results in the following rotation fields:

$$\vartheta_x = \sum_{i=1}^{3} N_i\, \vartheta_{xi} + \sum_{k=4}^{6} P_k\, C_k \Delta\vartheta_{sk}, \qquad \vartheta_y = \sum_{i=1}^{3} N_i\, \vartheta_{yi} + \sum_{k=4}^{6} P_k\, S_k \Delta\vartheta_{sk}, \tag{A.7}$$

where $C_k \equiv \cos(\theta_k)$ and $S_k \equiv \sin(\theta_k)$. Assuming, $N_1 = \lambda$, $N_2 = \xi$ and $N_3 = \eta$, and the higher order functions defined as:

$$P_4 = 4\lambda\xi, P_5 = 4\xi\eta, P_6 = 4\lambda\eta, \tag{A.8}$$

the curvature vector can be given by:

$$\boldsymbol{\chi} = \boldsymbol{B}_{\mathbf{b}\vartheta}\boldsymbol{U}_{\boldsymbol{n}} + \boldsymbol{B}_{\mathbf{b}\Delta\vartheta}\Delta\boldsymbol{\vartheta}_{\boldsymbol{n}}, \tag{A.9}$$

with $\boldsymbol{B}_{\mathbf{b}\vartheta}$ originating from equation (2.9), where zero columns are introduced for adjustment:

$$\boldsymbol{B}_{\mathbf{b}\vartheta} = \frac{1}{2A^{\mathrm{e}}}\begin{bmatrix} 0 & \beta_1 & 0 & 0 & \beta_2 & 0 & 0 & \beta_3 & 0 \\ 0 & 0 & \gamma_1 & 0 & 0 & \gamma_2 & 0 & 0 & \gamma_3 \\ 0 & \gamma_1 & \beta_1 & 0 & \gamma_2 & \beta_2 & 0 & \gamma_3 & \beta_3 \end{bmatrix}. \tag{A.10}$$

A similar procedure to obtain the matrix $\boldsymbol{B}_{\mathbf{b}\Delta\vartheta}$ should be applied, differentiating the functions P_k, leading to:

$$\boldsymbol{B}_{\mathbf{b}\Delta\boldsymbol{\vartheta}} = \frac{1}{2A^{\mathrm{e}}}\begin{bmatrix} \left(P_{k,\xi}\,\beta_2 + P_{k,\eta}\,\beta_3\right)C_k \\ \left(P_{k,\xi}\,\gamma_2 + P_{k,\eta}\,\gamma_3\right)S_k \\ \left(P_{k,\xi}\,\gamma_2 + P_{k,\eta}\,\gamma_3\right)C_k + \left(P_{k,\xi}\,\beta_2 + P_{k,\eta}\,\beta_3\right)S_k \end{bmatrix}. \tag{A.11}$$

Note that the vector of nodal degrees of freedom is $\boldsymbol{U_n} = \{w_1 \quad \vartheta_{x1} \quad \vartheta_{y1} \quad w_2 \quad \vartheta_{x2} \quad \vartheta_{y2} \quad w_3 \quad \vartheta_{x3} \quad \vartheta_{y3}\}$ and the difference between the quadratic and linear rotation at the segments mid-point is $\Delta\boldsymbol{\vartheta_n} = \{\Delta\vartheta_{s4} \quad \Delta\vartheta_{s5} \quad \Delta\vartheta_{s6}\}$.

To define the shear strain fields, the relation between the bending and shear rotations must be found. Consider a local s, n coordinate system at the element boundary, where s and n denote the tangential and outward normal directions respectively, like represented in Figure A.3.

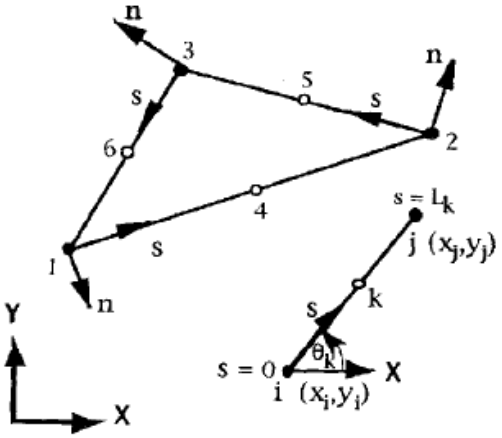

Figure A.3. Representation of the tangential and outward normal coordinate system (Katili, 1993).

The length of the segments is L_k, with $k = 4, 5, 6$. The assumed tangential shear strain can be given by:

$$\bar{Y}_{sz} = \frac{T_s}{D_s}, \tag{A.12}$$

with T_s being the tangential shear force along the side k, such that:

$$T_s = M_{s,s} + M_{ns,n}. \tag{A.13}$$

Considering the constitutive equations for the bending moments, $D_{\mathrm{s}} = (\kappa Eh/2(1+\upsilon))$ and $D_{\mathrm{b}} = (Eh^3/12(1-\upsilon^2))$. This allows defining:

$$M_s = D_{\mathrm{b}}\left(\vartheta_{s,s} + \upsilon\vartheta_{n,n}\right), \tag{A.14}$$

$$M_{ns} = D_{\mathrm{b}} \frac{(1-\upsilon)}{2} \left(\vartheta_{s,n} + \vartheta_{n,s}\right),$$

which give:

$$\bar{Y}_{sz} = \frac{D_{\mathrm{b}}}{D_{\mathrm{s}}} \left[\vartheta_{s,ss} + \upsilon \vartheta_{n,ns} + \frac{(1-\upsilon)}{2} \left(\vartheta_{s,nn} + \vartheta_{n,ns}\right)\right]. \tag{A.15}$$

By imposing, along the sides of the element, a linear and quadratic variation of the rotations ϑ_n and ϑ_s, respectively, such that:

$$\begin{aligned} \vartheta_n &= \left(1 - \frac{s}{L_k}\right) \vartheta_{ni} + \frac{s}{L_k} \vartheta_{nj}, \\ \vartheta_s &= \left(1 - \frac{s}{L_k}\right) \vartheta_{si} + \frac{s}{L_k} \vartheta_{sj} + 4 \frac{s}{L_k} \left(1 - \frac{s}{L_k}\right) \Delta\vartheta_{sk}, \end{aligned} \tag{A.16)}$$

makes $\vartheta_{n,ns} = \vartheta_{s,nn} = 0$, and so:

$$\bar{Y}_{sz} = \frac{D_{\mathrm{b}}}{D_{\mathrm{s}}} \vartheta_{s,ss} = -\frac{2}{3} \phi_k \Delta\vartheta_{sk}. \tag{A.17}$$

This gives the shear influence factor ϕ_k as:

$$\phi_k = \frac{12}{L_k^2} \frac{D_{\mathrm{b}}}{D_{\mathrm{s}}}. \tag{A.18}$$

The assumed shear angle components of the nodes can be determined based on the assumed tangential shear angles of the sides, such that

$$\begin{Bmatrix} \bar{Y}_{xz1} \\ \bar{Y}_{yz1} \\ \bar{Y}_{xz2} \\ \bar{Y}_{yz2} \\ \bar{Y}_{xz3} \\ \bar{Y}_{yz3} \end{Bmatrix} = \begin{bmatrix} S_6/A_1 & 0 & -S_4/A_1 \\ -C_6/A_1 & 0 & C_4/A_1 \\ -S_5/A_2 & S_4/A_2 & 0 \\ C_5/A_2 & -C_4/A_2 & 0 \\ 0 & -S_6/A_3 & S_5/A_3 \\ 0 & C_6/A_3 & -C_5/A_3 \end{bmatrix} \begin{Bmatrix} \bar{Y}_{sz4} \\ \bar{Y}_{sz5} \\ \bar{Y}_{sz6} \end{Bmatrix}, \tag{A.19}$$

where $A_1 = C_4 S_6 - C_6 S_4$, $A_2 = C_5 S_4 - C_4 S_5$ and $A_3 = C_6 S_5 - C_5 S_6$. This means that the assumed transverse shear can be interpolated with:

$$\begin{Bmatrix} \bar{Y}_{xz} \\ \bar{Y}_{yz} \end{Bmatrix} = \sum_{i=1}^{3} \boldsymbol{N_i} \begin{Bmatrix} \bar{Y}_{xzi} \\ \bar{Y}_{yzi} \end{Bmatrix} = \boldsymbol{N_Y} \begin{Bmatrix} \bar{Y}_{sz4} \\ \bar{Y}_{sz5} \\ \bar{Y}_{sz6} \end{Bmatrix}, \tag{A.20}$$

where

$$\boldsymbol{N_Y} = \begin{bmatrix} \left(\frac{S_6}{A_1}\lambda - \frac{S_5}{A_2}\xi\right) & \left(\frac{S_4}{A_2}\xi - \frac{S_6}{A_3}\eta\right) & \left(\frac{S_5}{A_3}\eta - \frac{S_4}{A_1}\lambda\right) \\ \left(\frac{C_5}{A_2}\xi - \frac{C_6}{A_1}\lambda\right) & \left(\frac{C_6}{A_3}\eta - \frac{C_4}{A_2}\xi\right) & \left(\frac{C_4}{A_1}\lambda - \frac{C_5}{A_3}\eta\right) \end{bmatrix}. \tag{A.21}$$

From equation (A.17) the following relation is obtained:

$$\begin{Bmatrix} \bar{Y}_{xz} \\ \bar{Y}_{yz} \end{Bmatrix} = \boldsymbol{B_{s\Delta\vartheta}}\Delta\boldsymbol{\vartheta_n}, \tag{A.22}$$

where $\boldsymbol{B_{s\Delta\vartheta}} = -(2/3)\boldsymbol{N_Y}\boldsymbol{\phi_k}$, which translates to:

$$\boldsymbol{B_{s\Delta\vartheta}} = \frac{2}{3}\begin{bmatrix} \left(\frac{S_5}{A_2}\xi - \frac{S_6}{A_1}\lambda\right)\phi_4 & \left(\frac{S_6}{A_3}\eta - \frac{S_4}{A_2}\xi\right)\phi_5 & \left(\frac{S_4}{A_1}\lambda - \frac{S_5}{A_3}\eta\right)\phi_6 \\ \left(\frac{C_6}{A_1}\lambda - \frac{C_5}{A_2}\xi\right)\phi_4 & \left(\frac{C_4}{A_2}\xi - \frac{C_6}{A_3}\eta\right)\phi_5 & \left(\frac{C_5}{A_3}\eta - \frac{C_4}{A_1}\lambda\right)\phi_6 \end{bmatrix}. \tag{A.23}$$

Using the variational functional of the modified Hu-Washizu principal, which gives the total strain energy as:

$$\Pi = \Pi_{\mathrm{b}} + \Pi_{\mathrm{s}} - \int_{A^{\mathrm{e}}} f_z w \, dA + \Pi_{\mathrm{ext}}, \tag{A.24}$$

with

$$\Pi_{\mathrm{b}} = \frac{1}{2}\int_{A^{\mathrm{e}}} \boldsymbol{\chi}^{\mathrm{T}}\boldsymbol{H_{\mathrm{b}}}\boldsymbol{\chi}\, dA, \tag{A.25}$$

$$\Pi_{\mathrm{s}} = \frac{1}{2}\int_{A^{\mathrm{e}}} \bar{\boldsymbol{Y}}^{\mathrm{T}}\boldsymbol{H_{\mathrm{s}}}\bar{\boldsymbol{Y}}dA + \int_{A^{\mathrm{e}}} \boldsymbol{T}(\boldsymbol{Y} - \bar{\boldsymbol{Y}})dA, \tag{A.26}$$

where Π_{b}, Π_{s} and Π_{ext} are the strain energies corresponding to bending, shear and the external forces respectively. f_z is the distributed load in the z direction. Considering the variation of the strain energy associated with the transverse shear vector, $\boldsymbol{T}$, equal to zero, the following constraint equation can be written:

$$\int_0^{L_k} \delta T_s(Y_{sz} - \bar{Y}_{sz})\,\mathrm{ds} = 0, \tag{A.27}$$

with T_s constant per side:

$$\int_0^{L_k} (Y_{sz} - \bar{Y}_{sz})\,\mathrm{ds} = 0, \tag{A.28}$$

recalling equation (A.16)) and knowing that $Y_{sz} = w_{,s} + \vartheta_s$ gives, after integration:

$$w_j - w_i + \frac{L_k}{2}\vartheta_{si} + \frac{L_k}{2}\vartheta_{sj} + \frac{2}{3}L_k\Delta\vartheta_{sk} - L_k\bar{Y}_{sz} = 0. \tag{A.29}$$

Thus, the rotations for the distinct coordinate axis can be obtained from one another:

$$\begin{Bmatrix}\vartheta_s\\ \vartheta_n\end{Bmatrix}_{i,j} = \begin{bmatrix}C_k & S_k\\ -S_k & C_k\end{bmatrix}\begin{Bmatrix}\vartheta_x\\ \vartheta_y\end{Bmatrix}_{i,j}, \tag{A.30}$$

which leads to

$$\frac{2}{3}L_k(1+\boldsymbol{\phi_k})\Delta\vartheta_{sk} = w_i - w_j - \frac{L_k}{2}\left(C_k\vartheta_{xi} + S_k\vartheta_{yi}\right) - \frac{L_k}{2}\left(C_k\vartheta_{xj} + S_k\vartheta_{yj}\right), \tag{A.31}$$

which can be written in the form:

$$\boldsymbol{A_{\Delta\vartheta}\Delta\vartheta_{sk}} = \boldsymbol{A_{\mathrm{w}}U_n}, \tag{A.32}$$

where

$$\boldsymbol{A_{\Delta\vartheta}} = \begin{bmatrix}\frac{2}{3}L_4(1+\phi_4) & 0 & 0\\ 0 & \frac{2}{3}L_5(1+\phi_5) & 0\\ 0 & 0 & \frac{2}{3}L_6(1+\phi_6)\end{bmatrix}, \tag{A.33}$$

and, noting that $L_kC_k = \left(x_j - x_i\right)$ and $L_kS_k = \left(y_j - y_i\right)$:

$$\boldsymbol{A_{\mathrm{w}}} = \begin{bmatrix}1 & \frac{-\gamma_3}{2} & \frac{\beta_3}{2} & -1 & \frac{-\gamma_3}{2} & \frac{\beta_3}{2} & 0 & 0 & 0\\ 0 & 0 & 0 & 1 & \frac{-\gamma_1}{2} & \frac{\beta_1}{2} & -1 & \frac{-\gamma_1}{2} & \frac{\beta_1}{2}\\ -1 & \frac{-\gamma_2}{2} & \frac{\beta_2}{2} & 0 & 0 & 0 & 1 & \frac{-\gamma_2}{2} & \frac{\beta_2}{2}\end{bmatrix}. \tag{A.34}$$

Making $\boldsymbol{A_{\mathrm{n}}} = \boldsymbol{A_{\Delta\vartheta}^{-1}A_{\mathrm{w}}}$ changes equation (A.32) into $\boldsymbol{\Delta\vartheta_{sk}} = \boldsymbol{A_{\mathrm{n}}U_n}$. Now, both the curvature and the transverse strain can be defined from the nodal displacements and rotations, with $\boldsymbol{B_{\mathrm{b}}} = \boldsymbol{B_{\mathrm{b}\vartheta}} + \boldsymbol{B_{\mathrm{b}\Delta\vartheta}A_{\mathrm{n}}}$ and $\boldsymbol{B_{\mathrm{s}}} = \boldsymbol{B_{\mathrm{s}\Delta\vartheta}A_{\mathrm{n}}}$ giving:

$$\begin{aligned}\boldsymbol{\chi} &= \boldsymbol{B_{\mathrm{b}}U_{\mathrm{n}}},\\ \boldsymbol{\Upsilon} &= \boldsymbol{B_{\mathrm{s}}U_{\mathrm{n}}}.\end{aligned} \tag{A.35}$$

The plate stiffness matrix, $\boldsymbol{K_{\mathrm{P}}}$, is then constituted by a bending and a shear component:

$$\boldsymbol{K_{\mathrm{b}}} = \int_{A^{\mathrm{e}}} \boldsymbol{B_{\mathrm{b}}}^{\mathrm{T}}\boldsymbol{H_{\mathrm{b}}B_{\mathrm{b}}}dA, \tag{A.36}$$

$$\boldsymbol{K_{\mathrm{s}}} = \int_{A^{\mathrm{e}}} \boldsymbol{B_{\mathrm{s}}}^{\mathrm{T}}\boldsymbol{H_{\mathrm{s}}B_{\mathrm{s}}}dA, \tag{A.37}$$

$$\boldsymbol{K_P} = \boldsymbol{K_b} + \boldsymbol{K_s}. \quad \text{(A.38)}$$

In general terms, the complete stiffness matrix for a shell element is defined with both the membrane and the plate stiffness matrixes (Zienkiewicz and Taylor, 2000).

ANNEX B: AUXILIARY CALCULUS

B.1 BBC 2005

The partial derivatives of the stress function Φ with respect to the planar required by equation (3.31) are the following:

$$\begin{aligned}\frac{\partial\bar{\sigma}}{\partial\Lambda} &= \frac{1}{\bar{\sigma}^{2k-1}}\{a[(\Lambda+\Gamma)^{2k-1}+(\Lambda-\Gamma)^{2k-1}] \\ &\quad + b[(\Lambda+\Psi)^{2k-1}+(\Lambda-\Psi)^{2k-1}]\}, \\ \frac{\partial\bar{\sigma}}{\partial\Gamma} &= \frac{a}{\bar{\sigma}^{2k-1}}[(\Lambda+\Gamma)^{2k-1}-(\Lambda-\Gamma)^{2k-1}], \\ \frac{\partial\bar{\sigma}}{\partial\Psi} &= \frac{b}{\bar{\sigma}^{2k-1}}[(\Lambda+\Psi)^{2k-1}-(\Lambda-\Psi)^{2k-1}],\end{aligned} \tag{B.1}$$

and

$$\begin{aligned}\frac{\partial\Lambda}{\partial\sigma_{xx}} &= \frac{N\left(N\sigma_{xx}-P\sigma_{yy}\right)}{\Lambda}, \frac{\partial\Lambda}{\partial\sigma_{yy}} = -\frac{P\left(N\sigma_{xx}-P\sigma_{yy}\right)}{\Lambda}, \frac{\partial\Lambda}{\partial\sigma_{xy}} = \frac{\sigma_{yx}}{2\Lambda}, \frac{\partial\Lambda}{\partial\sigma_{yx}} \\ &= \frac{\sigma_{xy}}{2\Lambda}, \\ \frac{\partial\Gamma}{\partial\sigma_{xx}} &= L, \frac{\partial\Gamma}{\partial\sigma_{yy}} = M, \frac{\partial\Gamma}{\partial\sigma_{xy}} = 0, \frac{\partial\Gamma}{\partial\sigma_{yx}} = 0, \\ \frac{\partial\Psi}{\partial\sigma_{xx}} &= \frac{Q\left(Q\sigma_{xx}-R\sigma_{yy}\right)}{\Psi}, \frac{\partial\Psi}{\partial\sigma_{yy}} = -\frac{R\left(Q\sigma_{xx}-R\sigma_{yy}\right)}{\Psi}, \frac{\partial\Psi}{\partial\sigma_{xy}} = \frac{\sigma_{yx}}{2\Psi}, \frac{\partial\Psi}{\partial\sigma_{yx}} \\ &= \frac{\sigma_{xy}}{2\Psi}.\end{aligned} \tag{B.2}$$

The partial derivatives of the stress function Φ with respect to the planar required by equation (3.35) are the following:

$$\begin{aligned}\left.\frac{\partial\bar{\sigma}}{\partial\Lambda}\right|_{\theta} &= \frac{1}{{F_{\theta}}^{2k-1}}\{a[(\Lambda_{\theta}+\Gamma_{\theta})^{2k-1}+(\Lambda_{\theta}-\Gamma_{\theta})^{2k-1}] \\ &\quad + b[(\Lambda_{\theta}+\Psi_{\theta})^{2k-1}+(\Lambda_{\theta}-\Psi_{\theta})^{2k-1}]\}, \\ \left.\frac{\partial\bar{\sigma}}{\partial\Gamma}\right|_{\theta} &= \frac{a}{{F_{\theta}}^{2k-1}}[(\Lambda_{\theta}+\Gamma_{\theta})^{2k-1}-(\Lambda_{\theta}-\Gamma_{\theta})^{2k-1}],\end{aligned} \tag{B.3}$$

$$\left.\frac{\partial\bar{\sigma}}{\partial\Psi}\right|_{\theta} = \frac{b}{{F_\theta}^{2k-1}}[(\Lambda_\theta + \Psi_\theta)^{2k-1} - (\Lambda_\theta - \Psi_\theta)^{2k-1}],$$

and

$$\left.\left(\frac{\partial\Lambda}{\partial\sigma_{xx}} + \frac{\partial\Lambda}{\partial\sigma_{yy}}\right)\right|_{\theta} = \frac{(N-P)(N\cos^2\theta - P\sin^2\theta)}{\Lambda_\theta},$$

$$\left.\left(\frac{\partial\Gamma}{\partial\sigma_{xx}} + \frac{\partial\Gamma}{\partial\sigma_{yy}}\right)\right|_{\theta} = L + M, \tag{B.4}$$

$$\left.\left(\frac{\partial\Psi}{\partial\sigma_{xx}} + \frac{\partial\Psi}{\partial\sigma_{yy}}\right)\right|_{\theta} = \frac{(Q-R)(Q\cos^2\theta - R\sin^2\theta)}{\Psi_\theta}.$$

Leading to:

$$\begin{aligned} G_\theta = {} & a\left[\frac{(N-P)(N\cos^2\theta - P\sin^2\theta)}{\Lambda_\theta} + L + M\right](\Lambda_\theta + \Gamma_\theta)^{2k-1} \\ & + a\left[\frac{(N-P)(N\cos^2\theta - P\sin^2\theta)}{\Lambda_\theta} - L - M\right](\Lambda_\theta - \Gamma_\theta)^{2k-1} \\ & + b\left[\frac{(N-P)(N\cos^2\theta - P\sin^2\theta)}{\Lambda_\theta}\right. \\ & \left. + \frac{(Q-R)(Q\cos^2\theta - R\sin^2\theta)}{\Psi_\theta}\right](\Lambda_\theta + \Psi_\theta)^{2k-1} \\ & + b\left[\frac{(N-P)(N\cos^2\theta - P\sin^2\theta)}{\Lambda_\theta}\right. \\ & \left. - \frac{(Q-R)(Q\cos^2\theta - R\sin^2\theta)}{\Psi_\theta}\right](\Lambda_\theta - \Psi_\theta)^{2k-1}, \end{aligned} \tag{B.5}$$

The partial derivatives of the stress function Φ with respect to the planar required by equation (3.41) are the following:

$$\left(\frac{\partial\Lambda}{\partial\sigma_{xx}}\right)\Big|_{\mathrm{b}} = \frac{N(N-P)}{\Lambda_{\mathrm{b}}}, \left(\frac{\partial\Gamma}{\partial\sigma_{xx}}\right)\Big|_{\mathrm{b}} = L, \left(\frac{\partial\Psi}{\partial\sigma_{xx}}\right)\Big|_{\mathrm{b}} = \frac{Q(Q-R)}{\Psi_{\mathrm{b}}}. \tag{B.6}$$

Leading to:

$$G_{\mathrm{b}} = a\left[\frac{N(N-P)}{\Lambda_{\mathrm{b}}} + L\right](\Lambda_{\mathrm{b}} + \Gamma_{\mathrm{b}})^{2k-1} + a\left[\frac{N(N-P)}{\Lambda_{\mathrm{b}}} - L\right](\Lambda_{\mathrm{b}} - \Gamma_{\mathrm{b}})^{2k-1} + b\left[\frac{N(N-P)}{\Lambda_{\mathrm{b}}} + \frac{Q(Q-R)}{\Psi_{\mathrm{b}}}\right](\Lambda_{\mathrm{b}} + \Psi_{\mathrm{b}})^{2k-1} + b\left[\frac{N(N-P)}{\Lambda_{\mathrm{b}}} - \frac{Q(Q-R)}{\Psi_{\mathrm{b}}}\right](\Lambda_{\mathrm{b}} - \Psi_{\mathrm{b}})^{2k-1}. \tag{B.7}$$

B.2 Vegter Model

Knowing that the interpolation function $F(\mu, c)$ is given by equation (3.49), it stands to reason that the principal stresses are given by:

$$\begin{aligned} \sigma_{11} &= \bar{\sigma} F_1(\mu, c), \\ \sigma_{22} &= \bar{\sigma} F_2(\mu, c). \end{aligned} \tag{B.8}$$

Differentiating σ_{11} and σ_{22} with respect to σ_{11} and denoting the mutual independence between the planar stress components yields:

$$\begin{aligned} \frac{\partial \sigma_{11}}{\partial \sigma_{11}} &= \frac{\partial F_1(\mu, c)}{\partial \sigma_{11}} \bar{\sigma} + \frac{\partial \bar{\sigma}}{\partial \sigma_{11}} F_1(\mu, c) = 1, \\ \frac{\partial \sigma_{22}}{\partial \sigma_{11}} &= \frac{\partial F_2(\mu, c)}{\partial \sigma_{11}} \bar{\sigma} + \frac{\partial \bar{\sigma}}{\partial \sigma_{11}} F_2(\mu, c) = 0. \end{aligned} \tag{B.9}$$

Since this independence also applies to c:

$$\begin{aligned} \frac{\partial F_1(\mu, c)}{\partial \sigma_{11}} &= \frac{\partial F_1(\mu, c)}{\partial \mu}\frac{\partial \mu}{\partial \sigma_{11}} + \frac{\partial F_1(\mu, c)}{\partial c}\frac{\partial c}{\partial \sigma_{11}} = \frac{\partial F_1(\mu, c)}{\partial \mu}\frac{\partial \mu}{\partial \sigma_{11}}, \\ \frac{\partial F_2(\mu, c)}{\partial \sigma_{11}} &= \frac{\partial F_2(\mu, c)}{\partial \mu}\frac{\partial \mu}{\partial \sigma_{11}} + \frac{\partial F_2(\mu, c)}{\partial c}\frac{\partial c}{\partial \sigma_{11}} = \frac{\partial F_2(\mu, c)}{\partial \mu}\frac{\partial \mu}{\partial \sigma_{11}}. \end{aligned} \tag{B.10}$$

Recalling that $\partial\Phi/\partial\sigma_{ij} = \partial\bar{\sigma}/\partial\sigma_{ij}$ and replacing in equation (B.9):

$$\begin{aligned} \frac{\partial F_1(\mu, c)}{\partial \mu}\frac{\partial \mu}{\partial \sigma_{11}} \bar{\sigma} + \frac{\partial \Phi}{\partial \sigma_{11}} F_1(\mu, c) = 1, \\ \frac{\partial F_2(\mu, c)}{\partial \mu}\frac{\partial \mu}{\partial \sigma_{11}} \bar{\sigma} + \frac{\partial \Phi}{\partial \sigma_{11}} F_2(\mu, c) = 0. \end{aligned} \tag{B.11}$$

With these, solving for $(\partial\Phi/\partial\sigma_{11})$, after eliminating $(\partial\mu/\partial\sigma_{11})$:

$$\frac{\partial \Phi}{\partial \sigma_{11}} = \frac{\frac{\partial F_2}{\partial \mu}}{F_1\frac{\partial F_2}{\partial \mu} - F_2\frac{\partial F_1}{\partial \mu}}. \tag{B.12}$$

Similarly, differentiating σ_{11} and σ_{22} with respect to σ_{22} and following the same procedure:

$$\frac{\partial \Phi}{\partial \sigma_{22}} = \frac{-\dfrac{\partial F_1}{\partial \mu}}{F_1 \dfrac{\partial F_2}{\partial \mu} - F_2 \dfrac{\partial F_1}{\partial \mu}}. \tag{B.13}$$

To find the relation with respect to c, the parameter μ is considered constant:

$$\begin{aligned} \frac{\partial \sigma_{11}}{\partial c} &= \frac{\partial F_1(\mu, c)}{\partial c}\bar{\sigma} + \frac{\partial \Phi}{\partial c}F_1(\mu, c) = 0, \\ \frac{\partial \sigma_{22}}{\partial c} &= \frac{\partial F_2(\mu, c)}{\partial \sigma_{11}}\bar{\sigma} + \frac{\partial \Phi}{\partial c}F_2(\mu, c) = 0. \end{aligned} \tag{B.14}$$

Similarly:

$$\begin{aligned} \frac{\partial F_1(\mu, c)}{\partial c} &= \frac{\partial F_1(\mu, c)}{\partial c} + \frac{\partial F_1(\mu, c)}{\partial \mu}\frac{\partial \mu}{\partial c}, \\ \frac{\partial F_2(\mu, c)}{\partial c} &= \frac{\partial F_2(\mu, c)}{\partial c} + \frac{\partial F_2(\mu, c)}{\partial \mu}\frac{\partial \mu}{\partial c}. \end{aligned} \tag{B.15}$$

giving:

$$\begin{aligned} \left(\frac{\partial F_1(\mu, c)}{\partial c} + \frac{\partial F_1(\mu, c)}{\partial \mu}\frac{\partial \mu}{\partial c}\right)\bar{\sigma} + \frac{\partial \Phi}{\partial c}F_1(\mu, c) = 0, \\ \left(\frac{\partial F_2(\mu, c)}{\partial c} + \frac{\partial F_2(\mu, c)}{\partial \mu}\frac{\partial \mu}{\partial c}\right)\bar{\sigma} + \frac{\partial \Phi}{\partial c}F_2(\mu, c) = 0. \end{aligned} \tag{B.16}$$

Solving for $(\partial\Phi/\partial c)$, after eliminating $(\partial\mu/\partial c)$:

$$\frac{\partial \Phi}{\partial c} = \bar{\sigma}\frac{\dfrac{\partial F_2}{\partial c}\dfrac{\partial F_1}{\partial \mu} - \dfrac{\partial F_1}{\partial c}\dfrac{\partial F_2}{\partial \mu}}{F_1 \dfrac{\partial F_2}{\partial \mu} - F_2 \dfrac{\partial F_1}{\partial \mu}}. \tag{B.17}$$

This allows to define:

$$\begin{Bmatrix} \dfrac{\partial \Phi}{\partial \sigma_{11}} \\ \dfrac{\partial \Phi}{\partial \sigma_{22}} \\ \dfrac{\partial \Phi}{\partial c} \end{Bmatrix} = \frac{1}{F_1 \dfrac{\partial F_2}{\partial \mu} - F_2 \dfrac{\partial F_1}{\partial \mu}} \begin{Bmatrix} \dfrac{\partial F_2}{\partial \mu} \\ -\dfrac{\partial F_1}{\partial \mu} \\ \bar{\sigma}\left(\dfrac{\partial F_2}{\partial c}\dfrac{\partial F_1}{\partial \mu} - \dfrac{\partial F_1}{\partial c}\dfrac{\partial F_2}{\partial \mu}\right) \end{Bmatrix}. \tag{B.18}$$

B.2.1 Hinge point calculation

Using the notation presented in equation (3.48), the hinge point can be determined by knowing the normal to the yield curve, denoted here by $\vec{n}$ and $\vec{m}$, in the points $\vec{A}$ and $\vec{C}$ respectively. This means that:

$$\left(\vec{B}-\vec{A}\right)\cdot\vec{n}=0\,,\left(\vec{B}-\vec{C}\right)\cdot\vec{m}=0. \tag{B.19}$$

Solving these equations for the coordinates of the hinge point, one obtains:

$$\begin{aligned} B_1 &= \frac{m_2(n_1A_1+n_2A_2)-n_2(m_1C_1+m_2C_2)}{n_1m_2-n_2m_1}, \\ B_2 &= \frac{n_1(m_1C_1+m_2C_2)-m_1(n_1A_1+n_2A_2)}{n_1m_2-n_2m_1}. \end{aligned} \tag{B.20}$$

The derivative of the hinge point with respect to c is defined as:

$$\frac{d}{dc}\begin{bmatrix} n_1 & n_2 \\ m_1 & m_2 \end{bmatrix}\begin{Bmatrix} B_1 \\ B_2 \end{Bmatrix}+\begin{bmatrix} n_1 & n_2 \\ m_1 & m_2 \end{bmatrix}\frac{d}{dc}\begin{Bmatrix} B_1 \\ B_2 \end{Bmatrix}=\frac{d}{dc}\begin{Bmatrix} n_1A_1+n_2A_2 \\ m_1C_1+m_2C_2 \end{Bmatrix}, \tag{B.21}$$

such that:

$$\begin{aligned} \begin{Bmatrix} P_1 \\ P_2 \end{Bmatrix} &= \begin{bmatrix} n_1 & n_2 \\ m_1 & m_2 \end{bmatrix}\begin{Bmatrix} \frac{dB_1}{dc} \\ \frac{dB_2}{dc} \end{Bmatrix} \\ &= \begin{Bmatrix} n_1\frac{dA_1}{dc}+\frac{dn_1}{dc}(A_1-B_1)+n_2\frac{dA_2}{dc}+\frac{dn_2}{dc}(A_2-B_2) \\ m_1\frac{dC_1}{dc}+\frac{dm_1}{dc}(C_1-B_1)+m_2\frac{dC_2}{dc}+\frac{dm_2}{dc}(C_2-B_2) \end{Bmatrix}, \end{aligned} \tag{B.22}$$

leading to:

$$\begin{Bmatrix} \frac{dB_1}{dc} \\ \frac{dB_2}{dc} \end{Bmatrix}=\frac{1}{n_1m_2-m_1n_2}\begin{Bmatrix} P_1m_2-P_2n_2 \\ P_2n_1-P_1m_1 \end{Bmatrix}. \tag{B.23}$$

Considering that that the normal vectors are constituted from the strain ratios, such that $n_1 = 1$ and $n_2 = \rho$:

$$\frac{d\vec{n}}{dc}=\begin{Bmatrix} \frac{dn_1}{dc} \\ \frac{dn_2}{dc} \end{Bmatrix}=\begin{Bmatrix} 0 \\ \frac{d\rho}{dc} \end{Bmatrix}. \tag{B.24}$$

where the derivative of the strain ratio can be derived from the Fourier series.